Ocean surface radial velocity imaging in the AT-INSAR velocity bunching model. A functional approach.

Fabricio Pérez[1], Miguel Ángel Moreles[1], Héctor Morales[2]

[1]Centro de Investigación en Matemáticas (CIMAT)
Jalisco S/N, Col. Valenciana, 36023, Guanajuato, México.

[2]Universidad Autónoma Metropolitana (UAM) – Mathematics Department
San Rafael Atlixco No. 186, Col. Vicentina, 09340, Ciudad de México, México.

Key Points:

- The scalar field of radial velocities of a simulated ocean surface is constructed from a noisy AT-INSAR image of that surface.
- The nonlinear integral equation that relates radial velocities to AT-INSAR intensities is solved by Newton's methods on function spaces.
- Robustness is illustrated by recovering fields of radial velocities for different R/V ratios and other radar parameters.
- A physical comparison is carried out between our results and the scalar field of interferometric velocities, this latter derived from the phase of the AT-INSAR image.

Corresponding author: M. A. Moreles , moreles@cimat.mx

Abstract

[

This work is concerned with the estimation of radial velocities of sea surface elevations. The data, is a noisy along-track interferometric synthetic aperture radar (AT-INSAR) image. We assume the Velocity Bunching Model. This model relates the complex AT-INSAR image at a point in the image plane, with the radial velocity of a scatterer point in the sea surface. The relation is by means of a nonlinear integral operator, mapping radial velocities into AT-INSAR images. Consequently, the estimation of radial velocities amounts to the solution of nonlinear integral equations. Our proposal is to solve the latter by Newton's methods on function spaces, the so-called optimize then discretize approach. We show that this continuous version is accurate, and faster than the classical discretize then optimize version. A physical comparison is also carried out with the interferometric velocities.]

1 Introduction

In recent decades, imaging of the surface of our planet Earth has increased with the appearance and improvement of tele-detection systems, such as Synthetic Aperture Radar (SAR). A SAR system is capable of constructing an image from the information of electromagnetic waves, which are firstly emitted by the radar and then backscattered by the observed region. See (Moreira et al., 2013) for a basic introduction on the subject.

Within the oceanographical context, radar engineers have found that SAR imaging can be successfully applied to measure ocean surface properties, such as currents or wave energy, for example. This adds to the well-known fact that a particular sea state can be statistically modeled by an appropriate two-dimensional directional wave spectrum (Holthuijsen, 2007).

Consequently, an ongoing research problem consists of finding the relationship between SAR images and ocean wave spectra. The literature on this subject is vast. For starters, see the work of (Alpers, 1983), where such relationship is studied. Therein, it is shown that the SAR response to the moving ocean wave field is a nonlinear process for a large range of ocean wave parameters. This means that, in order to determine an ocean wave spectrum, a nonlinear inverse problem is to be solved.

In (K. Hasselmann & Hasselmann, 1991), a mapping of an ocean wave spectrum into a SAR image spectrum is given by a closed integral transform. It is noted that the problem is undetermined when trying to solve for the wave spectrum, and a unique formal inversion of the forward mapping relation cannot exist. The classical approach is to solve a regularized least squares problem, where the cost function is the squared norm of the observed fitted SAR spectra plus a regularization term that uses additional information from a first-guess wave spectrum. The numerical solution is based a quasi-Newton method scheme. This algorithm is improved in (S. Hasselmann et al., 1996), by introducing a modified cost function with an additional iteration loop, such that the first-guess input spectrum is systematically updated.

In the aforementioned works, the observed nonlinear relationship between ocean wave spectra and SAR image spectra stress the effect of *velocity bunching*. This term is used to describe variations on the *scatter density* due to a fluctuating *surface radial velocity*. This physical mechanism causes the formation of wave-like patterns on SAR images of the ocean surface. For more details, see (Alpers & Rufenach, 1979) and K. Hasselmann et al. (1985).

The retrieval of the field of radial velocities is a problem that has attracted some attention recently. It provides complementary information to existing ocean observation systems, see (Hwang et al., 2013) and (Moiseev et al., 2020). In the former, for instance, the interferometric velocity is used to observe wave breaking in swell-dominant conditions, and its own references provide further motivation on the imaging problem that is developed below.

(Goldstein & Zebker, 1987) proposed the so-called airborne along-track interferometric synthetic aperture radar (AT-INSAR). Under this scheme, the radar data is acquired by two antennas, the fore and the aft, which are carried (in baseline) by a flying platform in the along-track direction at a given speed. While the aft antenna transmits the signals, both antennas receive the backscattered signals. Each antenna generates its own raw data, which is processed to produce its corresponding SAR image. After this, both SAR images are combined interferometrically to get the AT-INSAR image. A well-known fact is that the phase difference that is caused by the motion of the surface is proportional to the interferometric velocity. Thus, when the velocity bunching mechanism is a linear process, the interferometric velocity is an appropriate approximation to the surface radial velocity in the wave parameter range. The characterization of this parameter range is presented in (Alpers et al., 1981) and (Alpers & Rufenach, 1979).

Unlike (Goldstein & Zebker, 1987), the purpose of the present work is to retrieve the scalar field of radial velocities when the velocity bunching mechanism is a nonlinear process. Our model of reference is the AT-INSAR Velocity Bunching Model presented in (Mingquan Bao et al., 1997). Such a model relates the complex AT-INSAR image at a point in the image plane, to the radial velocity of a scatterer point in the sea surface. In the mathematical jargon, this relation is given by an integral operator that maps radial velocities into AT-INSAR intensities. Assuming that the radial velocity is known in advance, the AT-INSAR image is readily obtained by quadrature. This is the so-called direct problem. For this work, we consider the following inverse (imaging) problem:

Given a noisy AT-INSAR image of an unknown scalar field of sea surface elevations, estimate the scalar field of radial velocities that is associated with such surface elevations.

Under the first-study assumption that the ocean surface exhibits a swell sea state, we estimate radial velocities by solving the AT-INSAR velocity bunching integral equation.

The core of the paper is the development of numerical methods for solving the underlying integral equation. It will become apparent that the latter is nonlinear and oscillatory, which makes the solution challenging.

We develop two modified Newton's methods on function spaces for solution. First a nonlinear system, second as a nonlinear least squares problem. Derivatives are computed in the sense of Fréchet. See for instance (Cheney, 2001), for the required Functional Analysis.

Both solutions are mutually cross-validating. For comparison we implement also a discretize then optimize approach, in the case of minimization. As expected, the former perform better and are considerably faster in terms of execution time.

A physical comparison is also carried out between the bulk kinetic energy on the ocean surface area under study, associated to the estimated field of radial velocities and that of the interferometric velocities. The comparison is in terms of relative errors, again, the latter is outperformed.

We work with synthetic data, we generate a field of surface elevations following the classical variance spectra to surfaces approach. We obtain a random 2-D realization of a sea surface. Following (Mobley, 2016), we develop our own implementation.

Our work may be regarded as a numerical simulation study in line with (Yoshida, 2016) and (Estatico et al., 2015). In the former, the contribution of bunching to show a wavelike pattern of an azimuthal wave by numerical simulation is explored. In the latter, an algorithm is proposed for a buried object detection problem. Such algorithm is based on a regularizing approach in L^p Banach spaces. In our inverse problem, we follow this function space formalism, using the Hilbert properties of L^2. Our motivation is to postpone discretization *until the last moment*, that is, the optimize then discretize approach. It is proven to be more efficient, (Stuart, 2010), and sometimes necessary, (Zuazua, 2005).

2 Materials and Methods

In this section we formulate the imaging problem of interest and we develop the modified Newton's methods for its solution. We follow a functional approach, that is, we optimize on normed vector spaces of functions.

More precisely, we shall consider all function spaces as subspaces of $L^2\big((a,b)\big)$, the space of square summable complex functions. For two of such functions, namely ϕ and ψ, the inner product is

$$\langle \phi , \psi \rangle \quad = \quad \int_a^b \phi(x)\,\overline{\psi(x)}\,dx \tag{1}$$

We shall freely use all the well-known Hilbertian properties of L^2.

These methods of applied analysis are fully covered in (Cheney, 2001). An attractive feature of this book is the carefully chosen numerical examples. See, for instance, the discussion on Newton's method.

2.1 Problem statement

Our starting point is the AT-INSAR configuration, according to (Goldstein & Zebker, 1987). The AT-INSAR image is acquired by two antennas, the fore and the aft, which are carried (in baseline) by a flying platform in the along-track direction at the speed V. The antennas are separated by a distance $2B$. We assume that the system operates in the so-called mode 1, namely, the aft antenna transmits radar signals, and both antennas receive the backscattered signals.

Hereafter, we use the following notation:

- k_r, the wavenumber of the incoming electromagnetic wave.
- λ_r, the radar wavelength.
- x and x_R, the coordinates in the ground range direction (cross-track).
- y and y_R, the coordinates in the azimuth direction (along-track).
- $\mathbf{x} = (x,y)$, a point in the reference frame of the sea surface.
- $\mathbf{x}_R = (x_R, y_R)$, a point in the image plane.
- $P_{\mathbf{x}}$, the scatterer at the point $(\mathbf{x}, z(\mathbf{x}))$.
- $I(\mathbf{x}_R)$, the AT-INSAR image at the position $\mathbf{x}_R$ associated with $P_{\mathbf{x}}$.
- R, the distance from the median of the two antennas to $P_{\mathbf{x}}$.
- τ_s, the scene coherence time.

We assume the AT-INSAR Velocity Bunching Model for a complex AT-INSAR image I_{vb}, as introduced in (Mingquan Bao et al., 1997). In this model, the AT-INSAR (single-look) integration time T_0 is considered small when compared to the period of the dominant ocean wave. So, both the normalized radar cross section (NRCS) $\sigma(\mathbf{x},t)$ and the radial velocity $u_r(\mathbf{x},t)$ show a small variation with respect to time. This allows an approximation of these values by the respective quantities $\sigma_0(\mathbf{x})$ and $u_r(\mathbf{x})$, which are independent of time. In the particular case of the radial velocity, a first order approximation in time around $t_0 = \mathbf{x}/V$ is used:

$$u_r(\mathbf{x},t) \approx u_r(\mathbf{x}) + a_r(\mathbf{x})(t - t_0)$$

Here, $a_r(\mathbf{x})$ denotes the radial acceleration (at $\mathbf{x}$) that is associated with the ocean surface.

With these considerations, the expression for $I_{vb}(y_R) \equiv I_{vb}(\mathbf{x}_R)$ is:

$$\begin{aligned} I_{vb}(y_R) &= \frac{\pi T_0^2 \rho_a}{2} \exp\left[-\frac{4B^2}{V^2 T_0^2} \right] \int_{-\infty}^{+\infty} \frac{\sigma_0(\mathbf{x})}{\rho_a'(\mathbf{x})} \\ &\quad \times \exp\left[-2jk_r \frac{B}{V} u_r(\mathbf{x}) \right] \exp\left[\frac{4B^2 \rho_a^2}{V^2 T_0^2 \rho_a'^2(\mathbf{x})} \right] \\ &\quad \times \exp\left[\frac{2jBk_r}{R} \left(\frac{2\rho_a^2}{\rho_a'^2(\mathbf{x})} - 1 \right) \left(y_R - y - \frac{R}{V} u_r(\mathbf{x}) \right) \right] \\ &\quad \times \exp\left[-\frac{\pi^2}{\rho_a'^2(\mathbf{x})} \left(y_R - y - \frac{R}{V} u_r(\mathbf{x}) \right)^2 \right] dy \end{aligned} \tag{2}$$

$$\rho_a'(\mathbf{x}) = \left\{ \rho_a^2 + \left[\frac{\pi}{2} \frac{T_0 R}{V} a_r(\mathbf{x}) \right]^2 + \frac{\rho_a^2 T_0^2}{\tau_s^2} \right\}^{1/2} \tag{3}$$

Here, $\rho_a'(\mathbf{x})$ denotes the degraded single-look azimuthal resolution, and $\rho_a = \lambda_r R/(2VT_0)$ is the full-bandwidth, single-look azimuthal resolution for stationary targets.

The inverse (imaging) problem of interest is stated as follows: given a noisy AT-INSAR image D of an unknown sea surface z, compute an approximation of the corresponding scalar field of radial velocities u_r that is associated with z.

We assume that $D(\mathbf{x}_R)$ is a complex AT-INSAR image $I_{vb}(\mathbf{x}_R)$ that is corrupted by additive noise η, namely, $D = I_{vb} + \eta$. Note that, for each fixed x in the cross-track direction, the problem consists of solving an oscillatory nonlinear integral equation for $u_r(\cdot) \equiv u_r(x, \cdot)$.

For later reference, let us define

$$A_0 = \frac{\pi T_0^2 \rho_a}{2} \exp\left[-\frac{4B^2}{V^2 T_0^2} \right] \tag{4}$$

and

$$A_1 = y_R - y - \frac{R}{V} u_r(\mathbf{x}) \tag{5}$$

Finally, if we denote the integrand by f_{vb}, equation (2) can be written in the form:

$$I_{vb}(y_R) = A_0 \int_{-\infty}^{+\infty} f_{\mathrm{vb}}(u_r(\mathbf{x}), a_r(\mathbf{x}), \mathbf{x}, y_R)\, dy \tag{6}$$

Remark

In our case study, it is found a fortiori, that variations of this integral operator with respect to the radial acceleration are negligible. Consequently, the terms involving the latter in the Newton's methods that follow are discarded. It is possible to show this mathematically, but in this work we will only focus on the numerical results.

2.2 Newton's method for the nonlinear integral equation

The nonlinear integral equation (given above), implicitly defines a map between some function spaces $\mathscr{V}$ and $\mathscr{W}$, namely,

$$\mathscr{V} \to \mathscr{W}, \quad u_r \mapsto \mathscr{I}(u_r) = I_{vb}.$$

To formulate the inversion problem as the solution of a nonlinear integral equation, we consider the residual map

$$\mathscr{F} : \mathscr{V} \to \mathscr{W}, \quad \mathscr{F}(u_r) = D - I_{vb}.$$

The problem is to find u_r such that

$$\mathscr{F}(u_r) = 0.$$

Assuming Fréchet differentiability, we apply the Newton's method.

Given the initial guess $u_r^0 \in \mathscr{V}$, we solve at each iteration k for the function h^k

$$\mathscr{F}'(u_r^k)\, h^k \;=\; -\mathscr{F}(u_r^k) \tag{7}$$

and update

$$u_r^{k+1} = u_r^k + h^k. \tag{8}$$

Here, $\mathscr{F}'$ is the Fréchet derivative of $\mathscr{F}$. It follows that

$$\mathscr{F}'(u_r) = -\mathscr{I}'(u_r) = -I'_{vb}, \quad \text{and}$$

$$I'_{vb}h = A_0 \int_{-\infty}^{\infty} \left[\frac{\partial f_{vb}}{\partial u_r}\right] h(y)\, dy$$

where $(\partial f_{vb}/\partial u_r)$ is the vector calculus derivative of f_{vb} with respect to u_r:

$$\frac{\partial f_{vb}}{\partial u_r} = \left[\frac{2\pi^2 R A_1}{V\rho_a'^2} \;-\; j\,\frac{4Bk_r\rho_a^2}{V\rho_a'^2}\right] f_{vb} \tag{9}$$

We remark that the scheme (7), (8) is the continuous (infinite dimensional) version of the Newton's method.

Subsequently, we discretize with an appropriate quadrature to obtain a finite dimensional residual $F : \mathbb{R}^{N_y} \to \mathbb{R}^{2N_y}$.

The Newton's method reads: given an initial guess $\vec{u}_r^{\,0} \in \mathbb{R}^{N_y}$, solve at each iteration k:

$$F'(\vec{u}_r^{\,k})\,\vec{h}^k \;=\; -F(\vec{u}_r^{\,k}) \tag{10}$$

$$\vec{u}_r^{\,k+1} \;=\; \vec{u}_r^{\,k} + \vec{h}^k \tag{11}$$

The linear system to be solved in each iteration is overdetermined and ill conditioned. Thus, its numerical solution is somewhat challenging.

We apply Tikhonov regularization using the SVD of $F'(\vec{u}_r^{\,k})$, namely,

$$\vec{h}^k \;\approx\; \vec{h}^k_{\alpha_T} \;=\; -\sum_{i=1}^{N_y} \frac{\sigma_i}{\sigma_i^2 + \alpha_T}\left[\vec{u}_i \cdot F(\vec{u}_r^{\,k})\right]\vec{v}_i \tag{12}$$

where $\sigma_i \in \mathbb{R}_{\geq 0}$ is the i-th largest singular value of $F'(\vec{u}_r^{\,k})$, $\vec{u}_i \in \mathbb{R}^{2N_y}$ is the corresponding i-th left singular vector, and $\vec{v}_i \in \mathbb{R}^{N_y}$ is the corresponding i-th right singular vector.

This regularization technique is classical, see (Vogel, 2002). The problem strives on the choice of the regularization parameter for a successful application. Here, the parameter is set to the square of the first (and largest) singular value of $F'(\vec{u}_r^{\,k})$:

$$\alpha_T \;\leftarrow\; \sigma_1^2 \tag{13}$$

2.3 A minimization approach

For comparison, we develop a descent method for the corresponding nonlinear squares problem. The underlying functional,

$$\mathscr{G} : \mathscr{V} \to [0, \infty),$$

is given by

$$\mathscr{G}(u_r) = \frac{1}{2}\|\mathscr{F}(u_r)\|^2 = \frac{1}{2}\langle \mathscr{F}(u_r), \mathscr{F}(u_r)\rangle$$

It is readily seen that the Fréchet derivative of $\mathscr{G}$ at u_r applied to h is:

$$\mathscr{G}'(u_r)h = \frac{1}{2}\left[\langle h, (\mathscr{F}'(u_r))^* \mathscr{F}(u_r)\rangle + \overline{\langle h, (\mathscr{F}'(u_r))^* \mathscr{F}(u_r)\rangle}\right]$$

where $(\mathscr{F}'(u_r))^*$ is the adjoint operator of $\mathscr{F}'(u_r)$. Hence,

$$\mathscr{G}'(u_r)h = \langle h, \mathrm{Re}\left\{(\mathscr{F}'(u_r))^* \mathscr{F}(u_r)\right\}\rangle$$

Substituting $\mathscr{F}'(u_r)$, it follows that

$$\mathscr{G}'(u_r)h \quad = \quad \left\langle h, \mathrm{Re}\left\{ -A_0 \int_{-\infty}^{\infty} \left[\frac{\partial f_{vb}}{\partial u_r}\right] \overline{\left[\left[\mathscr{F}(u_r)\right](y_R)\right]} dy_R \right\} \right\rangle \tag{14}$$

By the Riesz representation theorem, the second argument of the inner product is the continuous gradient of $\mathscr{G}$ at u_r. That is, the function $\nabla\mathscr{G}(u_r)$ is defined as:

$$\nabla\mathscr{G}(u_r) \quad = \quad \mathrm{Re}\left\{ -A_0 \int_{-\infty}^{\infty} \left[\frac{\partial f_{vb}}{\partial u_r}\right] \overline{\left[\left[\mathscr{F}(u_r)\right](y_R)\right]} dy_R \right\} \tag{15}$$

The minimization problem is solved by the BFGS method with known gradient. In our case, a discrete version of (15).

3 Synthetic Data

In this section we specify the parameters and functions that we have employed to simulate the ocean surface and its associated AT-INSAR data. The area under study is a square Q with 1280 meters of side length, centered at the origin. We consider a 128×128 uniform square mesh, whose computation points lie at their vertices. Using this area with its mesh, the simulated ocean surface is $z : Q \to \mathbb{R}$, and its associated AT-INSAR data is $D : Q \to \mathbb{C}$.

3.1 Sea surface

We have developed our own software for ocean surface simulation. We follow the classical variance spectra to surface approach, to generate a random 2-D realization of a sea surface, see (Mobley, 2016). We adopt the configuration given in (Mingquan Bao et al., 1997). Table 1 shows ocean surface parameters.

Description	Name	Value	Units	Parameter
Wind speed	U_{10}	5	[m s^{-1}]	input
Peak wavelength	λ_S	100	[m]	input
Peak wave period	T_S	8.004415	[s]	derived

Table 1. Ocean surface parameters.

Since our basis for comparison is (Brüning et al., 1990), we consider a swell sea described by the highly-peaked JONSWAP omnidirectional spectrum introduced therein. Namely,

$$\mathscr{S}_S(k) = \frac{\alpha_S}{2k^3}\exp\left[-\frac{5}{4}\left(\frac{k}{k_S}\right)^{-2}\right]\gamma_S{}^{G_S}$$

where

$$G_S = \exp\left[-\frac{1}{2}\frac{\left(k^{1/2} - k_S^{1/2}\right)^2}{\sigma_S^2 k_S}\right]$$

Here,

- $\alpha_S = 0.212\times10^{-3}$ is the energy scale of $\mathscr{S}_S$.
- $k_S = (2\pi)/\lambda_S$ is the spatial peak frequency of $\mathscr{S}_S$.
- $\gamma_S = 10$ is the peak enhancement factor of $\mathscr{S}_S$.
- σ_S is the spectral width centered at k_S,

$$\sigma_S = \begin{cases} 0.07 & \text{for } k \le k_S \\ 0.09 & \text{for } k > k_S \end{cases} \tag{16}$$

In the frequency domain, figure 1 depicts the omnidirectional spectrum $\mathscr{S}_S$, whose narrow shape —centered at low frequencies— constitutes the underlying model that generates a swell sea state in the space-time domain. This spectrum $\mathscr{S}_S$ corresponds to one of the sea state configurations that are proposed in (Brüning et al., 1990), which in turn is adopted by (Mingquan Bao et al., 1997) in its AT-INSAR imaging problem of ocean waves.

Figure 1. Omnidirectional spectrum $\mathscr{S}_S$: continuous (line) and sampled (dots).

Next, a spreading function is used. In this case, the two-sided cosine-power model,

$$\Phi_{cp2}(k,\phi) = \frac{1}{2}N_p\left|\cos(\phi-\phi_w)\right|^{2p}, \qquad |\phi-\phi_w| \le \pi,$$

Leading to the two-sided directional swell spectrum,

$$\hat{\mathscr{S}}_{2C}(k_x,k_y) = \frac{1}{k}\mathscr{S}_S(k)\,\Phi_{cp2}(k,\phi),$$

where (k,ϕ) and (k_x,k_y) are the equivalent polar and cartesian coordinates, respectively.

We obtain a particular instance of the ocean variance spectrum $\hat{z}$. The ocean surface z is obtained by computing the discrete inverse Fourier transform of $\hat{z}$.

3.2 The AT-INSAR data

Table 2 shows the values that are given to the input parameters for the configuration of the AT-INSAR system. This selection is based on part III-B of (Mingquan Bao et al., 1997).

Description	Name	Value	Units
Angle of incidence	θ_r	$\pi/4$	[rad]
Platform speed	V	200	[m s^{-1}]
Carrier frequency	f_0	1.25×10^9	[s^{-1}]
Target exposure time	T_0	0.751	[s]
Half the distance between antennas	B	9.8	[m]
Scene coherence time	τ_s	0.12	[s]
Radar polarization (like-polarized)	VV	–	–
Number of NRCS realisations	N_σ	100	[realisations]

Table 2. Input parameters to configure the AT-INSAR system.

Based on table 2 and the ocean variance spectrum $\hat{z}$, we show a relevant set of derived parameters and functions in table 3. This configuration allows the construction of the discrete scalar fields of ocean-radar interaction: the radial velocities u_r, the radial accelerations a_r, and the time-averaged radar reflectivities σ_0.

Description	Name	Value	Units
Radar wavelength	λ_r	0.239834	[m]
Radar wavenumber	k_r	26.19806	[rad m^{-1}]
Antenna length (in azimuth)	L_a	21.22099	[m]
Time separation between antennas	Δt	0.049	[s]
Field of radial velocities	u_r	$u_r[\mathbf{x}_R]$	[m s^{-1}]
Field of radial accelerations	a_r	$a_r[\mathbf{x}_R]$	[m s^{-2}]
Field of radar reflectivities	σ_0	$\sigma_0[\mathbf{x}_R]$	[1]

Table 3. Derived parameters and functions of the AT-INSAR system.

From the information of table 3, the intensity $I_{vb}(\mathbf{x}_R)$ is approximated by quadrature.

Our modeling study is within the scope of inverse problems theory, see (Kaipio & Somersalo, 2005). In this context, we consider additive noise at each $\mathbf{x}_R$.

More precisely, to generate synthetic data, we add to $I_{vb}(\mathbf{x}_R)$ noise $\eta(\mathbf{x}_R)$ given by

$$\eta(\mathbf{x}_R) = \frac{1}{\sqrt{2}}\big[a_\eta(\mathbf{x}_R) + jb_\eta(\mathbf{x}_R)\big],$$

where the elements $a_\eta(\mathbf{x}_R)$ and $b_\eta(\mathbf{x}_R)$ are independent, identically distributed, real Gaussian random variables, with mean 0 and variance $\sigma^2_\eta(\mathbf{x}_R)$.

The location-dependent standard deviation $\sigma_\eta(\mathbf{x}_R)$ is given by

$$\sigma_\eta(\mathbf{x}_R) = \varepsilon \ \max\Big\{|I_{\mathrm{vb}}(\mathbf{x}_R)| \ , \ \mathrm{LB}\Big\} \tag{17}$$

We set $\varepsilon = 0.05$, allowing a 5% Gaussian error. $\mathrm{LB} = 1 \times 10^{-10}$ is about the same order of magnitude of $I_{vb}(\mathbf{x})$. This latter is introduced to avoid point supported densities.

Consequently, the noisy AT-INSAR data D is given by

$$D(\mathbf{x}_R) = I_{vb}(\mathbf{x}_R) + \eta(\mathbf{x}_R)$$

3.3 Interferometric velocities

Given the noisy AT-INSAR image D, the interferometric phase Φ_{ATI} is $\Phi_{ATI} = \angle D$, the latter is proportional to the interferometric velocity u_{ATI} (Goldstein & Zebker, 1987):

$$u_{ATI}(\mathbf{x}) = -\frac{\lambda_r}{4\pi}\frac{V}{B}\Phi_{ATI}(\mathbf{x}_R).$$

In applications, u_{ATI} is used as an approximation of the radial velocity u_r. We gauge this approximation in the results that follow.

4 Numerical Results

For imaging of the radial velocity, we consider two main configurations: range travelling waves (RTW) and azimuthally travelling waves (ATW). In the former, both tilt and hydrodynamic modulations of the ocean surface are specially stronger, whereas azimuthal smearing and velocity bunching of the ocean surface are particularly stronger in the latter.

In the Appendix we shall present results for variations of both RTW and ATW, which consists of a different wind direction ϕ_w and two additional R/V ratios. Here we fully report the *RTW scenario*, which is based on section III-B of (Mingquan Bao et al., 1997).

Table 4 shows the particular values that characterize this scenario. Figure 2 depicts its most relevant fields and spectra. Note that the angle ϕ_0 [rad] given here corresponds to the angle $\phi_p = \phi_w - \phi_0 + \pi/2$ [rad] given in (Mingquan Bao et al., 1997).

Description	Name	Value	Units	Parameter
Wind direction	ϕ_w	0	[rad]	input
Azimuthal look direction	ϕ_0	0	[rad]	input
Slant range	R	15×10^3	[m]	input
Range-to-velocity ratio	R/V	75	[s]	derived
Variance of surface elevation	$Var\{z(\mathbf{x}_R,t)\}$	0.020575	[m^2]	derived
Sample variance of z	s_z^2	0.021478	[m^2]	derived
Sample significant wave height	$\hat{H}_{m_0}$	0.586215	[m]	derived
Azimuth SAR resolution	ρ_a	11.97573	[m]	derived
Vector of radar LOS	v_{LOS}	$\left[\frac{\sqrt{2}}{2}, 0, -\frac{\sqrt{2}}{2}\right]^T$	unitary	derived

Table 4. The RTW scenario: input and derived parameters.

Figure 2. The RTW scenario: its most relevant fields and spectra.

As we show in figure 2(b), some properties of the ocean surface z are evident: there is a regular pattern of waves whose directions are very close to the wind direction $\phi_w = 0$ [rad], the majority of wavelengths are around $\lambda_S = 100$ [m], and a big amount of measured wave heights is well characterized by $\hat{H}_{m_0} = 0.586215$ [m].

4.1 Radial velocity imaging

Given $D(\mathbf{x}_R)$ for each x_R (cross-track coordinate) we solve for $u_r(\mathbf{x})$, both the Nonlinear System (NL) and the Functional Minimization (FM), which are associated with the nonlinear integral equation. In total there are 128 problems ordered from left to right, from 0 to 127.

We stress that we follow the optimize then discretize approach. For comparison, we use the discretize then optimize in the minimization problem. Results with the latter shall be referred as DFM.

In the minimization problems, the main difference is the computation of the gradient. In the infinite dimensional, optimize then discretize approach, the gradient is analytic and is given by the expression (15). In the discretize then optimize formulation, the gradient is approximated with appropriate finite differences of the discretized (finite dimensional) functional.

To avoid bias, we start all iterative methods with $u_r^0 \equiv 0$ as initial guess.

Summarizing, for each optimization problem, we compute the following four solutions:

- The Nonlinear System solution, denoted by u_r^*–NL.
- The Continuous Functional Minimization solution, denoted by u_r^*–FM.
- The Discrete Functional Minimization solution, denoted by u_r^*–DFM.
- The interferometric velocity solution, denoted by u_{ATI}.

To show a global comparison, we compute the Root Mean Square Error (RMSE) of each solution with respect to the target u_r. In figures 3 and 4, we exhibit such comparison for each optimization problem (each point in the horizontal axis corresponds to a fitting problem).

Figure 3. Blue: u_r^*–NL Black: u_r^*–DFM Violet: u_{ATI}

Figure 4. Red: u_r^*–FM Black: u_r^*–DFM Violet: u_{ATI}

From figure 3, it is apparent that NL performs better than DFM. From figure 4, we see that both FM and FDM have a very similar performance. Finally, both figures 3 and 4 illustrate that any optimization strategy (NL, FM or FDM) for any optimization problem, outperforms the interferometric velocity of (Goldstein & Zebker, 1987).

For the interested reader, our exhaustive numerical experiments are available in the Marine Data Archive (MDA) repository, in accordance with the Data Availability Statement that we have provided below. It is apparent that results are remarkably consistent in all RTW, ATW configurations for the 128 problems. In the Appendix we show a small sample.

In the following numerical results, we employ a specific figure to show the solution of a particular problem via a particular strategy. More specifically, the figure contains the fit for the radial velocity (using a particular strategy) and its associated AT-INSAR image I (the for-

ward mapping). In each figure, and for comparison purposes, we have also included the interferometric velocity solution u_{ATI}. In the case under study for this section, we only show problems 0 and 64.

Figures 5 and 6 are related to the same problem 0: figure 5 shows the solution to problem 0 via the Nonlinear System solution u_r^*–NL, whereas figure 6 shows the solution to problem 0 via the Continuous Functional Minimization solution u_r^*–FM.

Figure 5. PROBLEM 0 VIA NL. Top: radial velocity u_r (black), initial point ${u_r}^0$ (**blue**), interferometric velocity u_{ATI} (**violet**), estimated radial velocity u_r^* (**red**); Middle: Re$\{D\}$ (**black**), Re$\{I_0\}$ (**blue**), Re$\{I_{ATI}\}$ (**violet**), Re$\{I_*\}$ (**red**); Bottom: Im$\{D\}$ (**black**), Im$\{I_0\}$ (**blue**), Im$\{I_{ATI}\}$ (**violet**), Im$\{I_*\}$ (**red**).

Figure 6. PROBLEM 0 VIA FM. Top: radial velocity u_r (black), initial point ${u_r}^0$ (**blue**), interferometric velocity u_{ATI} (**violet**), estimated radial velocity u_r^* (**red**); Middle: Re$\{D\}$ (**black**), Re$\{I_0\}$ (**blue**), Re$\{I_{ATI}\}$ (**violet**), Re$\{I_*\}$ (**red**); Bottom: Im$\{D\}$ (**black**), Im$\{I_0\}$ (**blue**), Im$\{I_{ATI}\}$ (**violet**), Im$\{I_*\}$ (**red**).

Figures 7 and 8 are related to the same problem 64: figure 7 shows the solution to problem 64 via the Nonlinear System solution u_r^*–NL, whereas figure 8 shows the solution to problem 64 via the Continuous Functional Minimization solution u_r^*–FM.

Figure 7. PROBLEM 64 VIA NL. Top: radial velocity u_r (black), initial point ${u_r}^0$ (**blue**), interferometric velocity u_{ATI} (**violet**), estimated radial velocity u_r^* (**red**); Middle: Re$\{D\}$ (**black**), Re$\{I_0\}$ (**blue**), Re$\{I_{ATI}\}$ (**violet**), Re$\{I_*\}$ (**red**); Bottom: Im$\{D\}$ (**black**), Im$\{I_0\}$ (**blue**), Im$\{I_{ATI}\}$ (**violet**), Im$\{I_*\}$ (**red**).

Figure 8. PROBLEM 64 VIA FM. Top: radial velocity u_r (black), initial point ${u_r}^0$ (**blue**), interferometric velocity u_{ATI} (**violet**), estimated radial velocity u_r^* (**red**); Middle: Re$\{D\}$ (**black**), Re$\{I_0\}$ (**blue**), Re$\{I_{ATI}\}$ (**violet**), Re$\{I_*\}$ (**red**); Bottom: Im$\{D\}$ (**black**), Im$\{I_0\}$ (**blue**), Im$\{I_{ATI}\}$ (**violet**), Im$\{I_*\}$ (**red**).

4.2 Computational efficiency

In practice, imaging problems are computationally expensive. In the discretize then optimize approach, the approximation of derivatives by finite differences is costly. Having the exact derivative, and postponing discretization *until the last moment*, the solution is in general more efficient.

We can see this advantage in figures 9 and 10, where we report the values of execution time for the 128 inversion problems: in figure 9, we show the comparison between the solutions u_r^*–NL and u_r^*–DFM; in figure 10, we show the comparison between the solutions u_r^*–FM and u_r^*–DFM. We notice that both NL and FM are at least one order of magnitude faster than DFM.

Figure 9. Blue: u_r^*–NL Black: u_r^*–DFM

Figure 10. Red: u_r^*–FM Black: u_r^*–DFM

4.3 A physical comparison

A first inspection of radial velocity fitting and AT-INSAR images, figures 5, 6, 7 and 8, the gain with respect to the interferometric velocity u_{ATI} may seem marginal. To compare in terms of a physical quantity, we compute the relative error of kinetic energies (RE-KE) that are associated with the whole two-dimensional fields u_r^*–NL, u_r^*–FM and u_{ATI}. Results are shown in table 5.

The relative error of u_{ATI} is much greater than u_r^*–NL and u_r^*–FM. The error of using u_{ATI} is about 12%. In soome appliecations this might be critical.

Estimated solution	u_r^*-NL	u_r^*-FM	u_{ATI}
RE-KE	0.0630604	0.0130545	0.1240790

Table 5. Relative errors of kinetic energies associated with three estimated solutions.

5 Technical information

For the simulation of the ocean surface realizations, the AT-INSAR images (forward mappings), and the functional versions of the Newton's methods (inverse mappings), we have developed our own in house implementations. The comparative performance of the methods given above was carried out in a computer with the following specifications:

Hardware

- Processor: AMD © A10-5800B with Radeon(tm) HD Graphics, 3.80 GHz
- Physical memory: 8.00 Gb (7.20 Gb usable).
- Round-off unit (machine epsilon): $\varepsilon_M = 2.220446049250313 \times 10^{-16}$.

Software

- System type: 64-bit operating system.
- Operating system: Windows 7 Professional © 2009 – SP1, Microsoft Corporation.
- Programming language: Anaconda3 5.2.0 with Python 3.6.5 for 64 bits.
- Classical numerical methods (e.g. SVD and BFGS): NumPy and SciPy packages.
- IDE: The Scientific PYthon Development EnviRonment (Spyder) ©, version 3.2.8

6 Conclusions

Assuming the AT-INSAR-VB model, we have posed —the estimation of radial velocities of a simulated ocean surface— as the solution to a nonlinear integral equation. To solve this equation, we have developed functional (infinite-dimensional) versions of two modified Newton's methods, namely, a nonlinear system method coupled with Tikhonov regularization, and the BFGS method with known gradient for functional minimization.

For each technique, we have formulated the solution on function spaces, where the application of the Newton's method requires the Fréchet derivative of the objective function.

We have implemented discrete models and numerical algorithms, which have led to numerical results that are satisfactory. The functional approach produces faster solutions when compared to the classical discretize then optimize strategy. Furthermore, the fitting of the estimated solutions of radial velocity improves upon the interferometric velocitiy u_{ATI}. Finally, the comparison of predicted kinetic energies shows that, for certain applications, a better fit other than interferometric velocities is required.

This research is manifold: ocean waves modeling, SAR imaging of sea surfaces, inverse problems, numerical optimization, computational methods, etc. On the modeling side, we have only considered a swell spectrum. We left for future works other spectra of interest, such as those of JONSWAP and Pierson-Moskowitz. Also, the synthetic character of our input data may be regarded as a drawback. An imaging problem with actual data in a realistic test area is desired. However, a closer look to our methodology shows that the results mainly depend on the integral transform, and so the methods apply regardless of the test area. We shall provide evidence of this in later works.

Research on methods for sea surface imaging is ongoing. In a computational sense, the use of High Performance Computing is a straightforward continuation of this work. In our study, an integral equation is solved separately for each point in the cross track coordinate. This is because of the AT-INSAR-VB model, in which all the optimization problems are mutually independent. Consequently, a parallel implementation in a low-level computer language shall lead to even faster solutions.

ORCID

M. A. Moreles https://orcid.org/0000-0003-1643-1844

J. H. Morales-Barcenas https://orcid.org/0000-0001-9377-4918

F. O. Pérez https://orcid.org/0000-0002-2814-3447

Acknowledgments

Research supported in part by Conacyt project A1-S-17634

Data Availability Statement

The data sets associated with this paper are available at the Flanders Marine Institute.

Data set of Range Travelling Waves: https://doi.org/10.14284/444

Data set of Azimuthally Travelling Waves: https://doi.org/10.14284/446

References

Alpers, W. (1983). Monte carlo simulations for studying the relationship between ocean wave and synthetic aperture radar image spectra. *Journal of Geophysical Research: Oceans*, *88*(C3), 1745-1759.

Alpers, W., & Rufenach, C. (1979). The effect of orbital motions on synthetic aperture radar imagery of ocean waves. *IEEE Transactions on Antennas and Propagation*, *27*(5), 685-690.

Alpers, W. R., Ross, D. B., & Rufenach, C. L. (1981). On the detectability of ocean surface waves by real and synthetic aperture radar. *Journal of Geophysical Research: Oceans*, *86*(C7), 6481-6498.

Brüning, C., Alpers, W., & Hasselmann, K. (1990). Monte-carlo simulation studies of the nonlinear imaging of a two dimensional surface wave field by a synthetic aperture radar. *International Journal of Remote Sensing*, *11*(10), 1695-1727.

Cheney, E. W. (2001). *Analysis for applied mathematics*. New York: Springer-Verlag.

Estatico, C., Fedeli, A., Pastorino, M., & Randazzo, A. (2015). Buried object detection by means of a lp banach-space inversion procedure. *Radio Science*, *50*(1), 41-51.

Goldstein, R. M., & Zebker, H. A. (1987). Interferometric radar measurement of ocean surface currents. *Nature*, *328*, 707-709.

Hasselmann, K., & Hasselmann, S. (1991). On the nonlinear mapping of an ocean wave spectrum into a synthetic aperture radar image spectrum and its inversion. *Journal of Geophysical Research: Oceans*, *96*(C6), 10713-10729.

Hasselmann, K., Raney, R. K., Plant, W. J., Alpers, W., Shuchman, R. A., Lyzenga, D. R., ... Tucker, M. J. (1985). Theory of synthetic aperture radar ocean imaging: A marsen view. *Journal of Geophysical Research: Oceans*, *90*(C3), 4659-4686.

Hasselmann, S., Brning, C., Hasselmann, K., & Heimbach, P. (1996). An improved algorithm for the retrieval of ocean wave spectra from synthetic aperture radar image spectra. *Journal of Geophysical Research: Oceans*, *101*(C7), 16615-16629.

Holthuijsen, L. H. (2007). *Waves in oceanic and coastal waters*. United Kingdom: Cambridge University Press.

Hwang, P. A., Toporkov, J. V., Sletten, M. A., & Menk, S. P. (2013). Mapping surface currents and waves with interferometric synthetic aperture radar in coastal waters: Observations of wave breaking in swell-dominant conditions. *Journal of Physical Oceanography*, *43*(3), 563-582.

Kaipio, J., & Somersalo, E. (2005). *Statistical and computational inverse problems*. New York: Springer-Verlag.

Mingquan Bao, Bruning, C., & Alpers, W. (1997). Simulation of ocean waves imaging by an along-track interferometric synthetic aperture radar. *IEEE Transactions on Geoscience and Remote Sensing*, *35*(3), 618-631.

Mobley, C. D. (2016). *Modeling sea surfaces. a tutorial on fourier transform techniques. version 2.0*. Sequoia Scientific, Inc.

Moiseev, A., Johnsen, H., Johannessen, J. A., Collard, F., & Guitton, G. (2020). On removal of sea state contribution to sentinel-1 doppler shift for retrieving reliable ocean surface

current. *Journal of Geophysical Research: Oceans*, *125*(9), e2020JC016288.
Moreira, A., Prats-Iraola, P., Younis, M., Krieger, G., Hajnsek, I., & Papathanassiou, K. P. (2013). A tutorial on synthetic aperture radar. *IEEE Geoscience and Remote Sensing Magazine*, *1*(1), 6-43.
Stuart, A. M. (2010). Inverse problems: A bayesian perspective. *Acta Numerica*, *19*, 451559.
Vogel, C. R. (2002). *Computational methods for inverse problems*. Philadelphia: Society for Industrial and Applied Mathematics (SIAM).
Yoshida, T. (2016). Numerical research on clear imaging of azimuth-traveling ocean waves in sar images. *Radio Science*, *51*(7), 989-998.
Zuazua, E. (2005). Propagation, observation, and control of waves approximated by finite difference methods. *SIAM Review*, *47*(2), 197-243.

7 Appendix. Numerical results for different directions and R/V ratios

This complementary section presents a small sample of numerical results, which we have selected from the results of the whole set of $N_x = 128$ problems. As pointed out above, since all the fitting results are remarkably similar, we only show two problems from the variants of the scenarios RTW and ATW. To cover different regions of our simulated ocean surface, our sample comprises the equidistant problems 0, 16, 32, 48, 64, 80, 96 and 112. We only show results for the FM method, because the solutions that are obtained with the NL and DFM methods are consistent with the results that are reported in section 4.

7.1 Scenarios: input and derived parameters

To test our proposed methods under different conditions, we specify here the set of parameters that determine each of five additional scenarios. On the one hand, the five scenarios are governed by the same properties that we provide in subsection 3.1 and table 2. On the other hand, each scenario is distinctive from the others because of the values of three input parameters: the azimuthal look direction ϕ_0, the wind direction ϕ_w, and the slant range R. In particular, the modification of the ratio R/V is of interest in velocity bunching.

These are the five scenarios: RTW-R16 (table 6, figure 11); RTW-R18 (table 7, figure 14); ATW (table 8, figure 17); ATW-R16 (table 9, figure 20); ATW-R18 (table 10, figure 23). Their construction is based on sections III-B and III-E of (Mingquan Bao et al., 1997).

Description	Name(s)	Value(s)	Units	Parameter
Wind direction	ϕ_w	$\pi/9$	[rad]	input
Azimuthal look direction	ϕ_0	0	[rad]	input
Slant range	R	16×10^3	[m]	input
Range-to-velocity ratio	R/V	80	[s]	derived
Variance of surface elevation	$Var\{z(\mathbf{x}_R, t)\}$	0.020620	[m^2]	derived
Sample variance of z	s_z^2	0.016873	[m^2]	derived
Sample significant wave height	$\hat{H}_{m_0}$	0.519591	[m]	derived
Azimuth SAR resolution	ρ_a	12.77411	[m]	derived
Vector of radar LOS	v_{LOS}	$\left[\frac{\sqrt{2}}{2}, 0, -\frac{\sqrt{2}}{2}\right]^T$	unitary	derived

Table 6. The RTW-R16 scenario: input and derived parameters. First modification of R/V.

Description	Name(s)	Value(s)	Units	Parameter
Wind direction	ϕ_w	$\pi/9$	[rad]	input
Azimuthal look direction	ϕ_0	0	[rad]	input
Slant range	R	18×10^3	[m]	input
Range-to-velocity ratio	R/V	90	[s]	derived
Variance of surface elevation	$Var\{z(\mathbf{x}_R,t)\}$	0.020620	[m^2]	derived
Sample variance of z	s_z^2	0.016873	[m^2]	derived
Sample significant wave height	$\hat{H}_{m_0}$	0.519591	[m]	derived
Azimuth SAR resolution	ρ_a	14.37087	[m]	derived
Vector of radar LOS	v_{LOS}	$\left[\frac{\sqrt{2}}{2}, 0, -\frac{\sqrt{2}}{2}\right]^T$	unitary	derived

Table 7. The RTW-R18 scenario: input and derived parameters. Second modification of R/V.

Description	Name(s)	Value(s)	Units	Parameter
Wind direction	ϕ_w	0	[rad]	input
Azimuthal look direction	ϕ_0	$\pi/2$	[rad]	input
Slant range	R	15×10^3	[m]	input
Range-to-velocity ratio	R/V	75	[s]	derived
Variance of surface elevation	$Var\{z(\mathbf{x}_R,t)\}$	0.020575	[m^2]	derived
Sample variance of z	s_z^2	0.021478	[m^2]	derived
Sample significant wave height	$\hat{H}_{m_0}$	0.586215	[m]	derived
Azimuth SAR resolution	ρ_a	11.97573	[m]	derived
Vector of radar LOS	v_{LOS}	$\left[0, \frac{\sqrt{2}}{2}, -\frac{\sqrt{2}}{2}\right]^T$	unitary	derived

Table 8. The ATW scenario: input and derived parameters.

Description	Name(s)	Value(s)	Units	Parameter
Wind direction	ϕ_w	$\pi/9$	[rad]	input
Azimuthal look direction	ϕ_0	$\pi/2$	[rad]	input
Slant range	R	16×10^3	[m]	input
Range-to-velocity ratio	R/V	80	[s]	derived
Variance of surface elevation	$Var\{z(\mathbf{x}_R,t)\}$	0.020620	[m^2]	derived
Sample variance of z	s_z^2	0.016873	[m^2]	derived
Sample significant wave height	$\hat{H}_{m_0}$	0.519591	[m]	derived
Azimuth SAR resolution	ρ_a	12.77411	[m]	derived
Vector of radar LOS	v_{LOS}	$\left[0, \frac{\sqrt{2}}{2}, -\frac{\sqrt{2}}{2}\right]^T$	unitary	derived

Table 9. The ATW-R16 scenario: input and derived parameters. First modification of R/V.

Each value of ϕ_0 allows to select different mechanisms of the ocean surface: in the RTW scenario, there is a stronger influence of tilt and hydrodynamic modulations; in the ATW scenario, there is a stronger influence of azimuthal smearing and velocity bunching. Also, if ϕ_w is not parallel to the range or azimuth directions, the respective variations of RTW and ATW make each inversion problem more challenging, because the mechanisms of both directions get combined. Finally, if the ratio R/V increases, velocity bunching is stronger. See (Alpers, 1983; Brüning et al., 1990; Mingquan Bao et al., 1997).

Description	Name(s)	Value(s)	Units	Parameter
Wind direction	ϕ_w	$\pi/9$	[rad]	input
Azimuthal look direction	ϕ_0	$\pi/2$	[rad]	input
Slant range	R	18×10^3	[m]	input
Range-to-velocity ratio	R/V	90	[s]	derived
Variance of surface elevation	$Var\{z(\mathbf{x}_R, t)\}$	0.020620	[m^2]	derived
Sample variance of z	s_z^2	0.016873	[m^2]	derived
Sample significant wave height	$\hat{H}_{m_0}$	0.519591	[m]	derived
Azimuth SAR resolution	ρ_a	14.37087	[m]	derived
Vector of radar LOS	v_{LOS}	$\left[0, \frac{\sqrt{2}}{2}, -\frac{\sqrt{2}}{2}\right]^T$	unitary	derived

Table 10. The ATW-R18 scenario: input and derived parameters. Second modification of R/V.

7.2 The RTW-R16 scenario

Figure 11. The RTW-R16 scenario: its most relevant fields and spectra.

436 **Solution under the RTW-R16 scenario**

Figure 12. PROBLEM 64 VIA FM. Top: radial velocity u_r (black), initial point ${u_r}^0$ (**blue**), interferometric velocity u_{ATI} (**violet**), estimated radial velocity ${u_r}^*$ (**red**); Middle: Re$\{D\}$ (**black**), Re$\{I_0\}$ (**blue**), Re$\{I_{ATI}\}$ (**violet**), Re$\{I_*\}$ (**red**); Bottom: Im$\{D\}$ (**black**), Im$\{I_0\}$ (**blue**), Im$\{I_{ATI}\}$ (**violet**), Im$\{I_*\}$ (**red**).

Figure 13. PROBLEM 80 VIA FM. Top: radial velocity u_r (black), initial point ${u_r}^0$ (**blue**), interferometric velocity u_{ATI} (**violet**), estimated radial velocity ${u_r}^*$ (**red**); Middle: Re$\{D\}$ (**black**), Re$\{I_0\}$ (**blue**), Re$\{I_{ATI}\}$ (**violet**), Re$\{I_*\}$ (**red**); Bottom: Im$\{D\}$ (**black**), Im$\{I_0\}$ (**blue**), Im$\{I_{ATI}\}$ (**violet**), Im$\{I_*\}$ (**red**).

437 ### 7.3 The RTW-R18 scenario

Figure 14. The RTW-R18 scenario: its most relevant fields and spectra.

438 **Solution under the RTW-R18 scenario**

Figure 15. PROBLEM 96 VIA FM. Top: radial velocity u_r (black), initial point ${u_r}^0$ (**blue**), interferometric velocity u_{ATI} (**violet**), estimated radial velocity ${u_r}^*$ (**red**); Middle: Re$\{D\}$ (**black**), Re$\{I_0\}$ (**blue**), Re$\{I_{ATI}\}$ (**violet**), Re$\{I_*\}$ (**red**); Bottom: Im$\{D\}$ (**black**), Im$\{I_0\}$ (**blue**), Im$\{I_{ATI}\}$ (**violet**), Im$\{I_*\}$ (**red**).

Figure 16. PROBLEM 112 VIA FM. Top: radial velocity u_r (black), initial point ${u_r}^0$ (**blue**), interferometric velocity u_{ATI} (**violet**), estimated radial velocity ${u_r}^*$ (**red**); Middle: Re$\{D\}$ (**black**), Re$\{I_0\}$ (**blue**), Re$\{I_{ATI}\}$ (**violet**), Re$\{I_*\}$ (**red**); Bottom: Im$\{D\}$ (**black**), Im$\{I_0\}$ (**blue**), Im$\{I_{ATI}\}$ (**violet**), Im$\{I_*\}$ (**red**).

439 ### 7.4 The ATW scenario

Figure 17. The ATW scenario: its most relevant fields and spectra.

440 **Solution under the ATW scenario**

Figure 18. PROBLEM 0 VIA FM. Top: radial velocity u_r (black), initial point ${u_r}^0$ (**blue**), interferometric velocity u_{ATI} (**violet**), estimated radial velocity ${u_r}^*$ (**red**); Middle: Re$\{D\}$ (**black**), Re$\{I_0\}$ (**blue**), Re$\{I_{ATI}\}$ (**violet**), Re$\{I_*\}$ (**red**); Bottom: Im$\{D\}$ (**black**), Im$\{I_0\}$ (**blue**), Im$\{I_{ATI}\}$ (**violet**), Im$\{I_*\}$ (**red**).

Figure 19. PROBLEM 16 VIA FM. Top: radial velocity u_r (black), initial point ${u_r}^0$ (**blue**), interferometric velocity u_{ATI} (**violet**), estimated radial velocity ${u_r}^*$ (**red**); Middle: Re$\{D\}$ (**black**), Re$\{I_0\}$ (**blue**), Re$\{I_{ATI}\}$ (**violet**), Re$\{I_*\}$ (**red**); Bottom: Im$\{D\}$ (**black**), Im$\{I_0\}$ (**blue**), Im$\{I_{ATI}\}$ (**violet**), Im$\{I_*\}$ (**red**).

441 ### 7.5 The ATW-R16 scenario

Figure 20. The ATW-R16 scenario: its most relevant fields and spectra.

442 **Solution under the ATW-R16 scenario**

Figure 21. PROBLEM 32 VIA FM. Top: radial velocity u_r (black), initial point ${u_r}^0$ (**blue**), interferometric velocity u_{ATI} (**violet**), estimated radial velocity ${u_r}^*$ (**red**); Middle: Re$\{D\}$ (**black**), Re$\{I_0\}$ (**blue**), Re$\{I_{ATI}\}$ (**violet**), Re$\{I_*\}$ (**red**); Bottom: Im$\{D\}$ (**black**), Im$\{I_0\}$ (**blue**), Im$\{I_{ATI}\}$ (**violet**), Im$\{I_*\}$ (**red**).

Figure 22. PROBLEM 48 VIA FM. Top: radial velocity u_r (black), initial point ${u_r}^0$ (**blue**), interferometric velocity u_{ATI} (**violet**), estimated radial velocity ${u_r}^*$ (**red**); Middle: Re$\{D\}$ (**black**), Re$\{I_0\}$ (**blue**), Re$\{I_{ATI}\}$ (**violet**), Re$\{I_*\}$ (**red**); Bottom: Im$\{D\}$ (**black**), Im$\{I_0\}$ (**blue**), Im$\{I_{ATI}\}$ (**violet**), Im$\{I_*\}$ (**red**).

443 ### 7.6 The ATW-R18 scenario

Figure 23. The ATW-R18 scenario: its most relevant fields and spectra.

444 **Solution under the ATW-R18 scenario**

Figure 24. PROBLEM 96 VIA FM. Top: radial velocity u_r (black), initial point ${u_r}^0$ (**blue**), interferometric velocity u_{ATI} (**violet**), estimated radial velocity ${u_r}^*$ (**red**); Middle: Re$\{D\}$ (**black**), Re$\{I_0\}$ (**blue**), Re$\{I_{ATI}\}$ (**violet**), Re$\{I_*\}$ (**red**); Bottom: Im$\{D\}$ (**black**), Im$\{I_0\}$ (**blue**), Im$\{I_{ATI}\}$ (**violet**), Im$\{I_*\}$ (**red**).

Figure 25. PROBLEM 112 VIA FM. Top: radial velocity u_r (black), initial point ${u_r}^0$ (**blue**), interferometric velocity u_{ATI} (**violet**), estimated radial velocity ${u_r}^*$ (**red**); Middle: Re$\{D\}$ (**black**), Re$\{I_0\}$ (**blue**), Re$\{I_{ATI}\}$ (**violet**), Re$\{I_*\}$ (**red**); Bottom: Im$\{D\}$ (**black**), Im$\{I_0\}$ (**blue**), Im$\{I_{ATI}\}$ (**violet**), Im$\{I_*\}$ (**red**).

Figure_01.

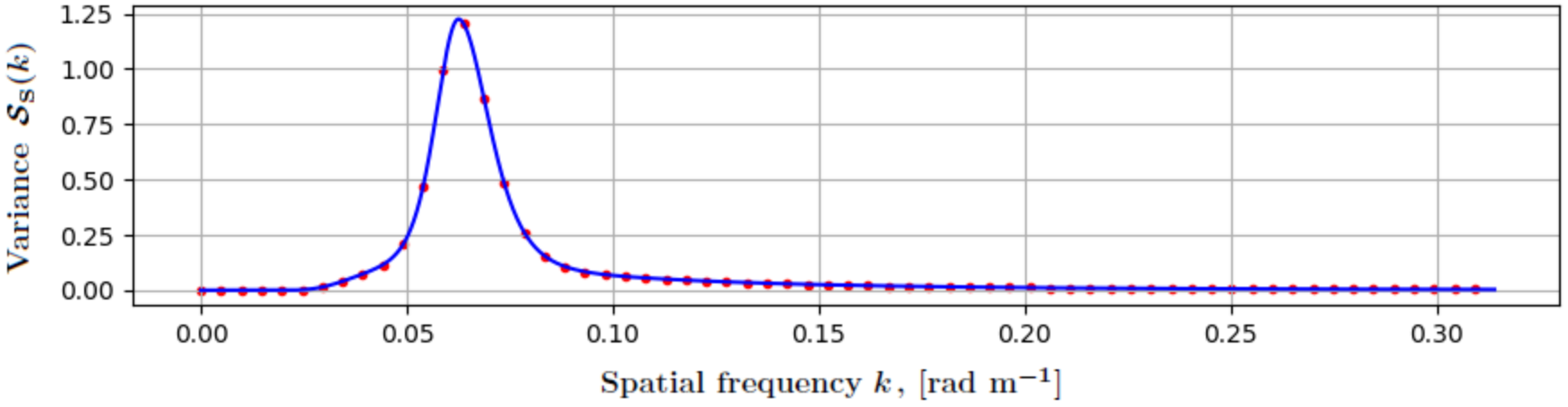
1.25
1.00
0.75
0.50
0.25
0.00
Variance $\mathcal{S}_{\mathrm{S}}(k)$
0.00
0.05
0.10
0.15
0.20
0.25
0.30
Spatial frequency k, [rad m^{-1}]

Figure_02.

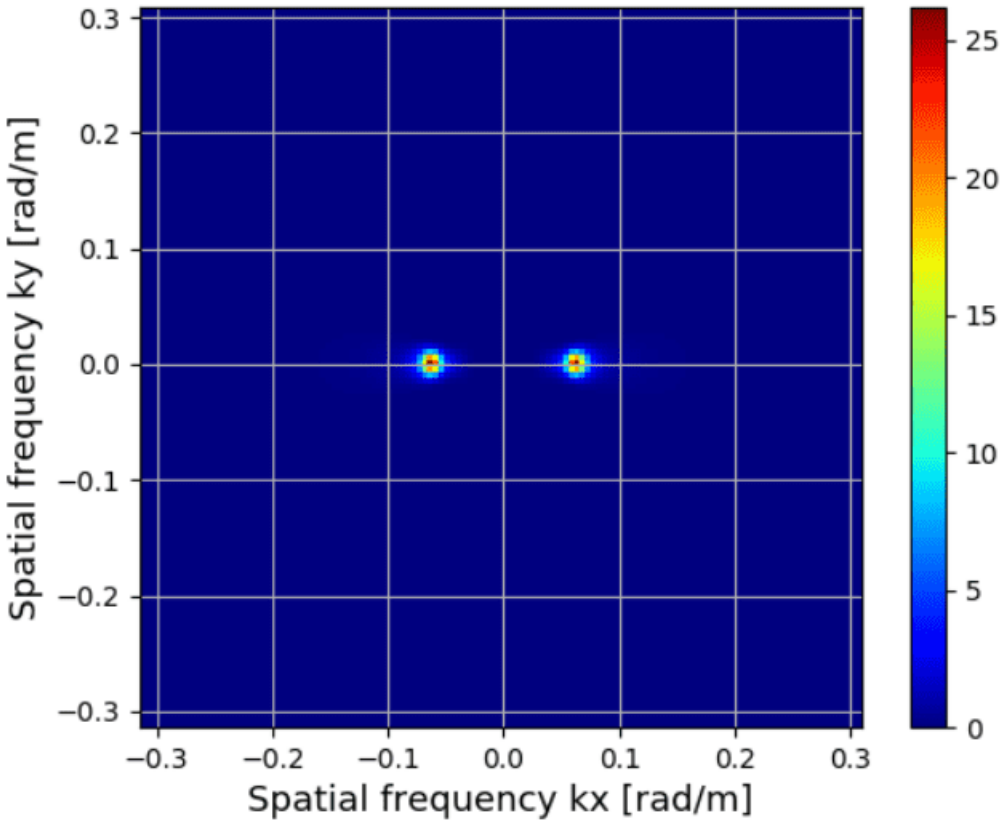

(a) Sampled directional spectrum $\hat{\mathscr{S}}_{2C}$.

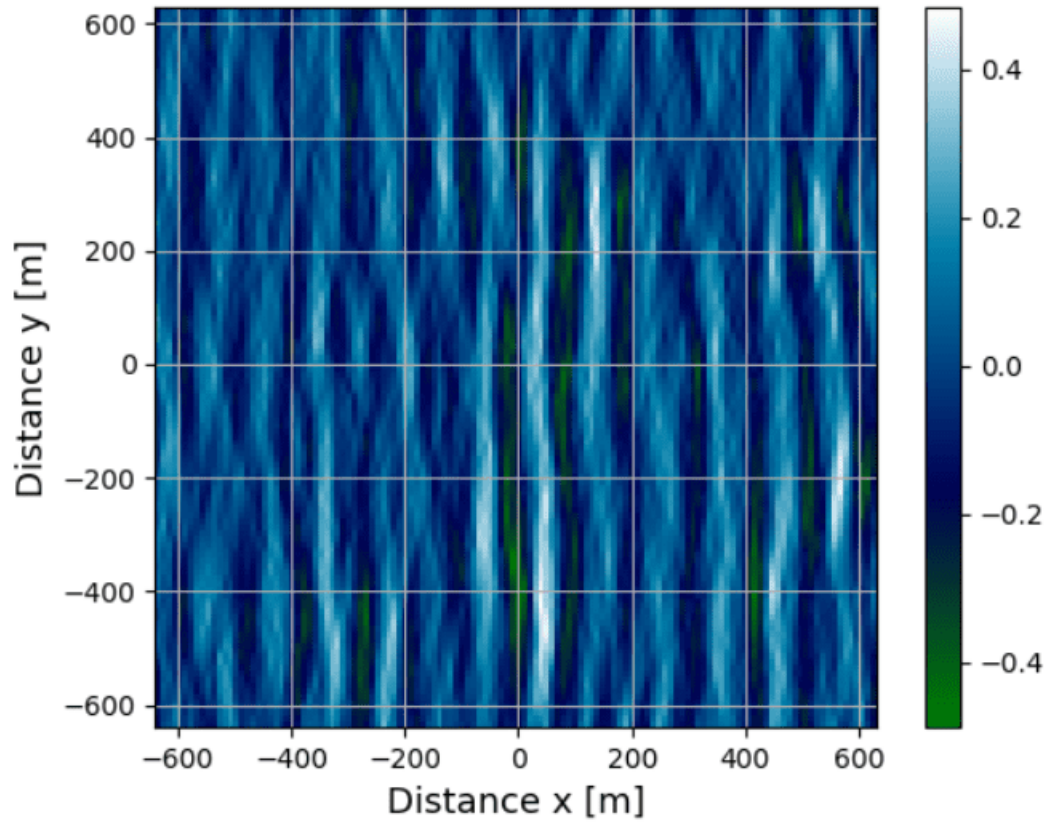

(b) The simulated ocean surface z.

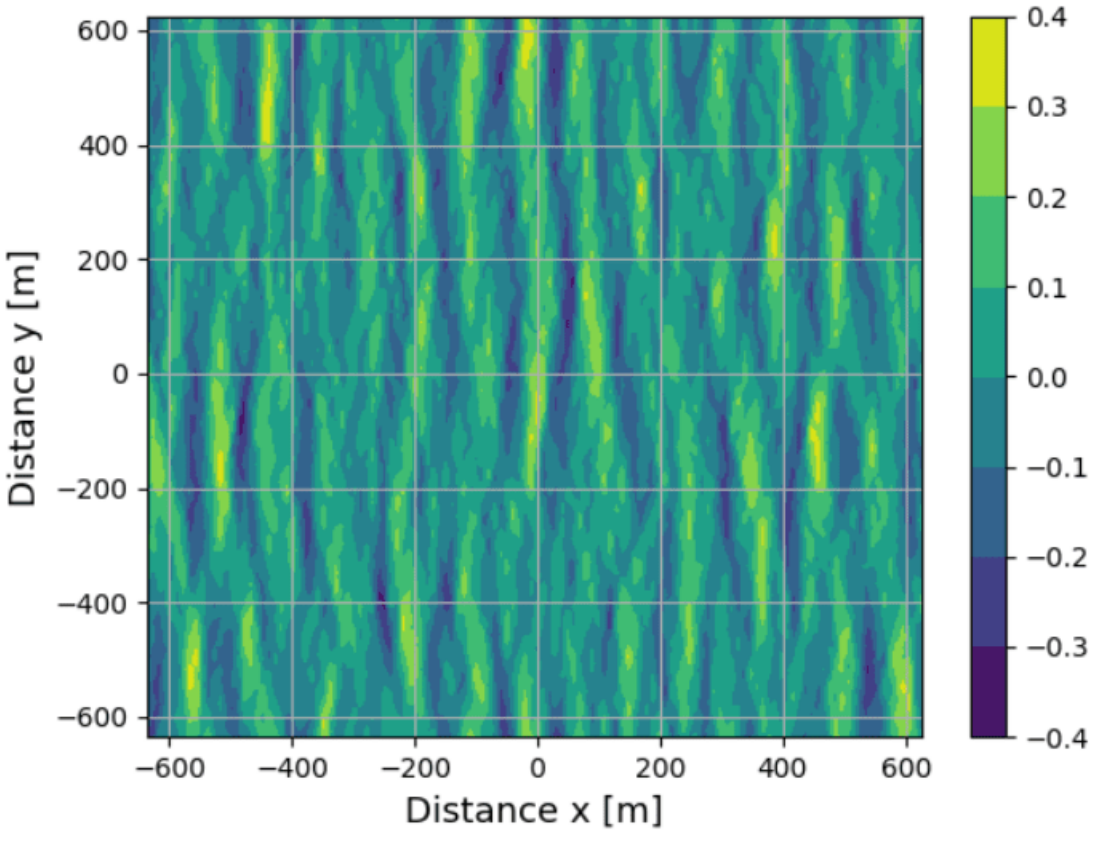

(c) Field of radial velocities u_r.

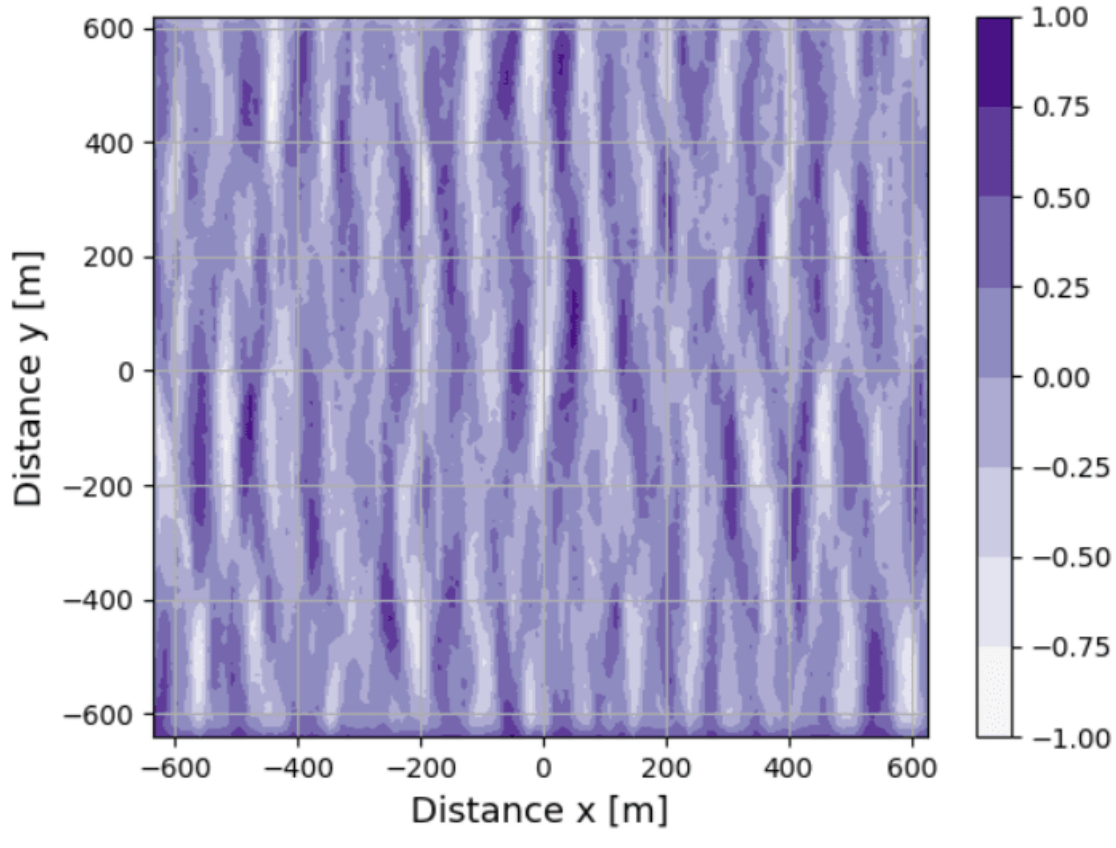

(d) The phase $\Phi_{ATI} = \angle D$.

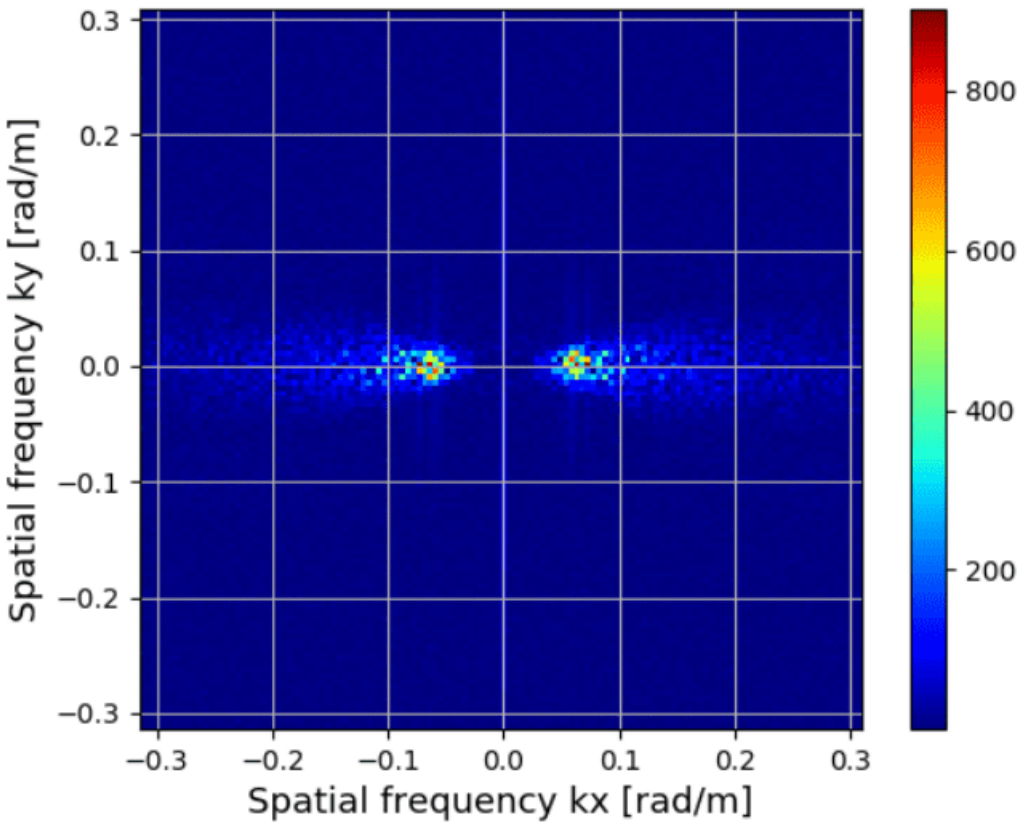

(e) The spectrum $\mathfrak{F}_D\{\Phi_{ATI}\}$.

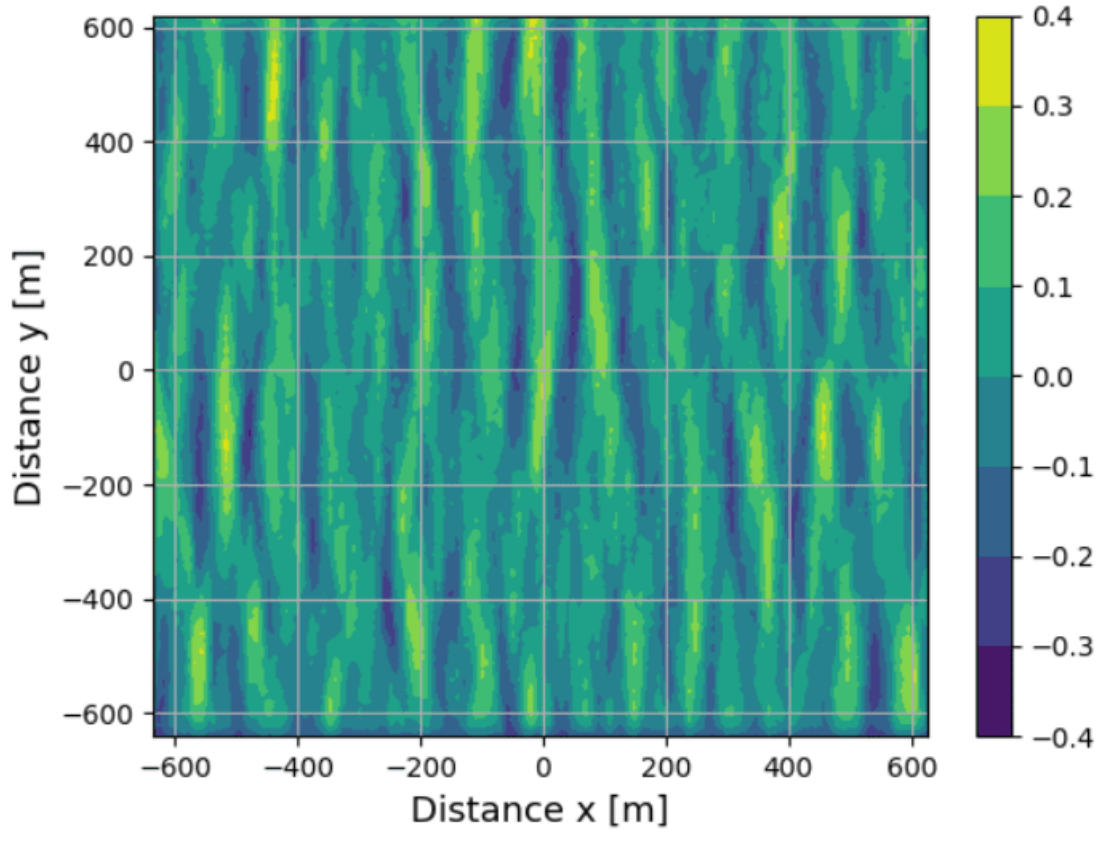

(f) The field u_{ATI}.

Figure_03.

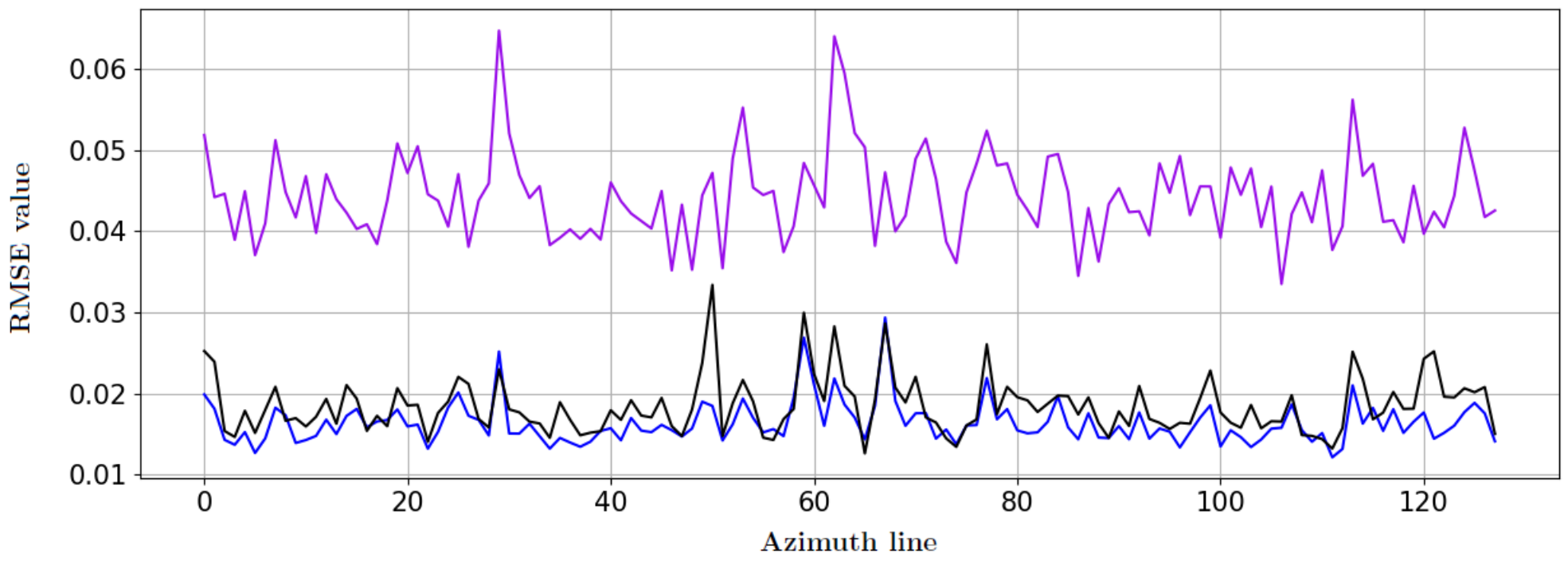
RMSE value
0.06
0.05
0.04
0.03
0.02
0.01
0
20
40
60
80
100
120
Azimuth line

Figure_04.

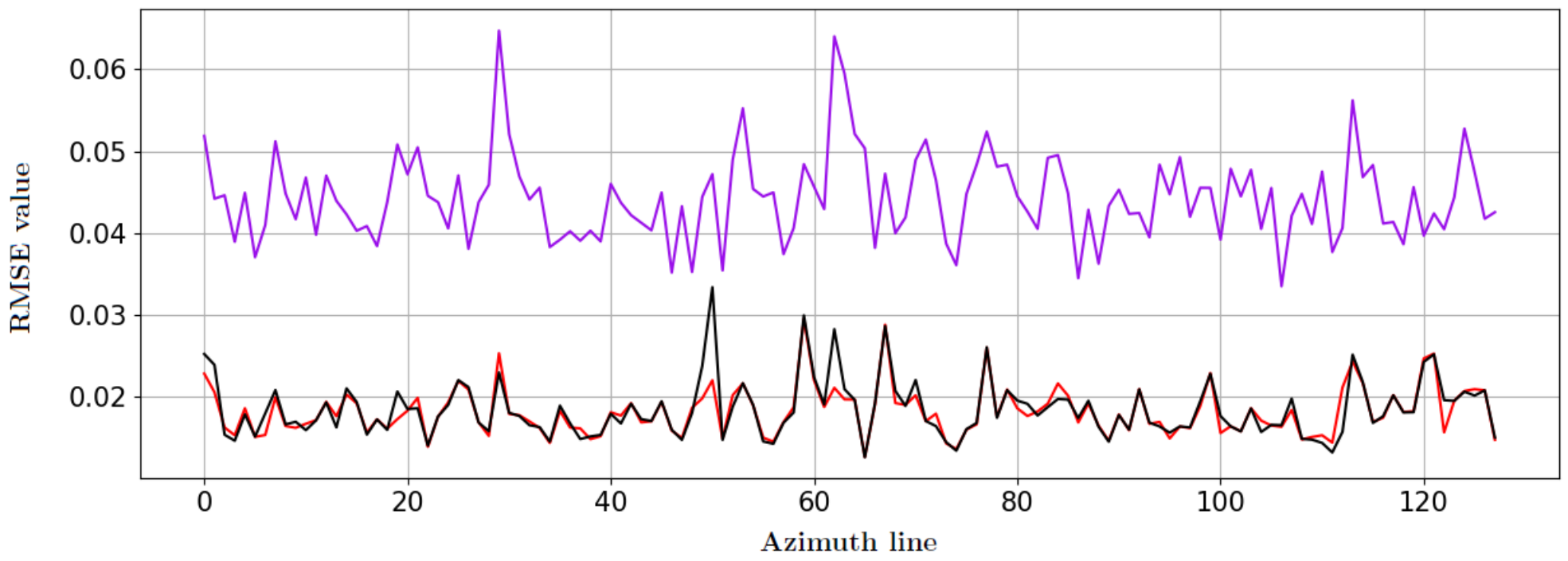
RMSE value
0.06
0.05
0.04
0.03
0.02
0
20
40
60
80
100
120
Azimuth line

Figure_05.

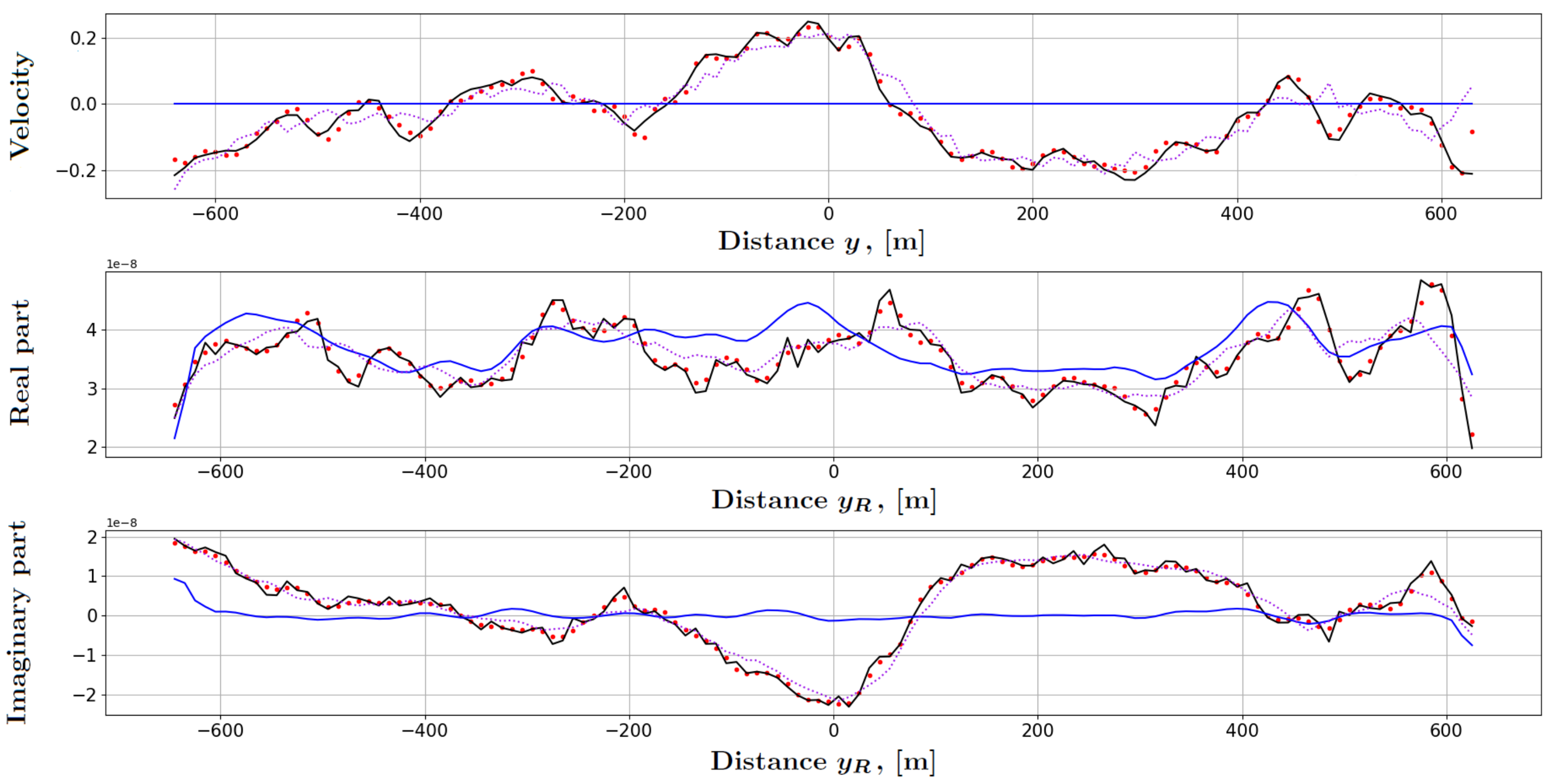
Velocity
0.2
0.0
−0.2
−600
−400
−200
0
200
400
600
Distance y, [m]
Real part
1e−8
4
3
2
Distance y_R, [m]
Imaginary part
1e−8
2
1
0
−1
−2
Distance y_R, [m]

Figure_06.

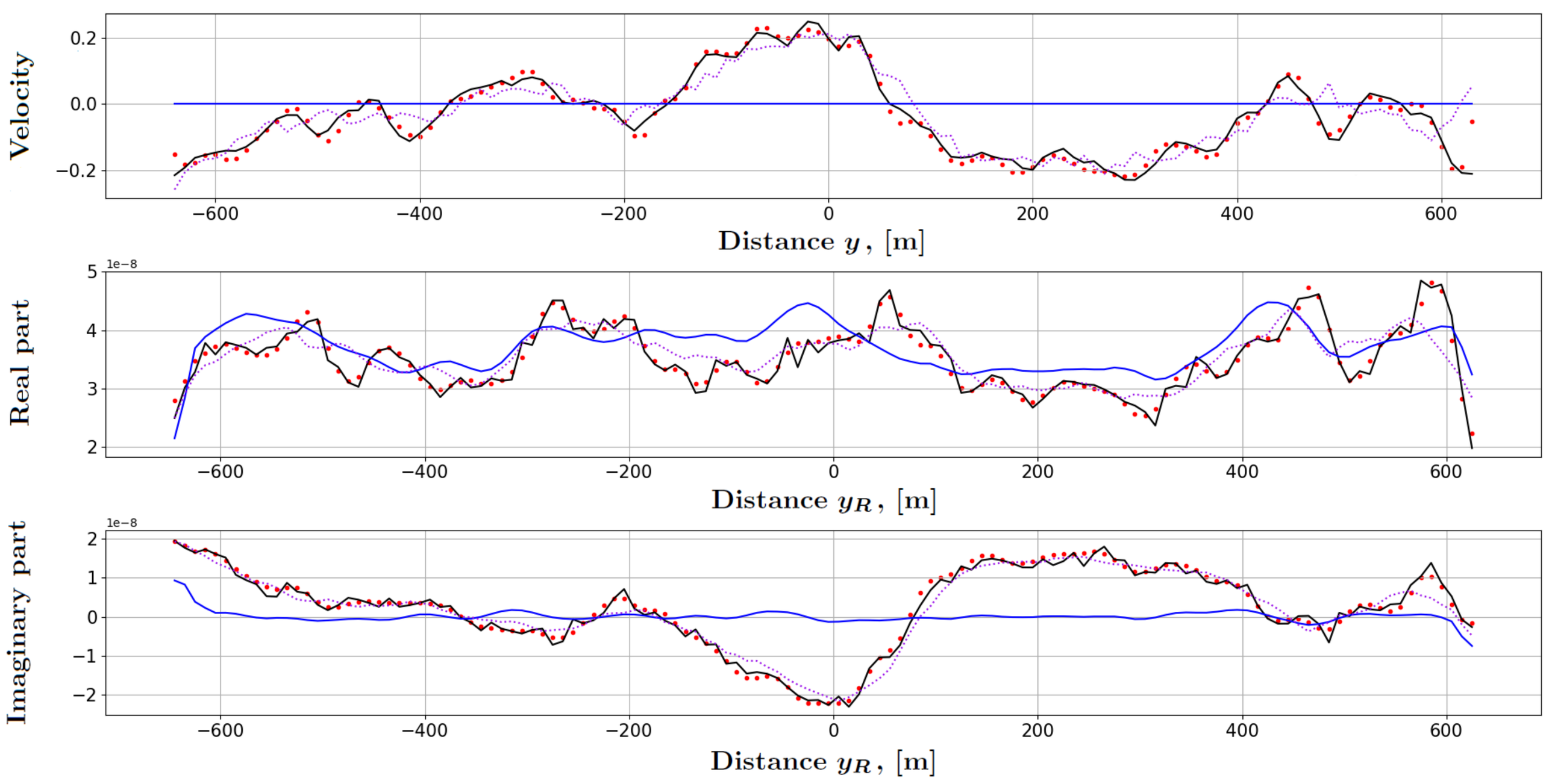
Velocity
0.2
0.0
−0.2
−600
−400
−200
0
200
400
600
Distance y, [m]
Real part
1e−8
5
4
3
2
−600
−400
−200
0
200
400
600
Distance y_R, [m]
Imaginary part
1e−8
2
1
0
−1
−2
−600
−400
−200
0
200
400
600
Distance y_R, [m]

Figure_07.

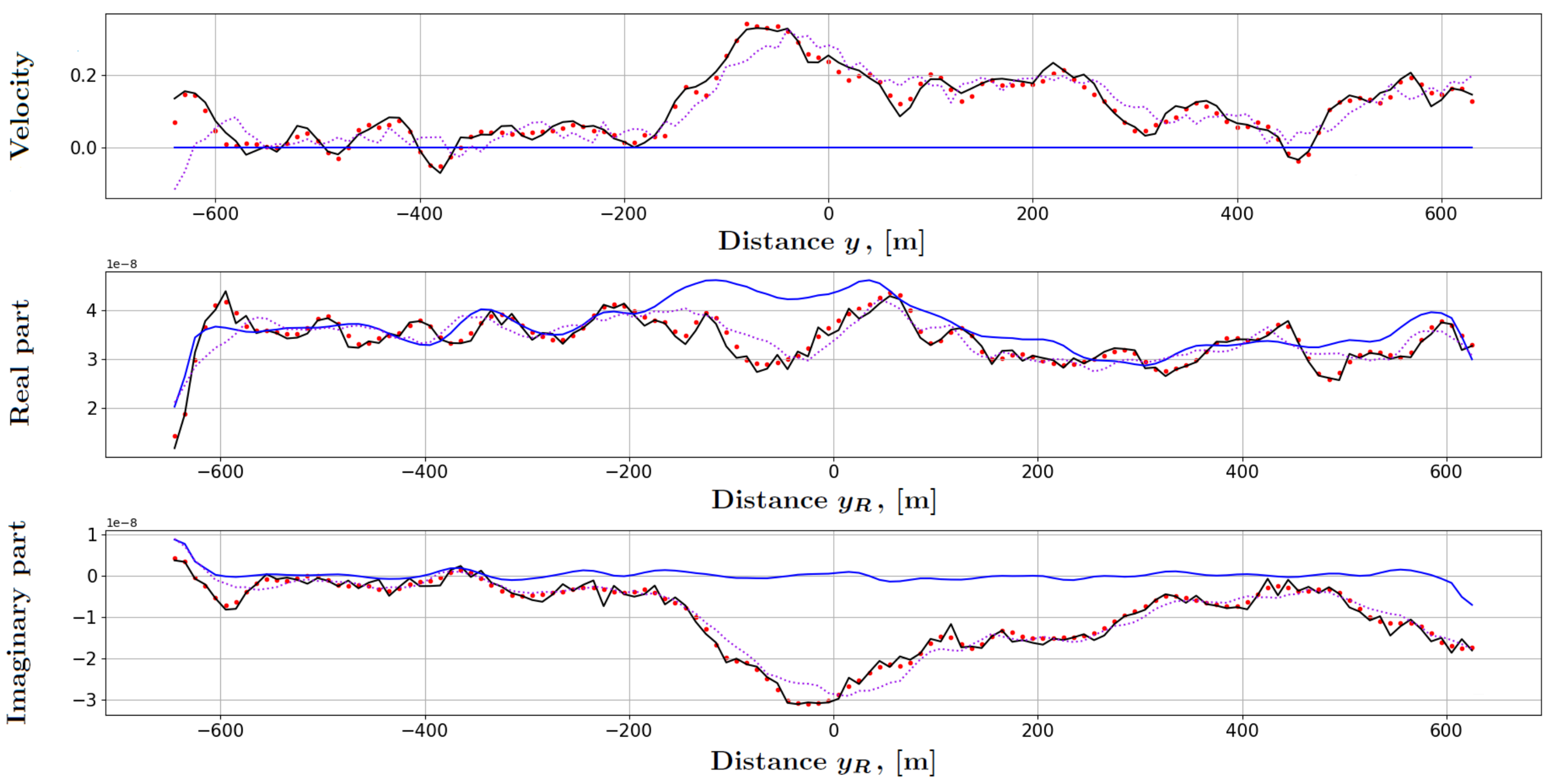
Velocity
0.2
0.0
−600
−400
−200
0
200
400
600
Distance y, [m]
1e−8
Real part
4
3
2
−600
−400
−200
0
200
400
600
Distance y_R, [m]
1e−8
Imaginary part
1
0
−1
−2
−3
−600
−400
−200
0
200
400
600
Distance y_R, [m]

Figure_08.

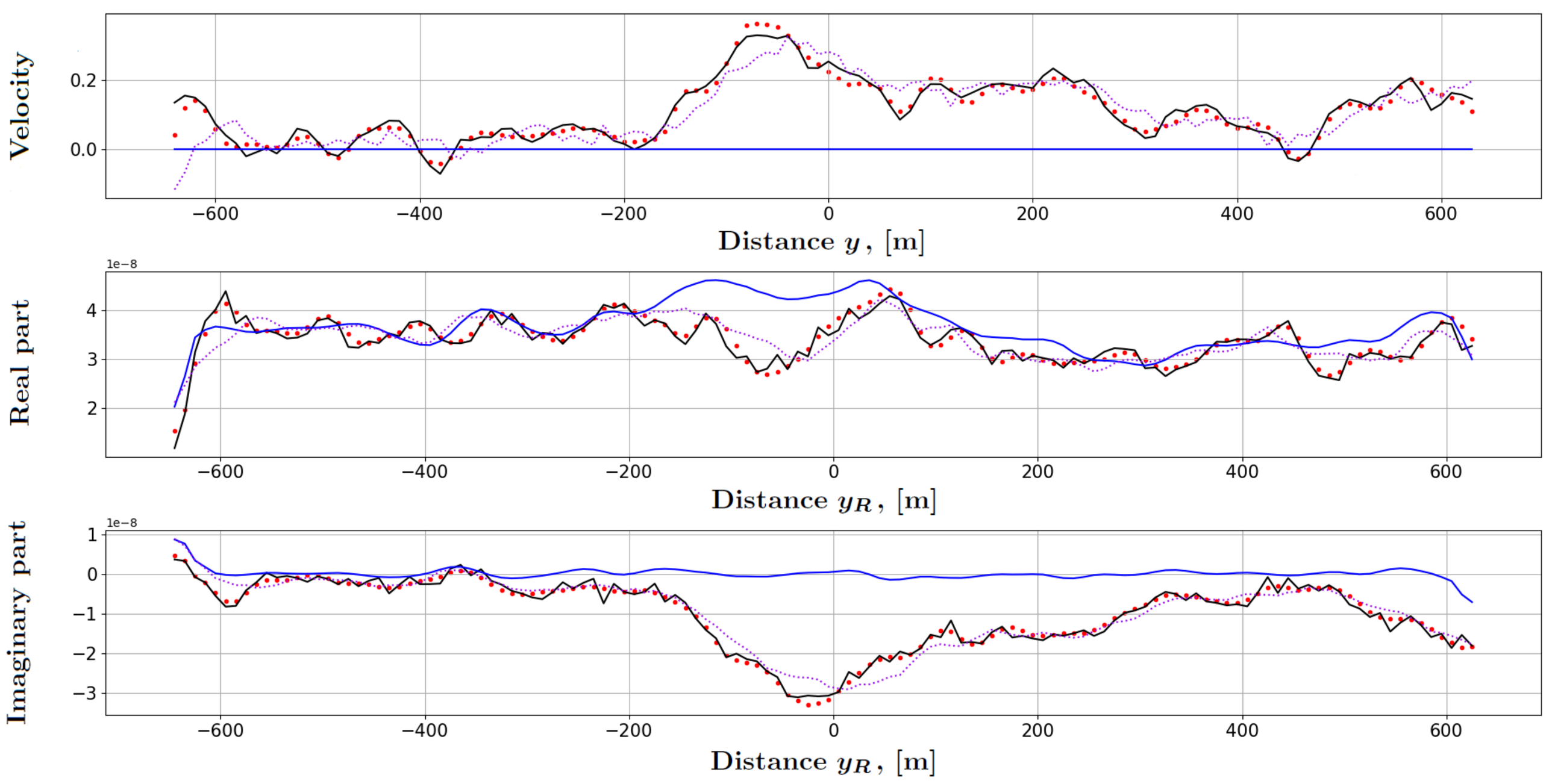
Velocity
0.2
0.0
−600
−400
−200
0
200
400
600
Distance y, [m]
1e−8
Real part
4
3
2
−600
−400
−200
0
200
400
600
Distance y_R, [m]
1e−8
Imaginary part
1
0
−1
−2
−3
−600
−400
−200
0
200
400
600
Distance y_R, [m]

Figure_09.

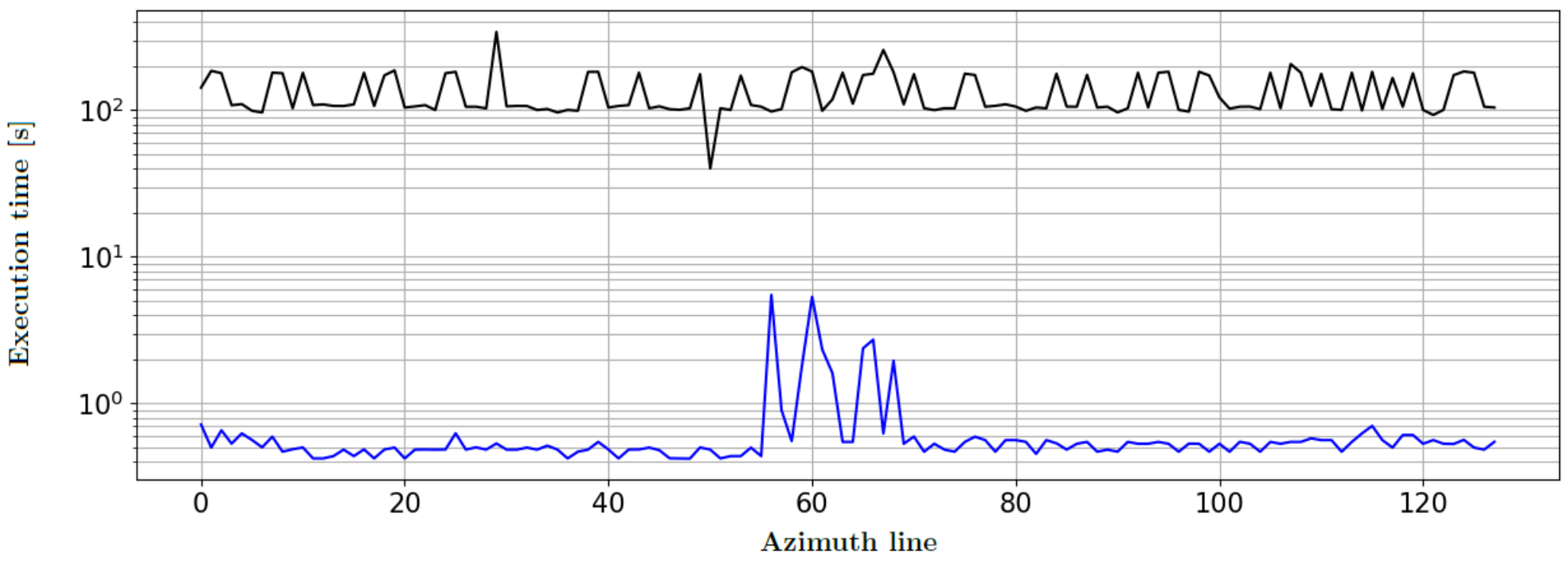
Execution time [s]
10^2
10^1
10^0
0
20
40
60
80
100
120
Azimuth line

Figure_10.

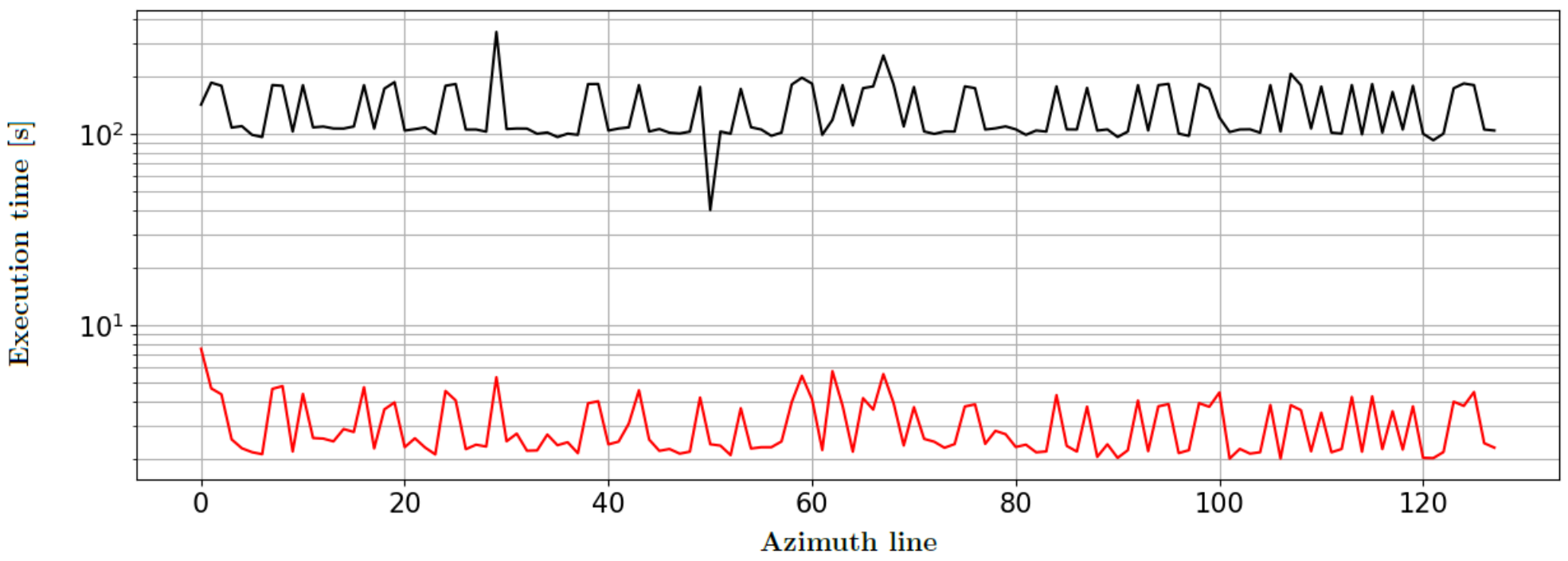
Execution time [s]
10^2
10^1
0
20
40
60
80
100
120
Azimuth line

Figure_11.

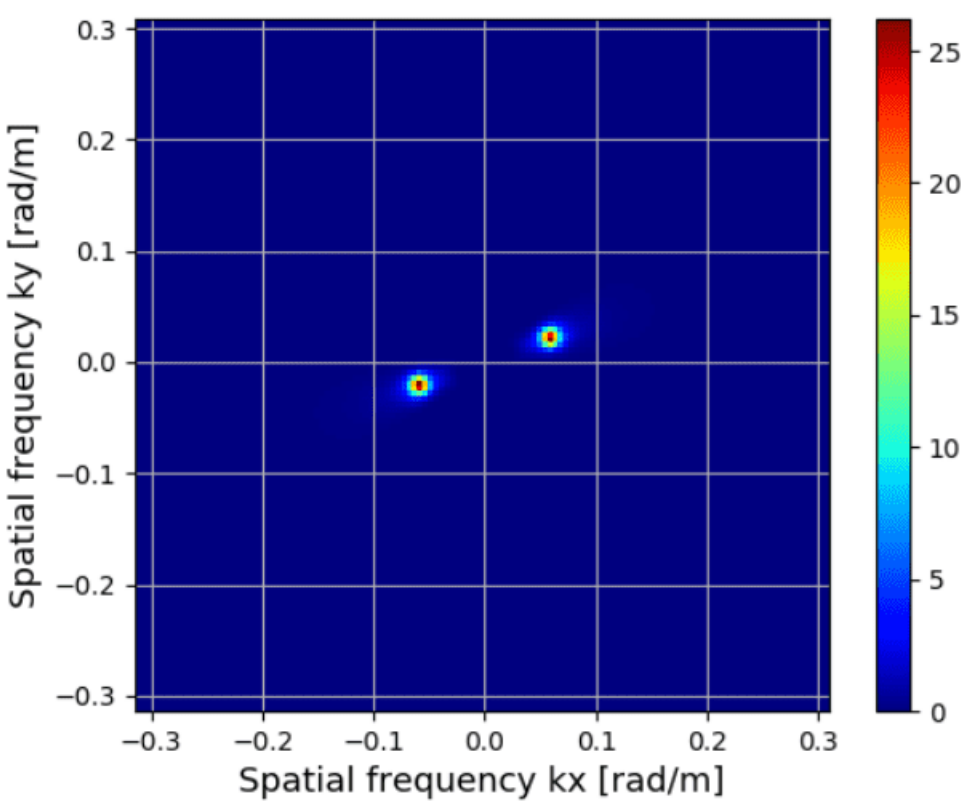

(a) Sampled directional spectrum $\hat{\mathscr{S}}_{2C}$.

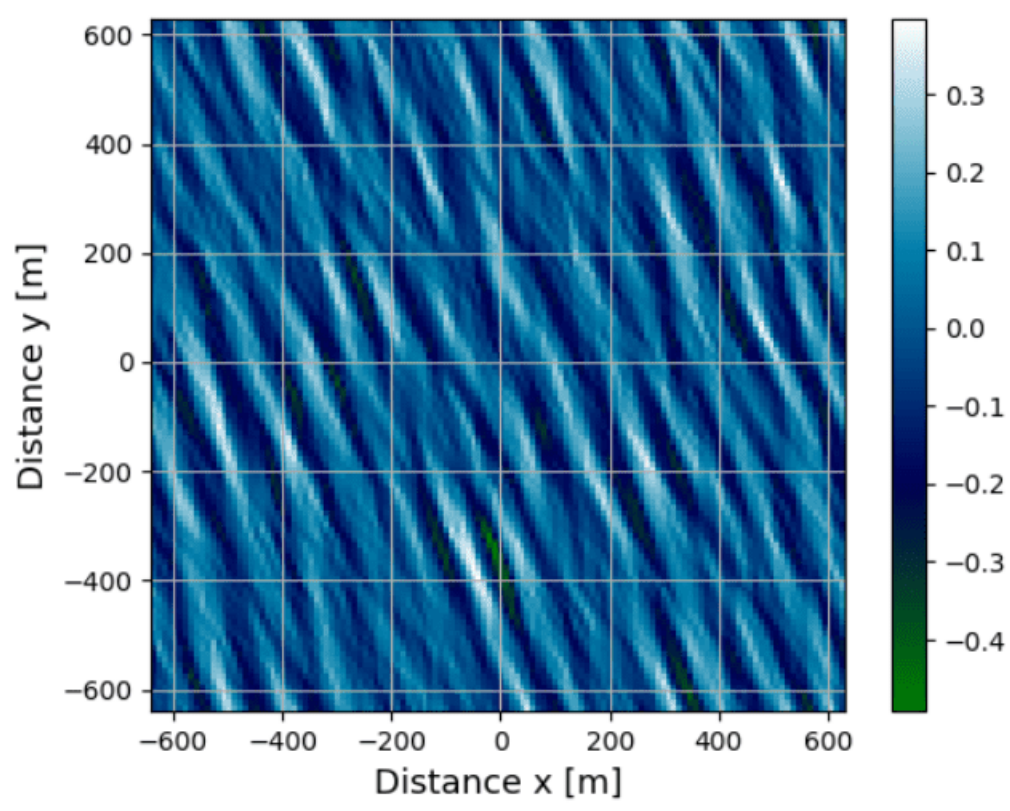

(b) The simulated ocean surface z.

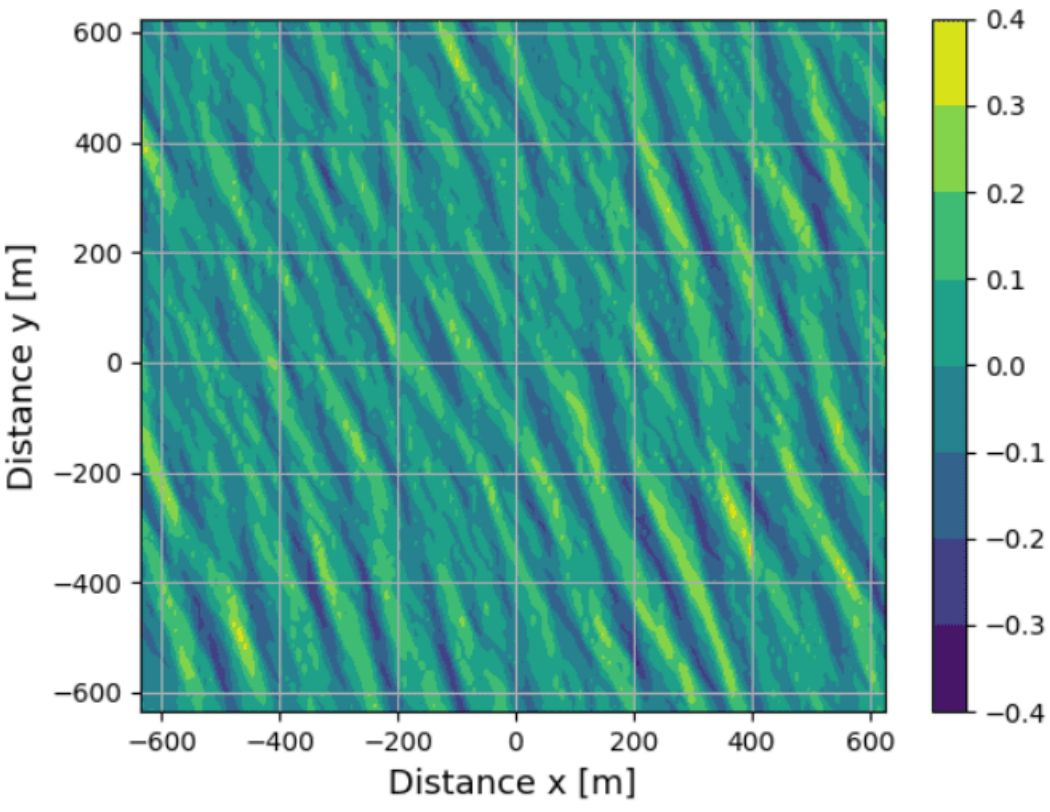

(c) Field of radial velocities u_r.

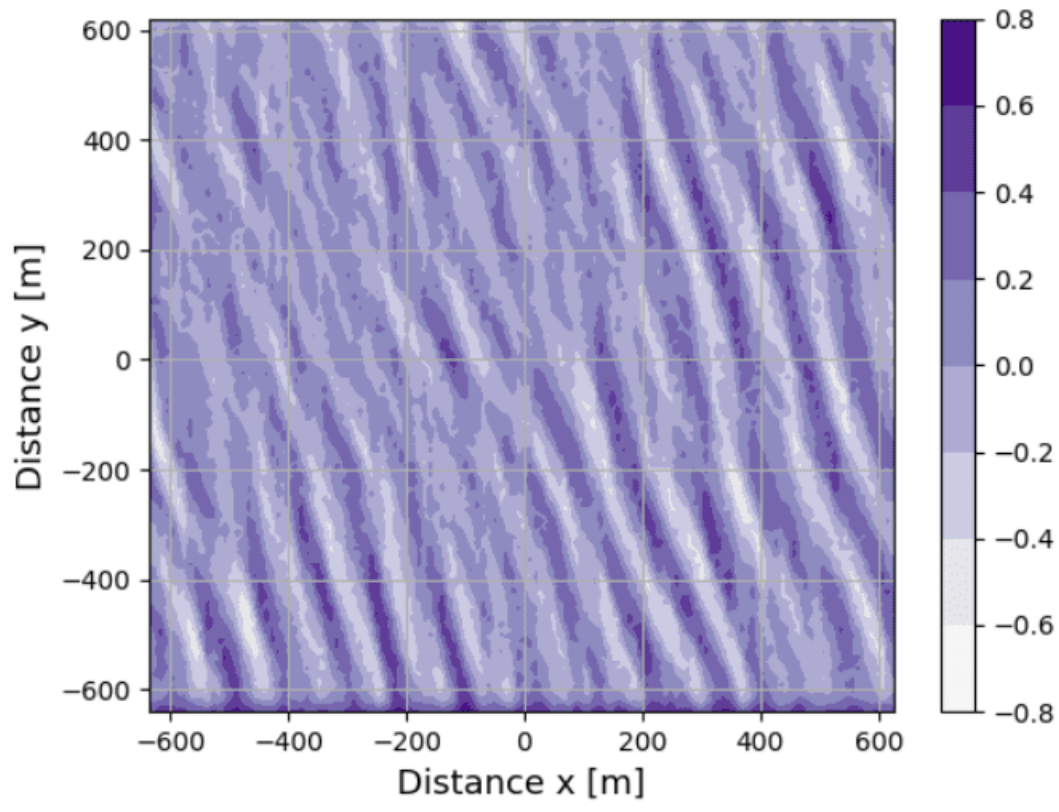

(d) The phase $\Phi_{ATI} = \angle D$.

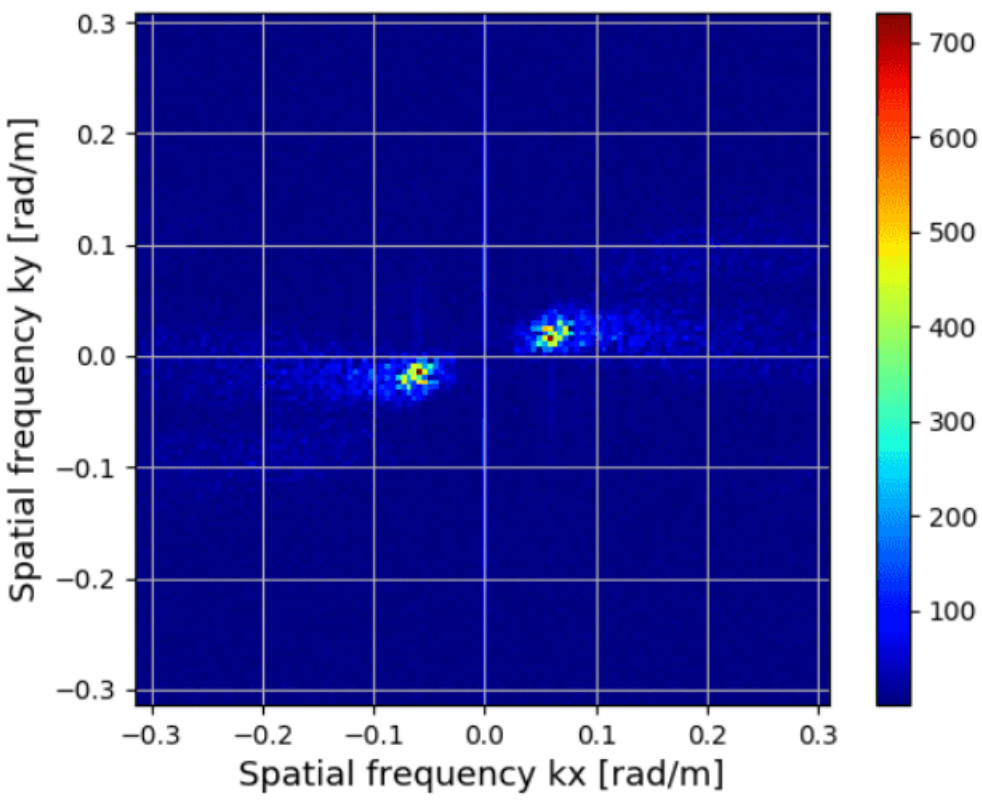

(e) The spectrum $\mathfrak{F}_D\{\Phi_{ATI}\}$.

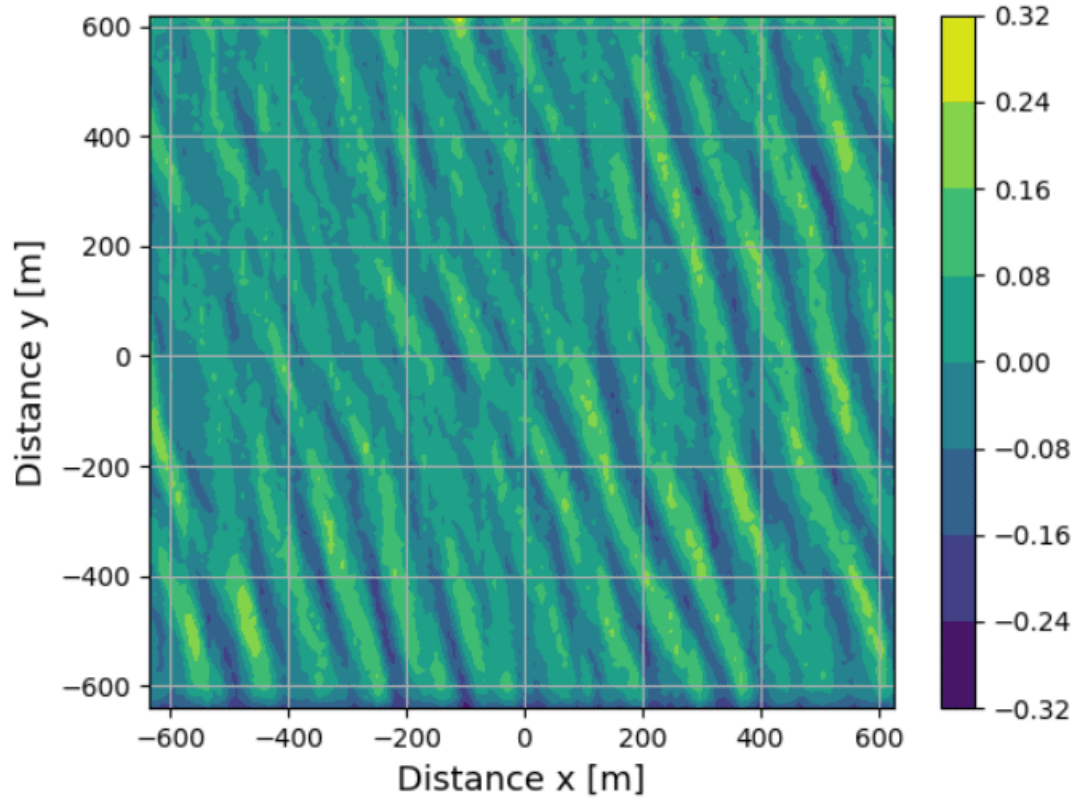

(f) The field u_{ATI}.

Figure_12.

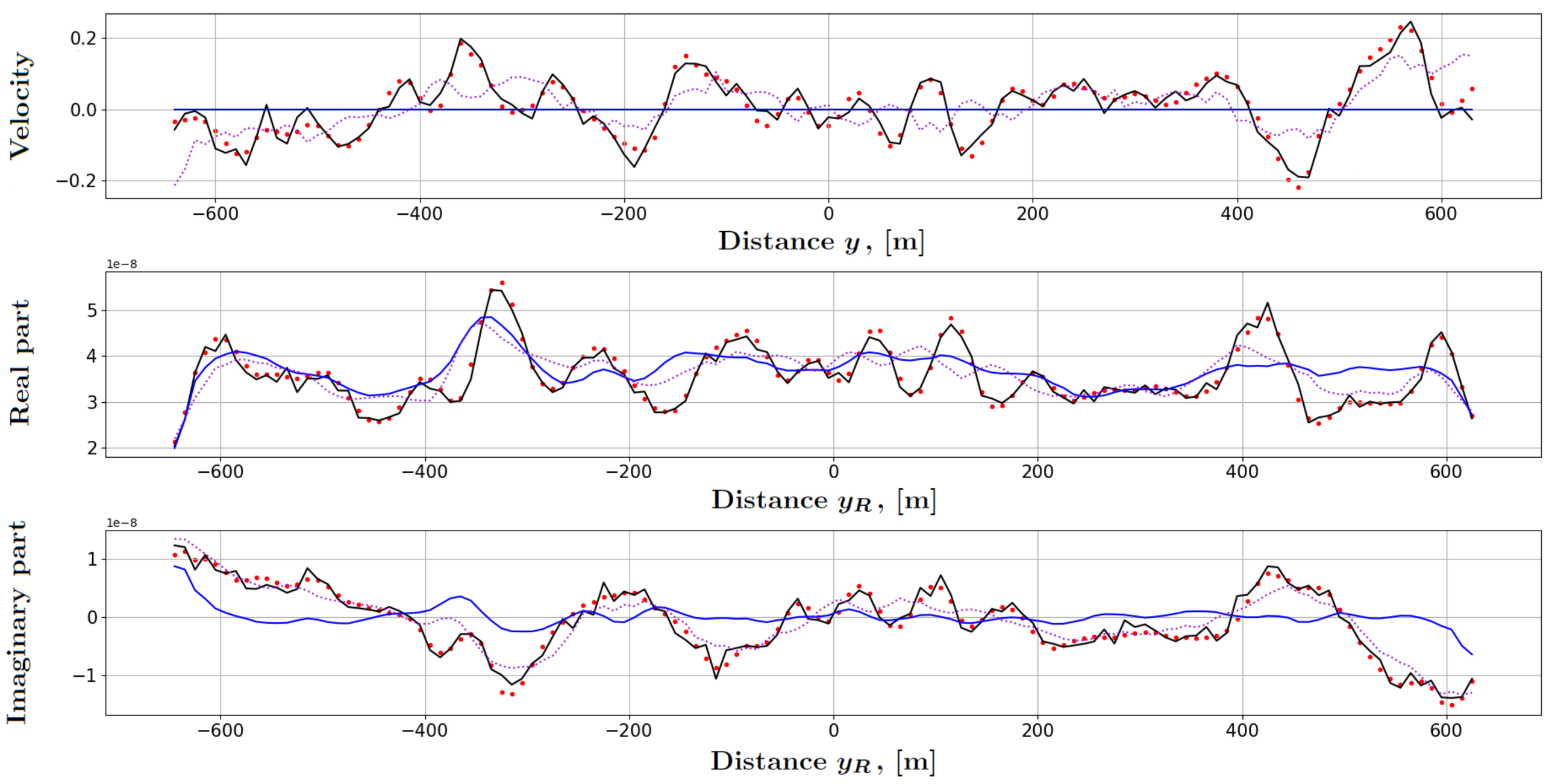
Velocity
0.2
0.0
−0.2
−600
−400
−200
0
200
400
600
Distance y, [m]
Real part
1e−8
5
4
3
2
−600
−400
−200
0
200
400
600
Distance y_R, [m]
Imaginary part
1e−8
1
0
−1
−600
−400
−200
0
200
400
600
Distance y_R, [m]

Figure_13.

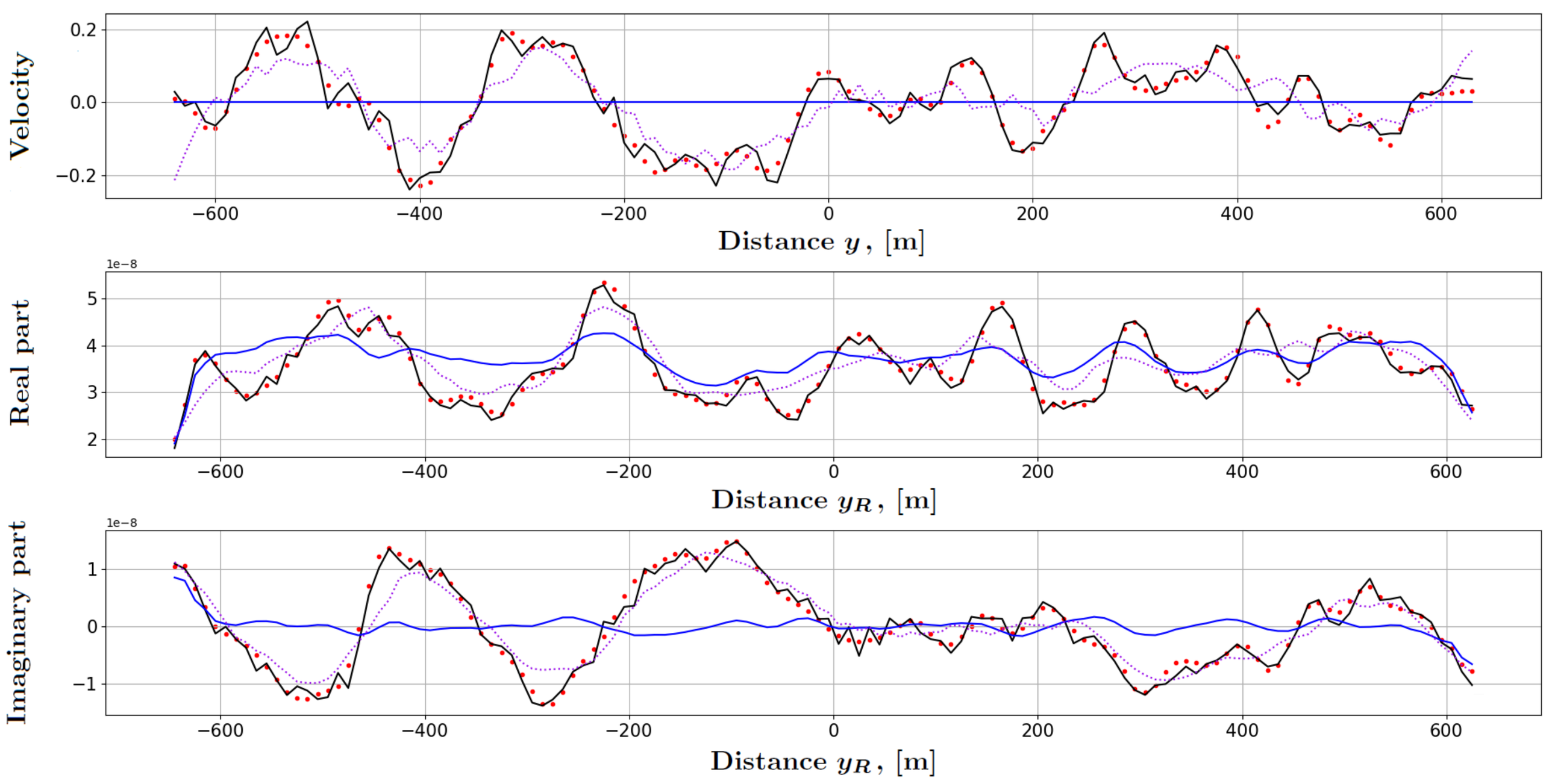
Velocity
0.2
0.0
−0.2
−600
−400
−200
0
200
400
600
Distance y, [m]
Real part
1e−8
5
4
3
2
−600
−400
−200
0
200
400
600
Distance y_R, [m]
Imaginary part
1e−8
1
0
−1
−600
−400
−200
0
200
400
600
Distance y_R, [m]

Figure_14.

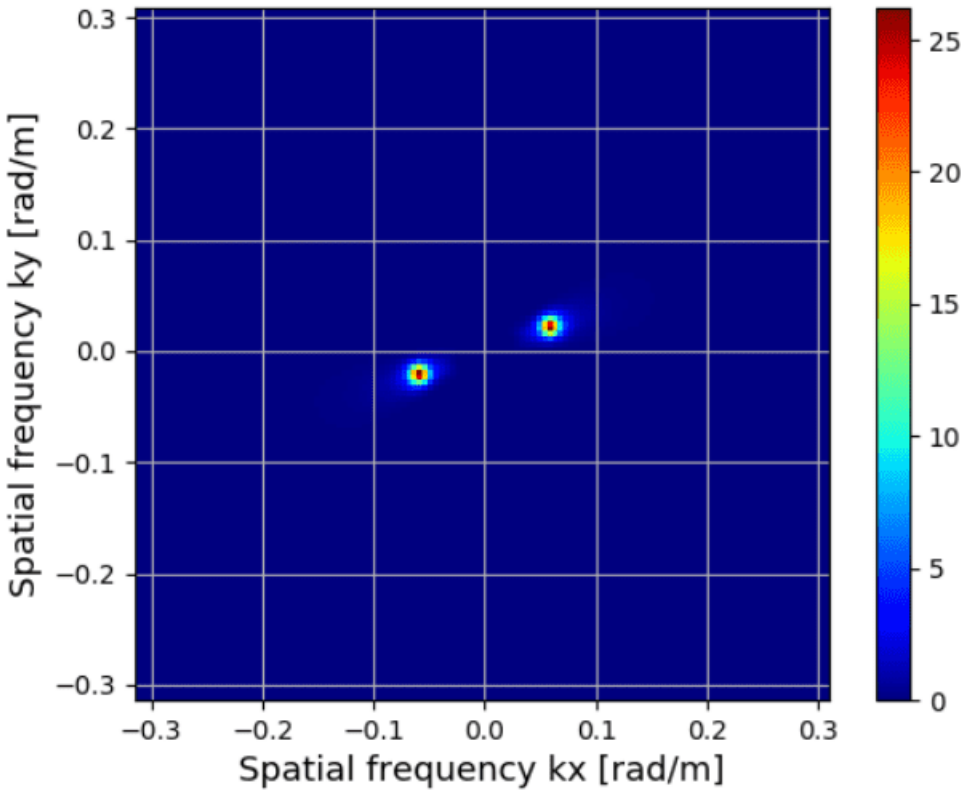

(a) Sampled directional spectrum $\hat{\mathscr{S}}_{2C}$.

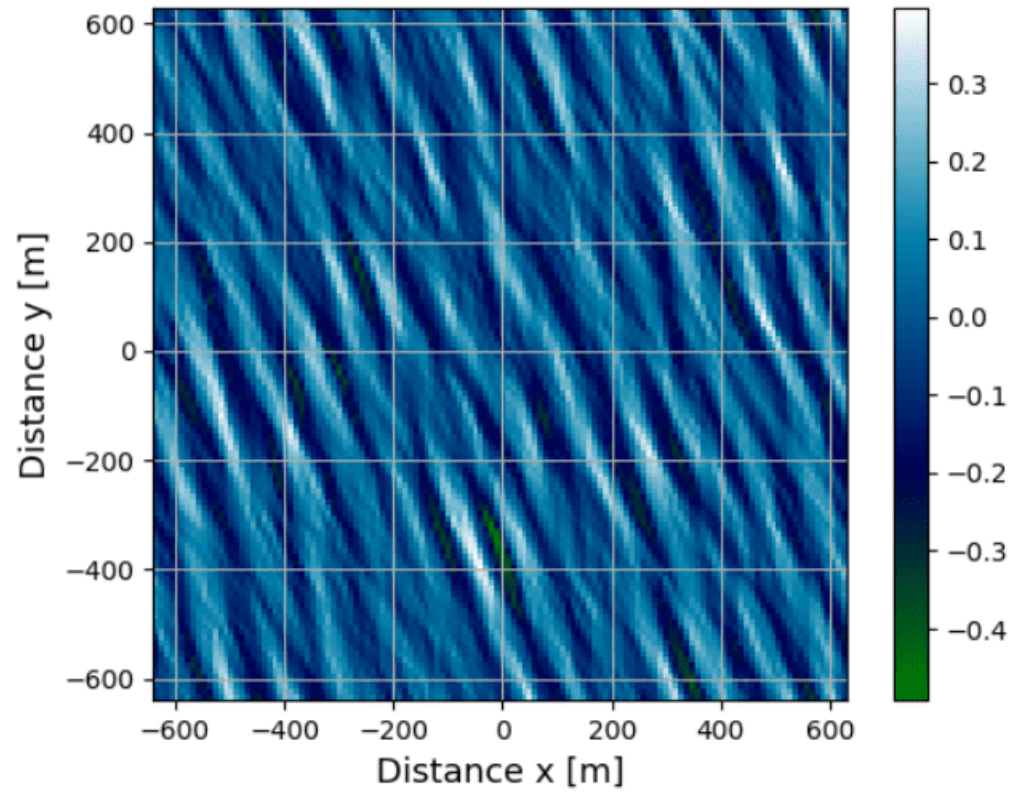

(b) The simulated ocean surface z.

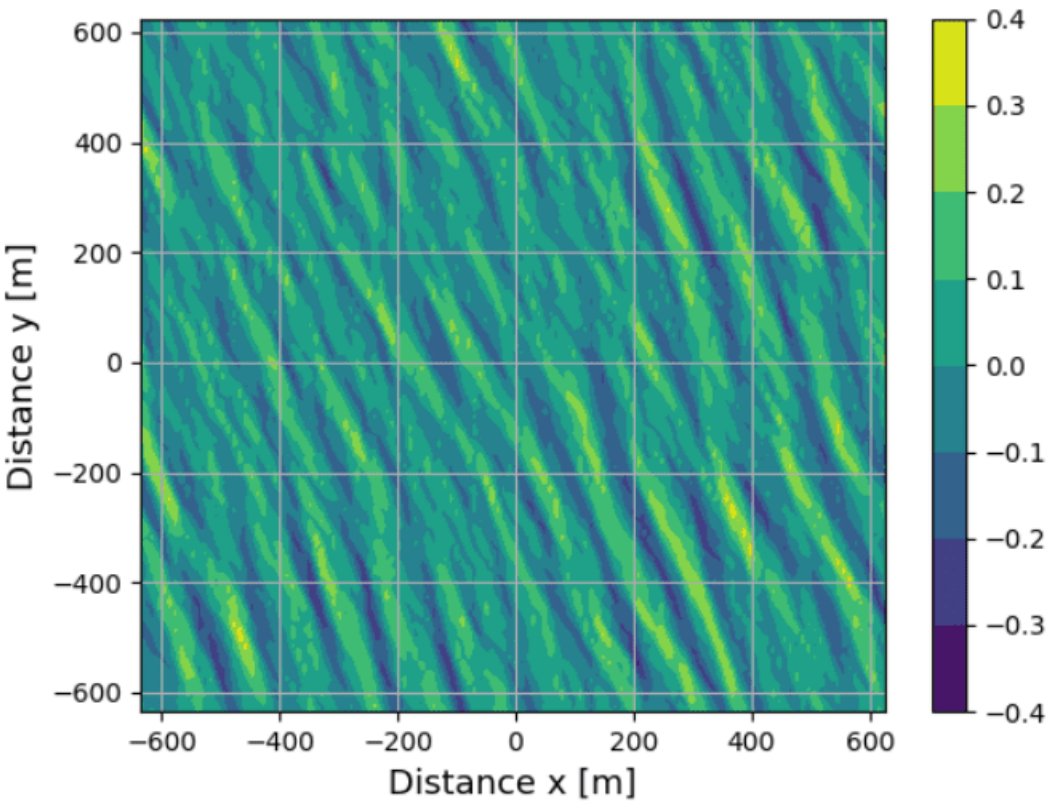

(c) Field of radial velocities u_r.

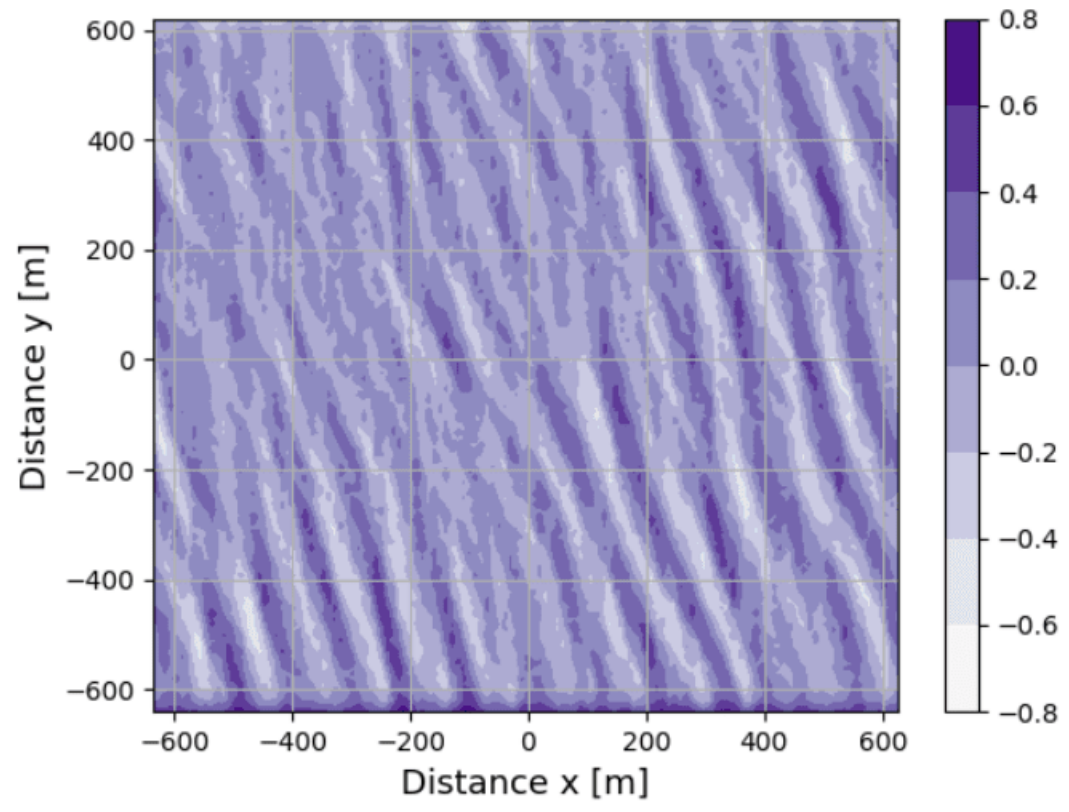

(d) The phase $\Phi_{ATI} = \angle D$.

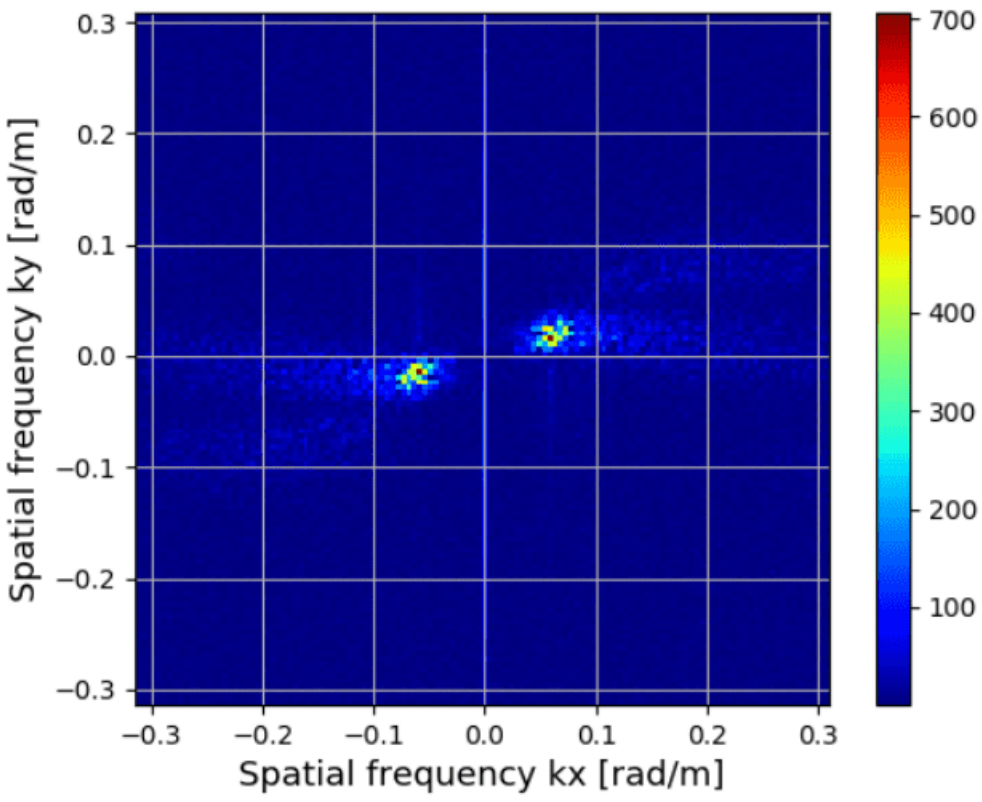

(e) The spectrum $\mathfrak{F}_D\{\Phi_{ATI}\}$.

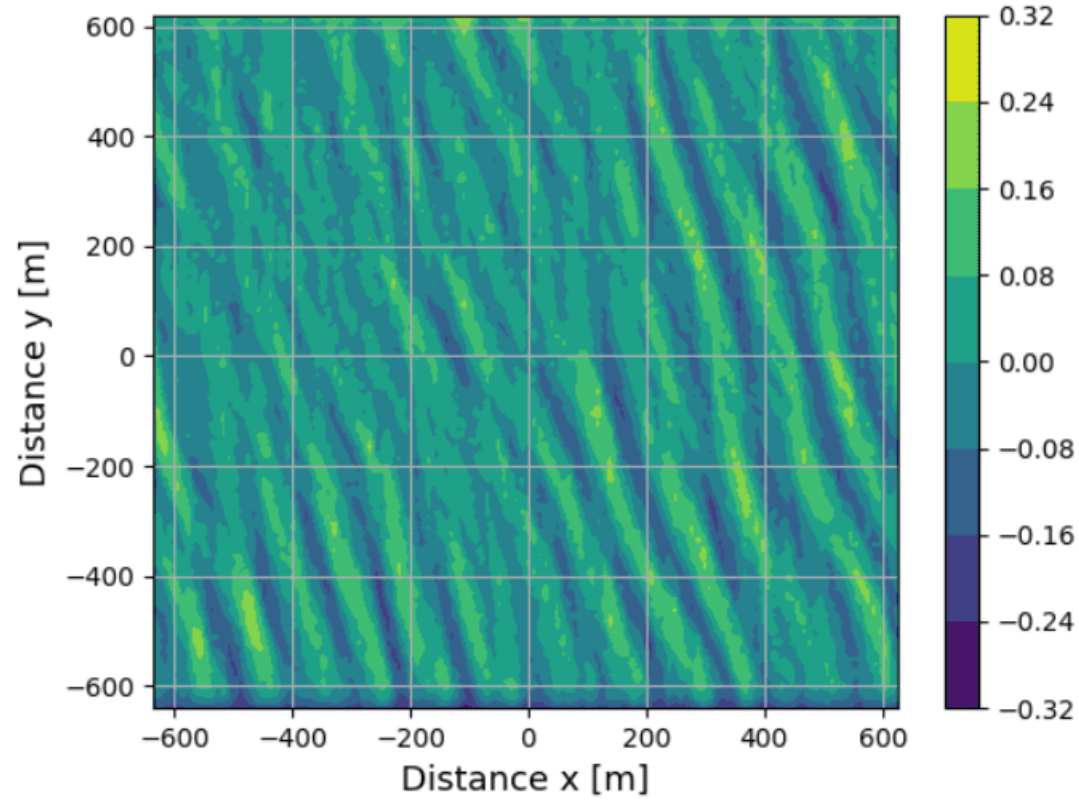

(f) The field u_{ATI}.

Figure_15.

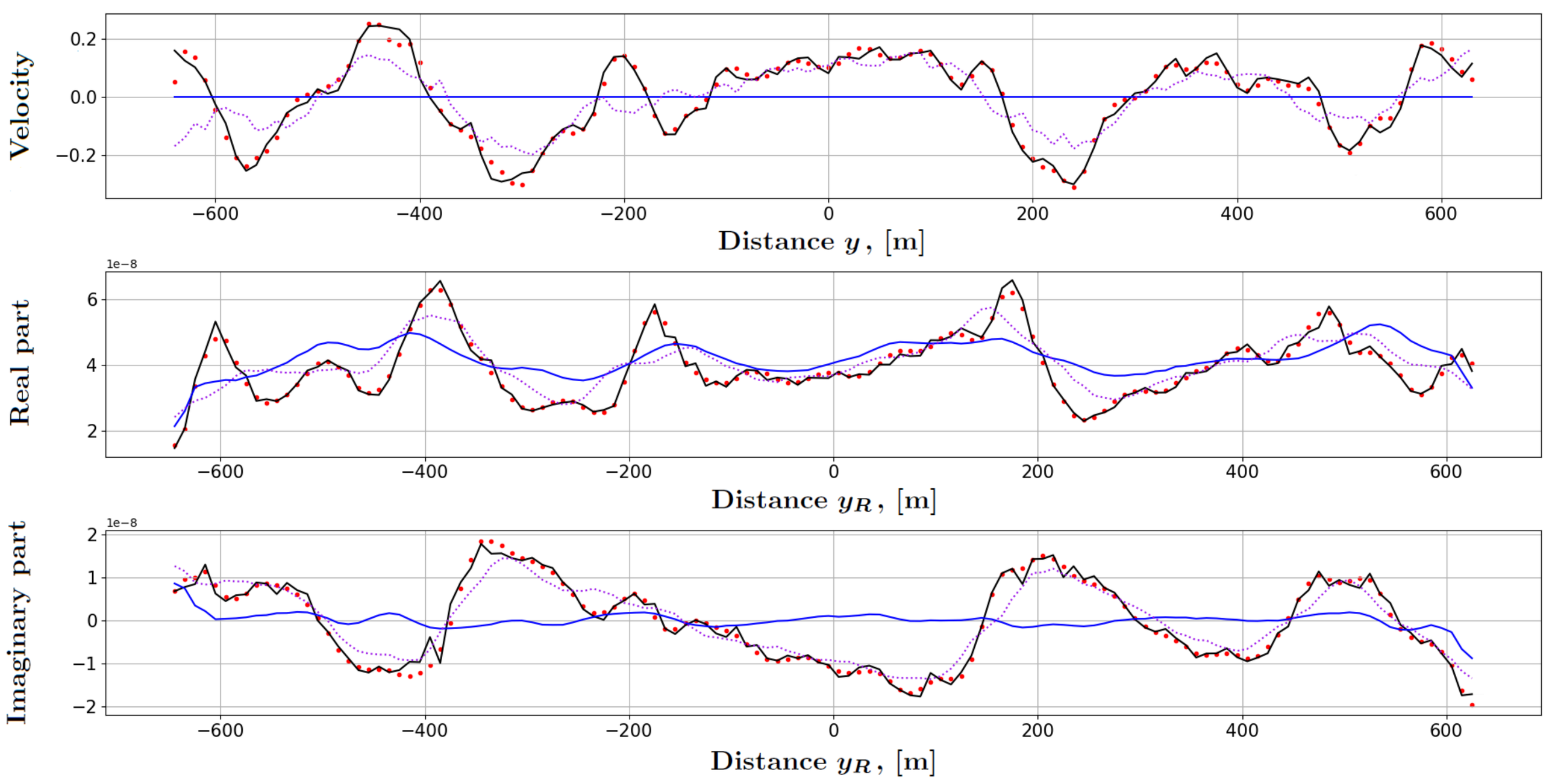
Velocity
0.2
0.0
−0.2
−600
−400
−200
0
200
400
600
Distance y, [m]
Real part
1e−8
6
4
2
−600
−400
−200
0
200
400
600
Distance y_R, [m]
Imaginary part
1e−8
2
1
0
−1
−2
−600
−400
−200
0
200
400
600
Distance y_R, [m]

Figure_16.

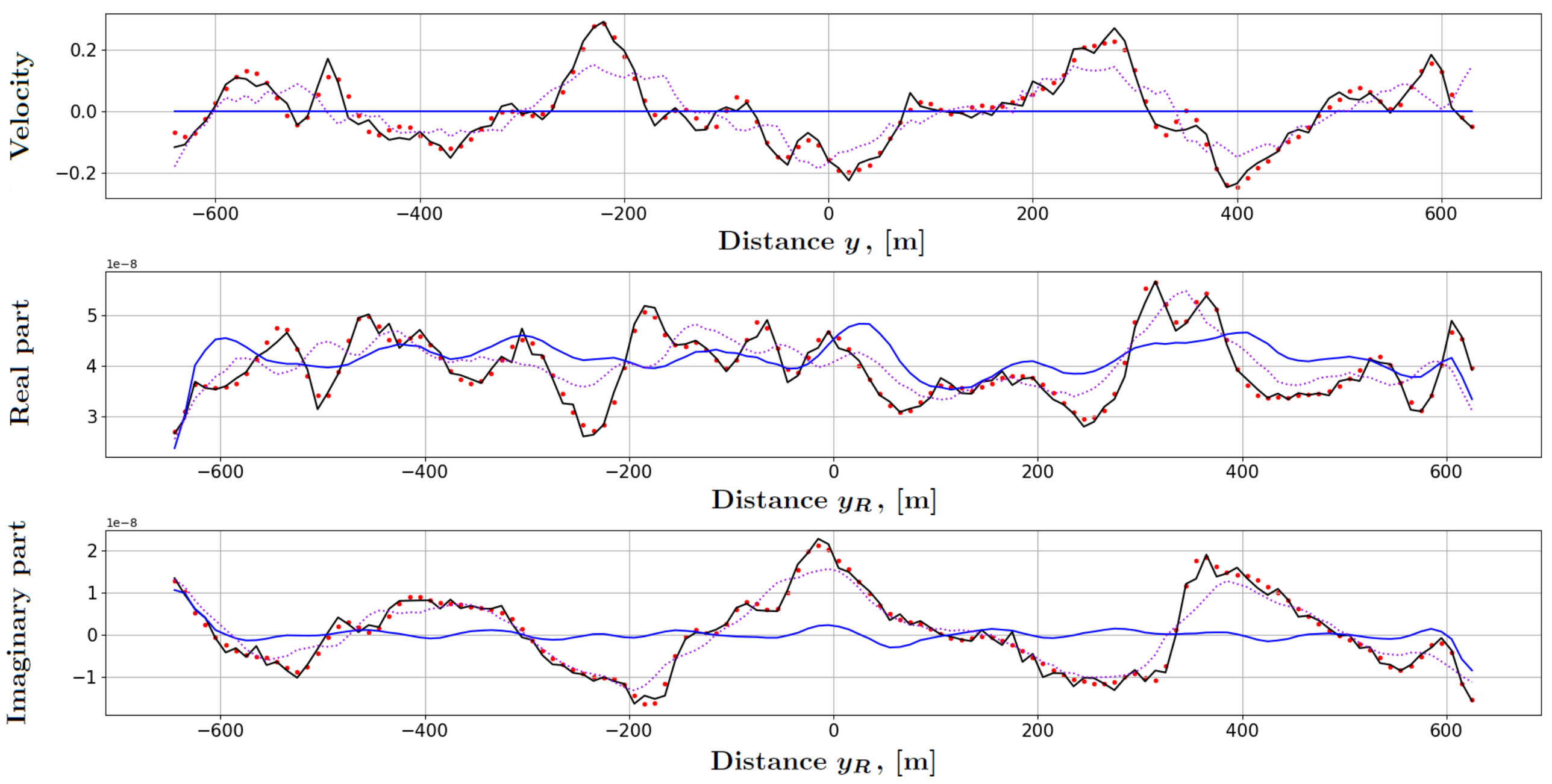
Velocity
0.2
0.0
−0.2
−600
−400
−200
0
200
400
600
Distance y, [m]
Real part
1e−8
5
4
3
−600
−400
−200
0
200
400
600
Distance y_R, [m]
Imaginary part
1e−8
2
1
0
−1
−600
−400
−200
0
200
400
600
Distance y_R, [m]

Figure_17.

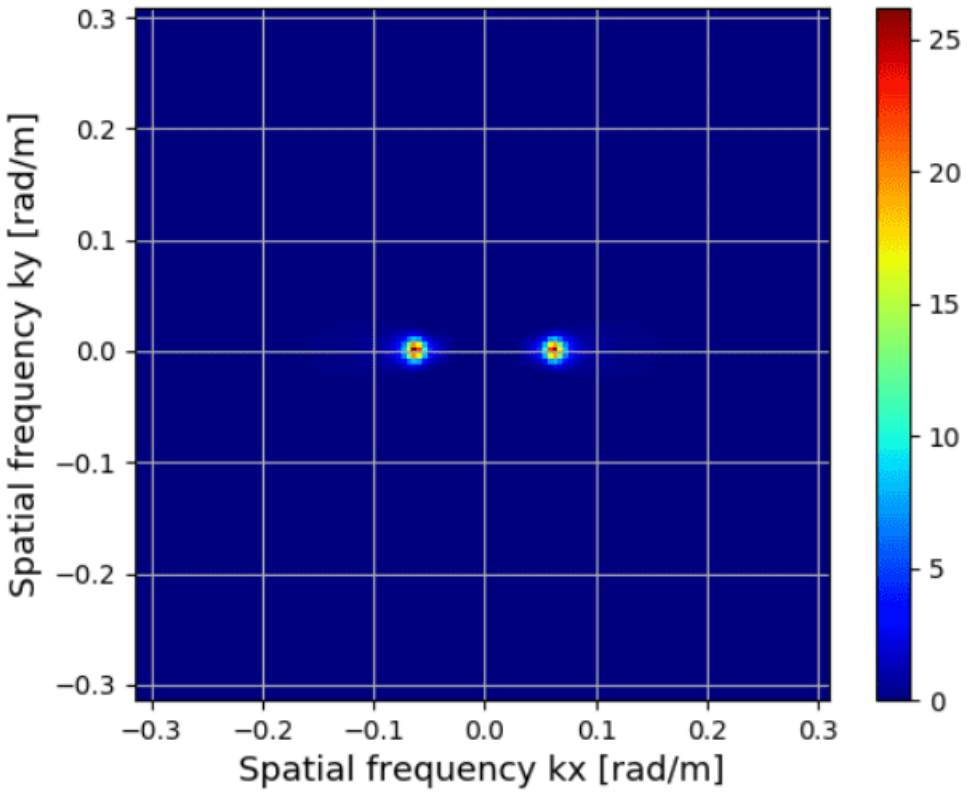

(a) Sampled directional spectrum $\hat{\mathscr{S}}_{2C}$.

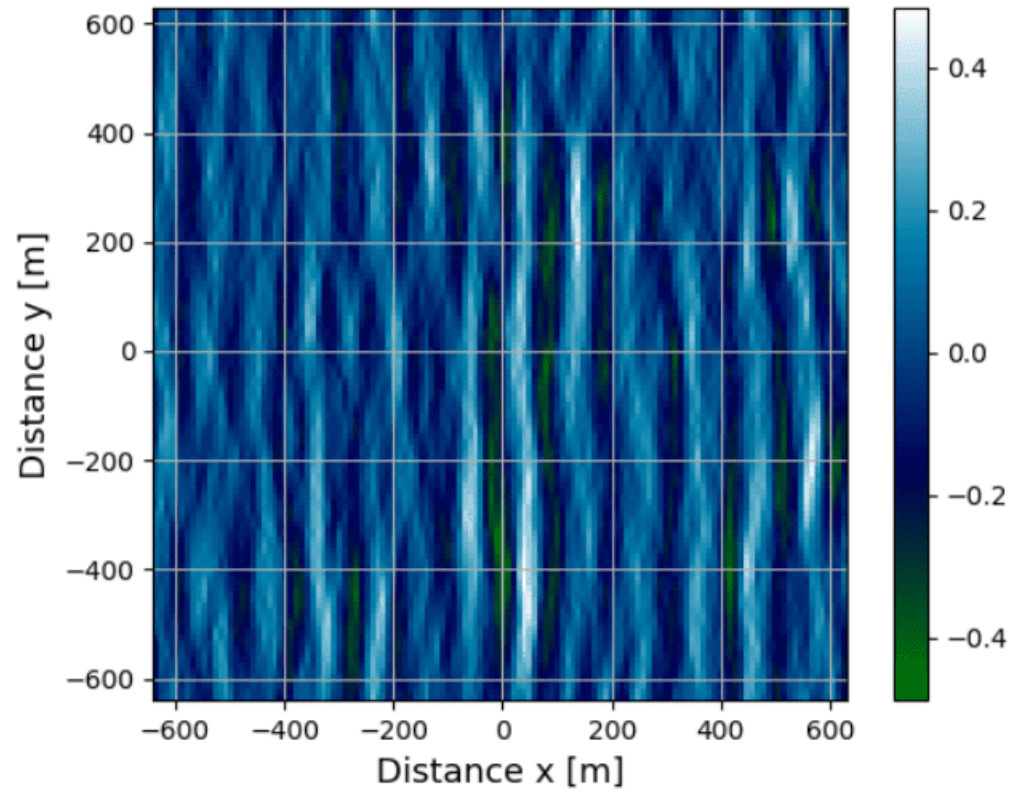

(b) The simulated ocean surface z.

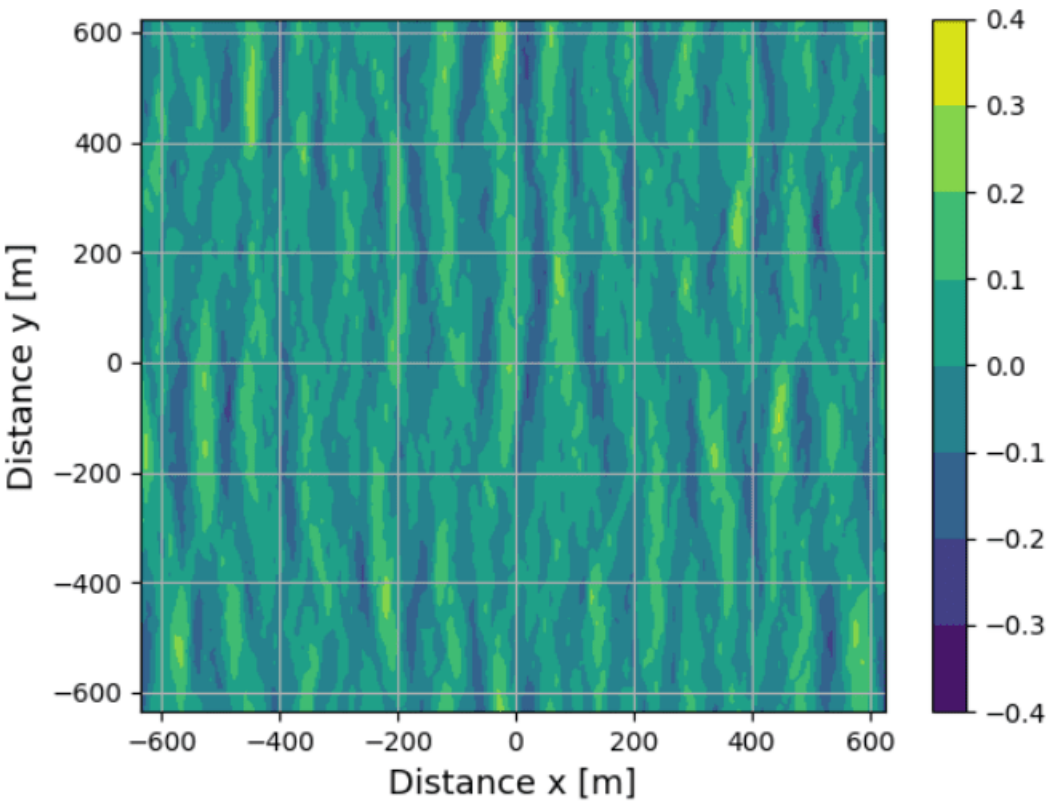

(c) Field of radial velocities u_r.

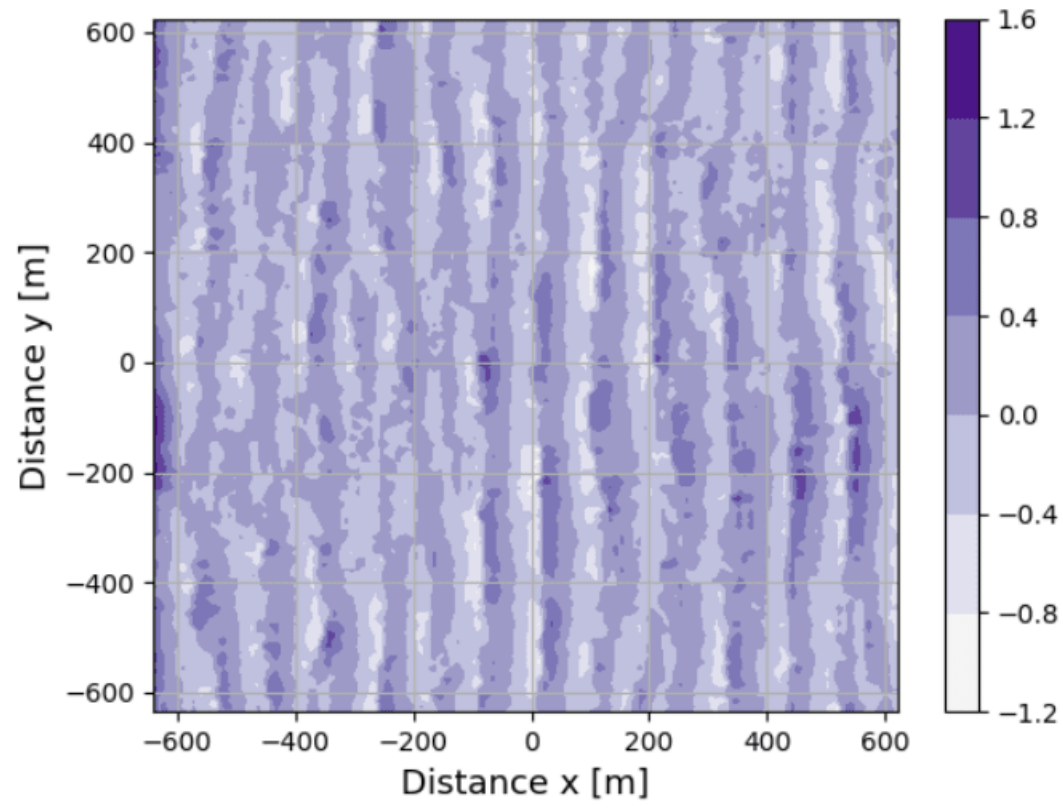

(d) The phase $\Phi_{ATI} = \angle D$.

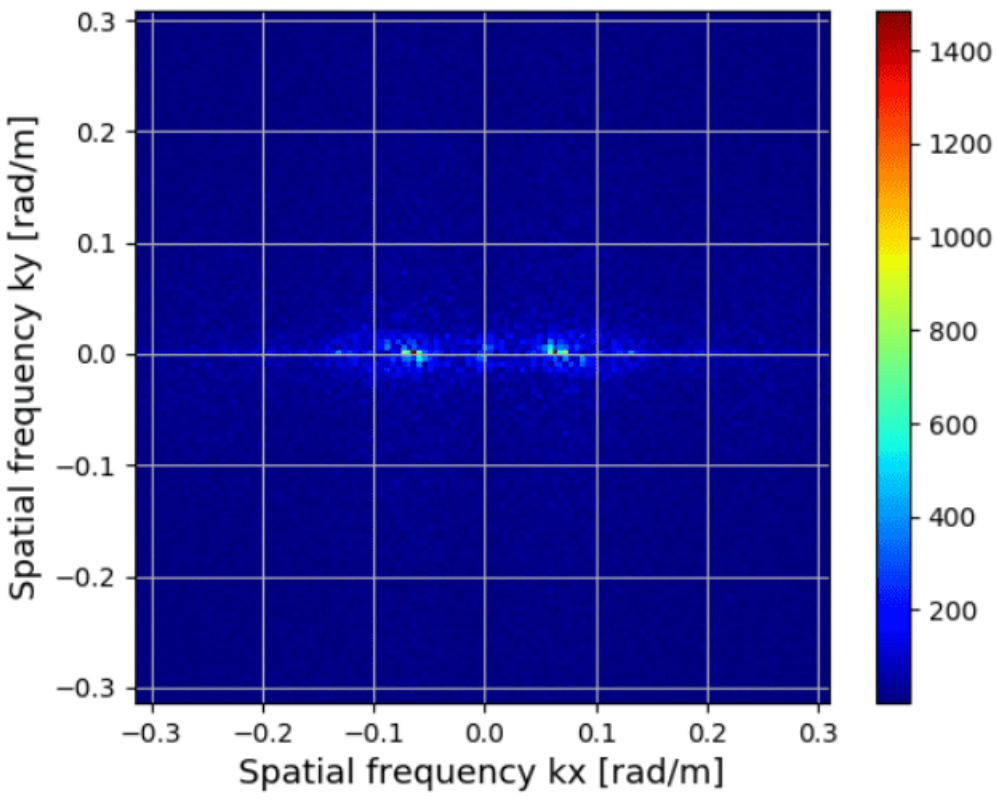

(e) The spectrum $\mathfrak{F}_D\{\Phi_{ATI}\}$.

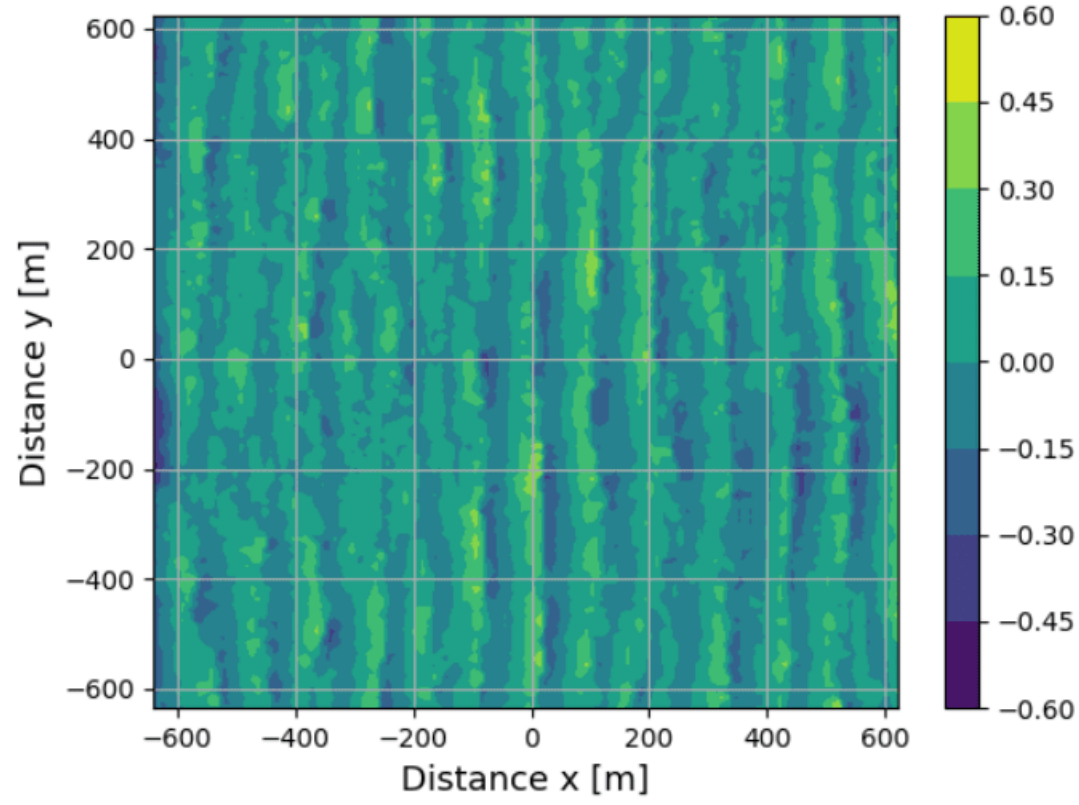

(f) The field u_{ATI}.

Figure_18.

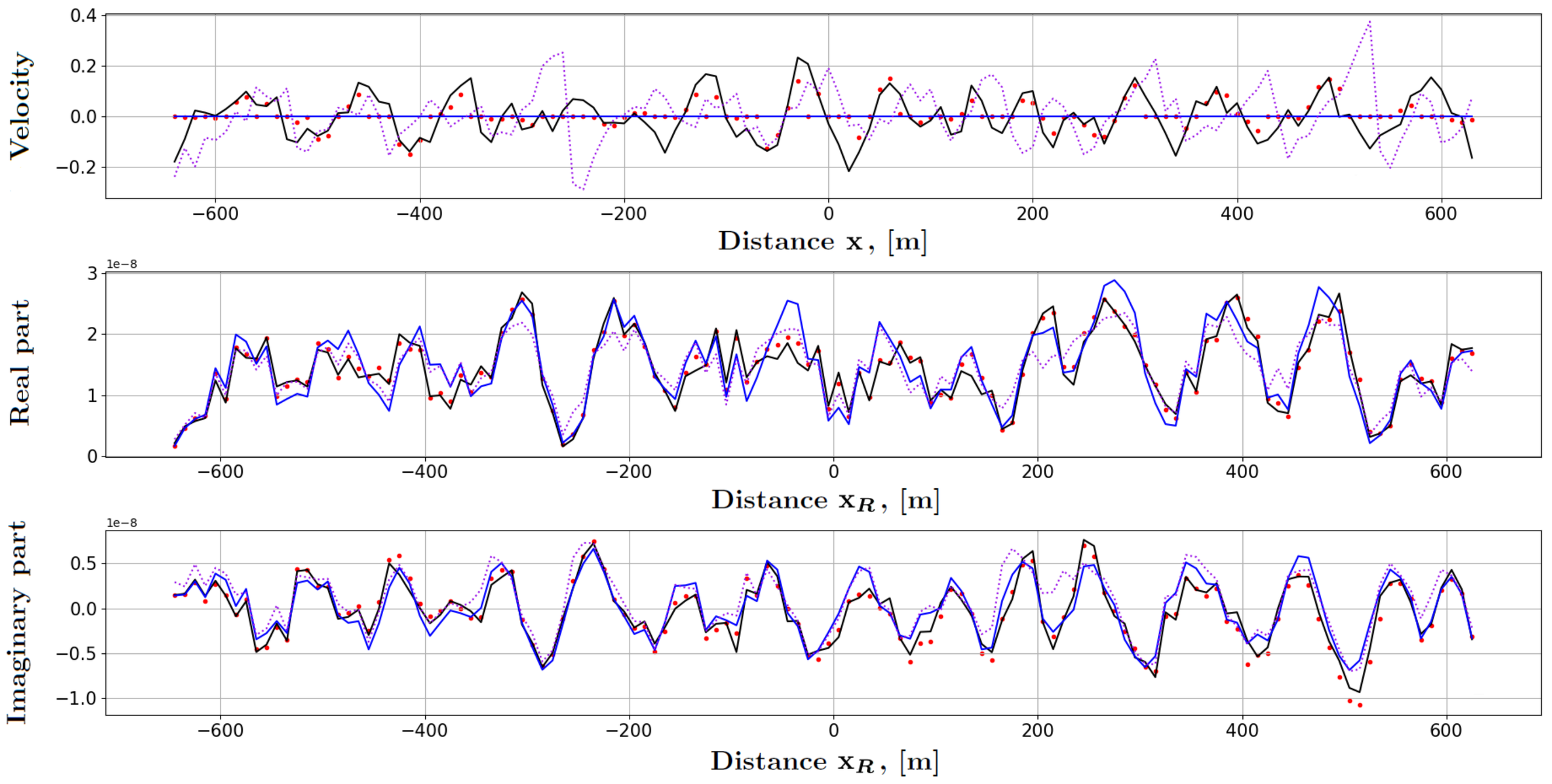
Velocity
0.4
0.2
0.0
−0.2
−600
−400
−200
0
200
400
600
Distance x, [m]
Real part
1e−8
3
2
1
0
−600
−400
−200
0
200
400
600
Distance x_R, [m]
Imaginary part
1e−8
0.5
0.0
−0.5
−1.0
−600
−400
−200
0
200
400
600
Distance x_R, [m]

Figure_19.

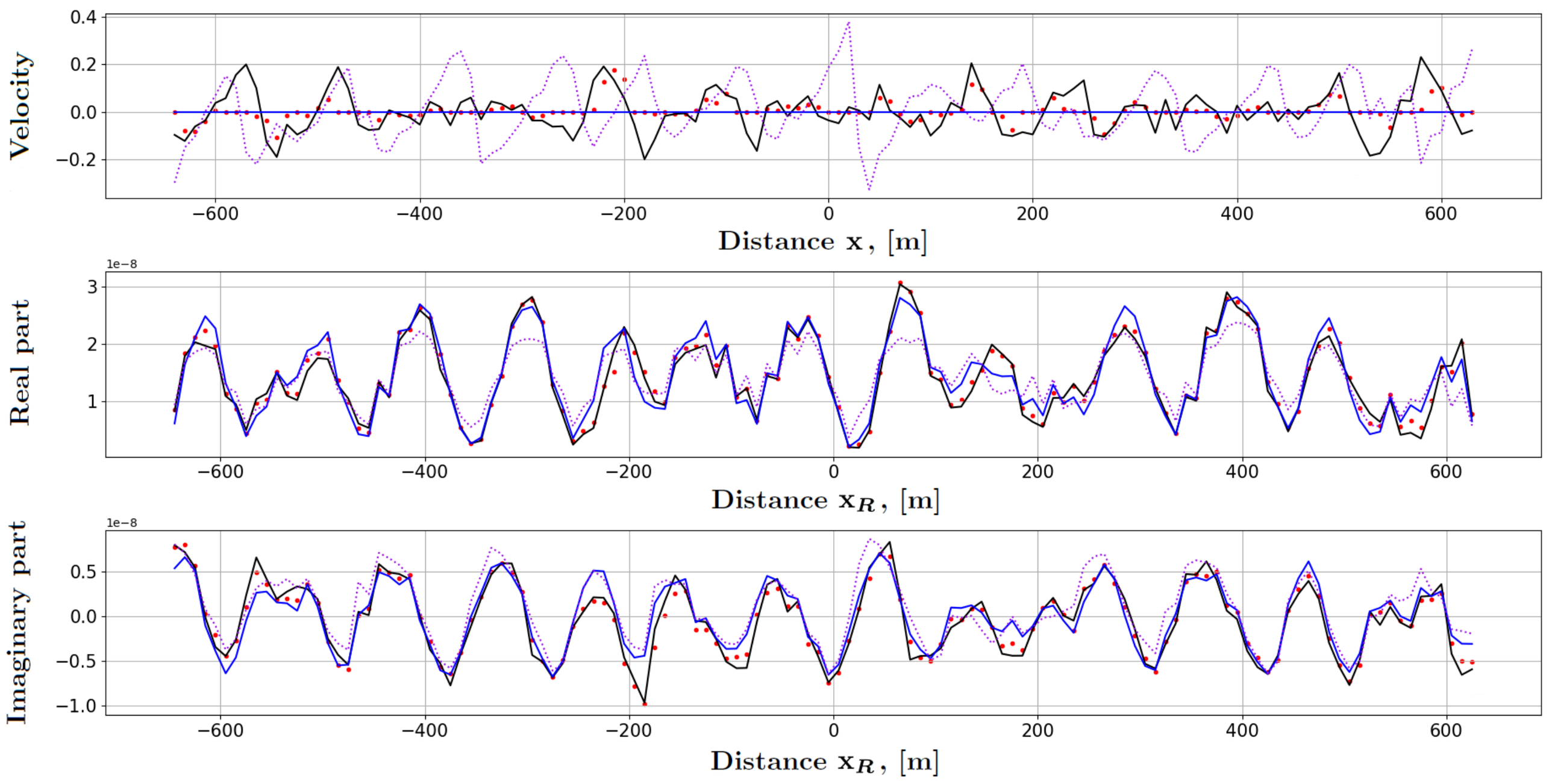
Velocity
0.4
0.2
0.0
−0.2
−600
−400
−200
0
200
400
600
Distance x, [m]
Real part
1e−8
3
2
1
−600
−400
−200
0
200
400
600
Distance x_R, [m]
Imaginary part
1e−8
0.5
0.0
−0.5
−1.0
−600
−400
−200
0
200
400
600
Distance x_R, [m]

Figure_20.

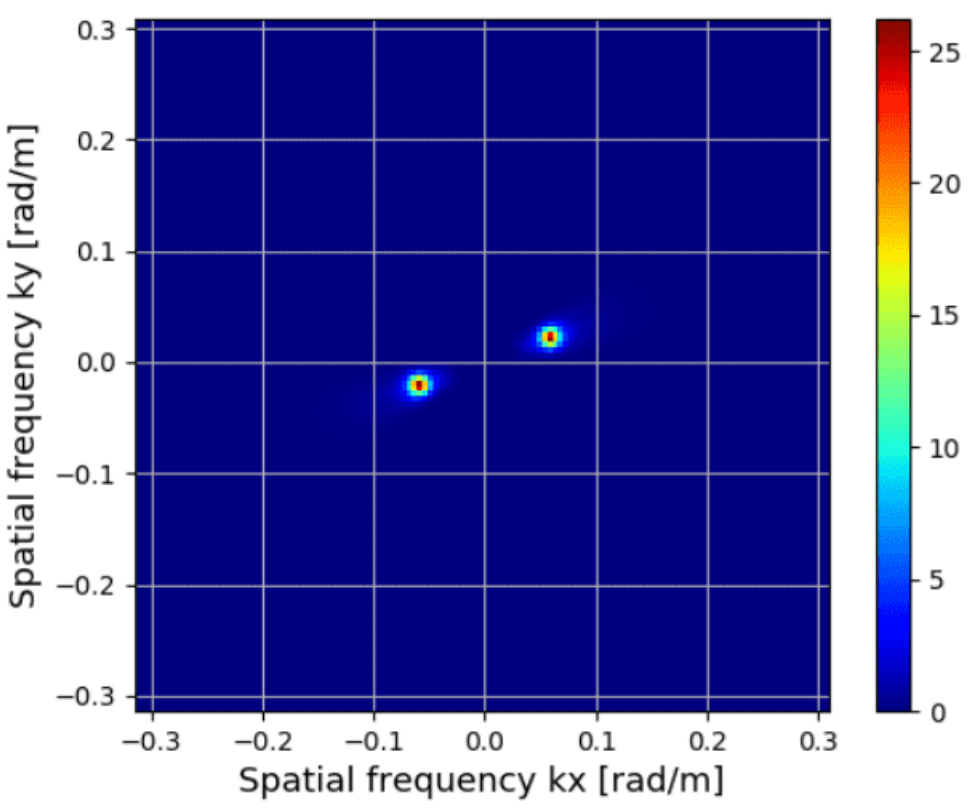

(a) Sampled directional spectrum $\hat{\mathscr{S}}_{2C}$.

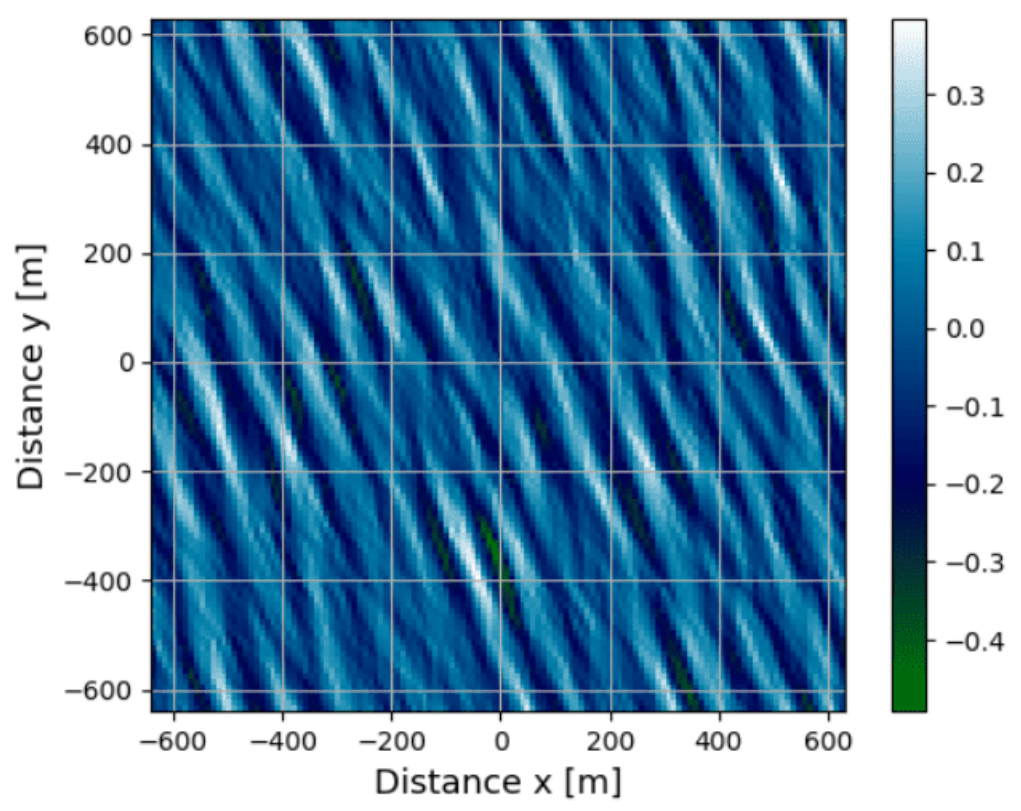

(b) The simulated ocean surface z.

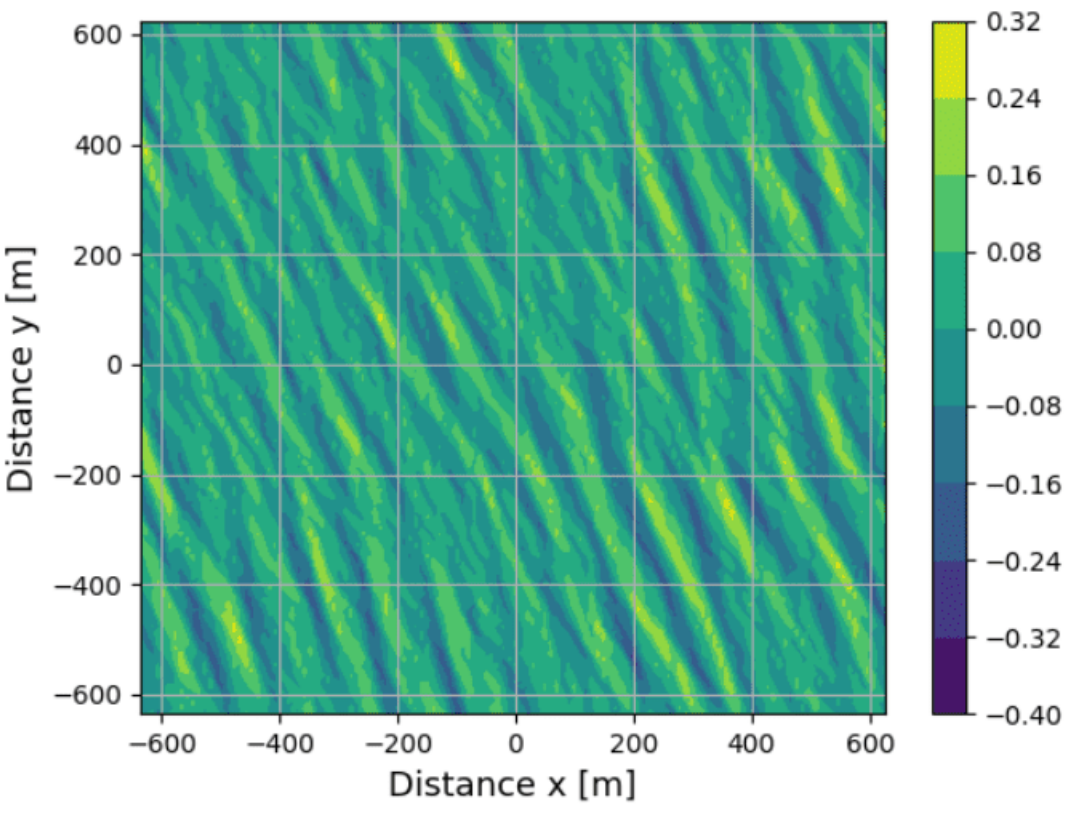

(c) Field of radial velocities u_r.

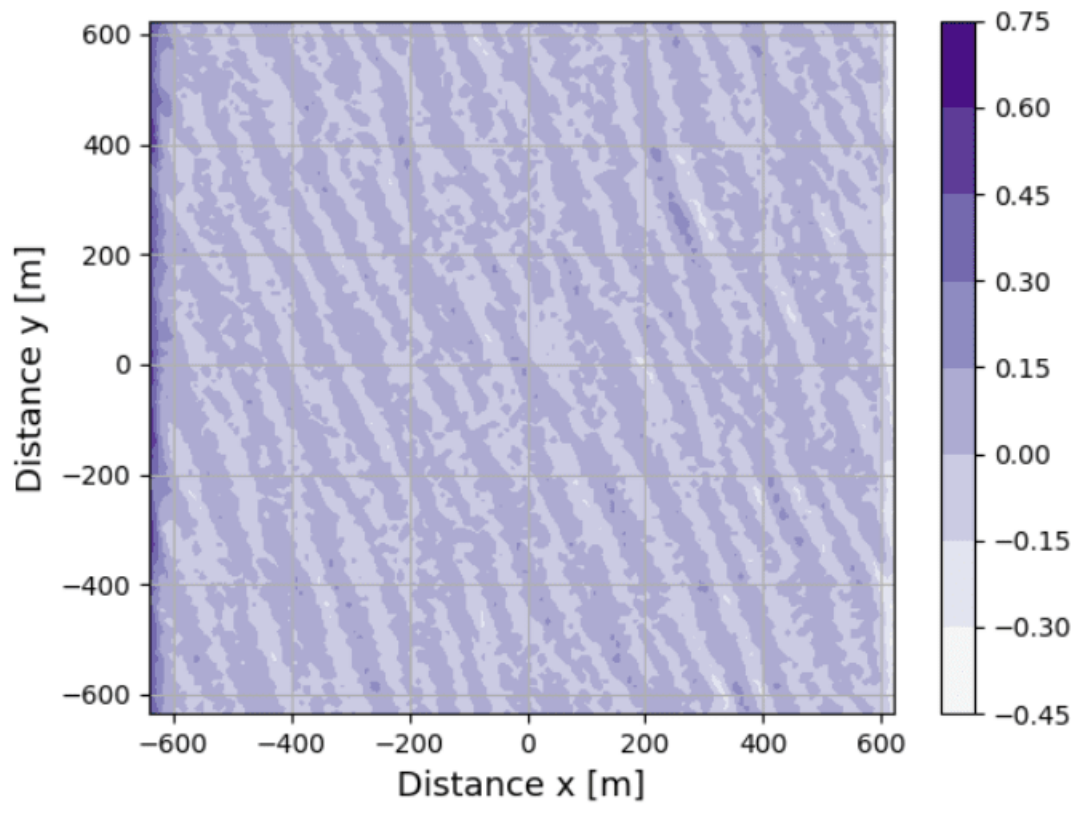

(d) The phase $\Phi_{ATI} = \angle D$.

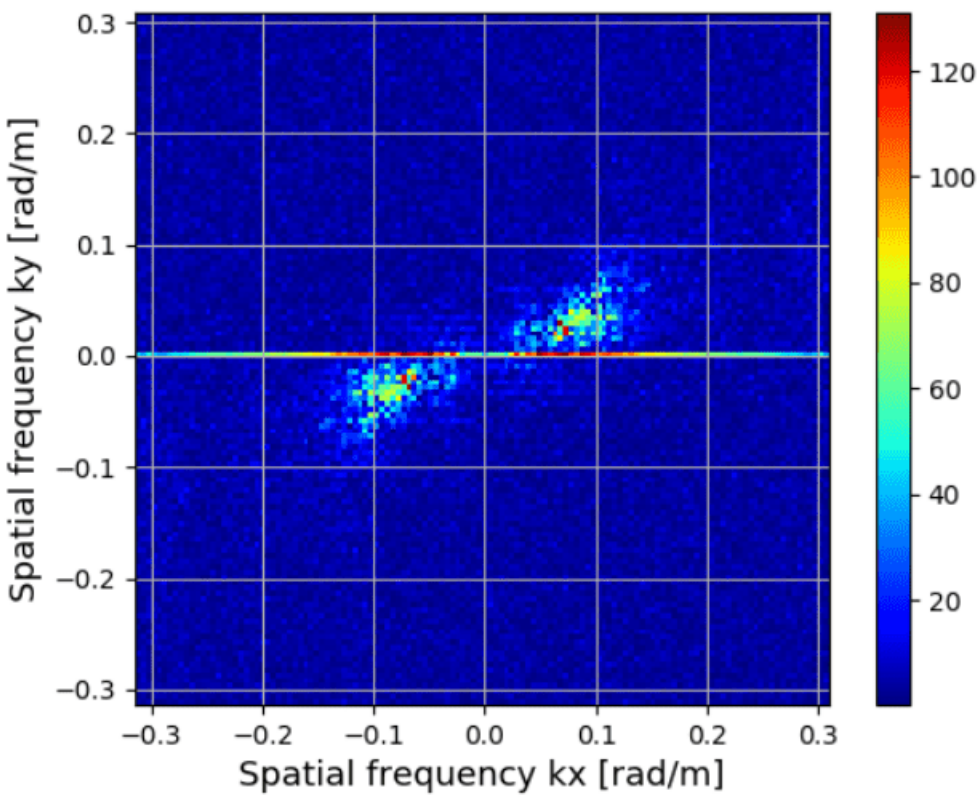

(e) The spectrum $\mathfrak{F}_D\{\Phi_{ATI}\}$.

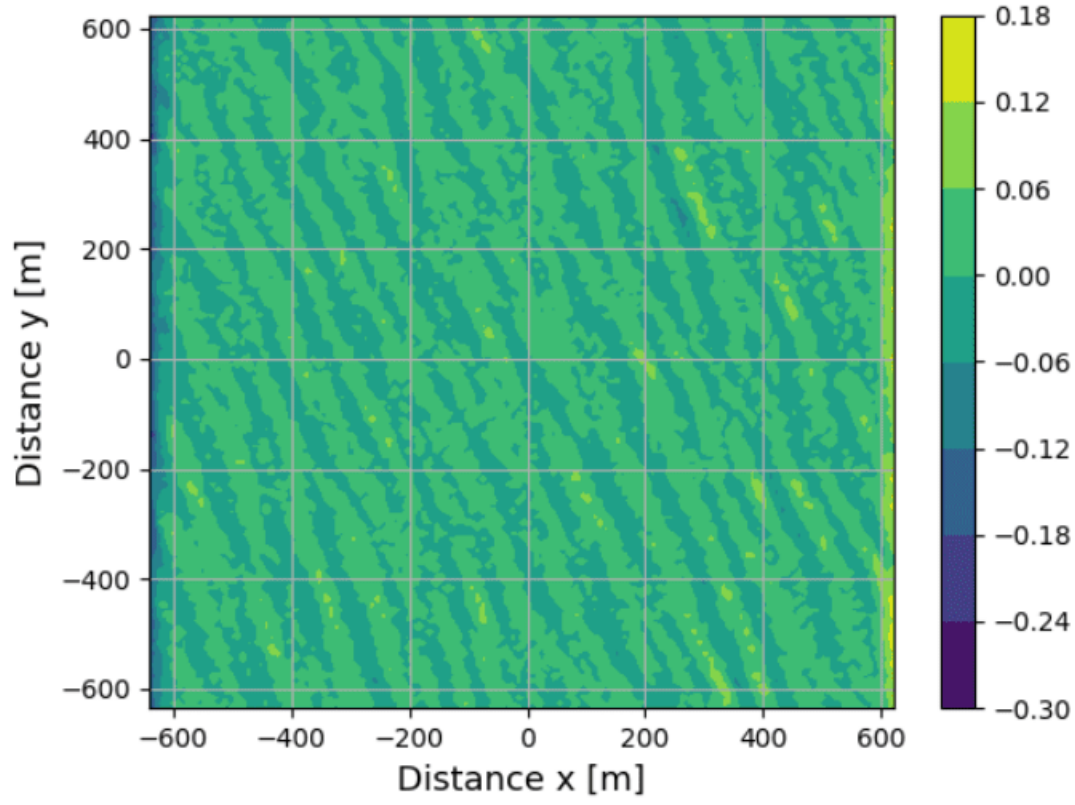

(f) The field u_{ATI}.

Figure_21.

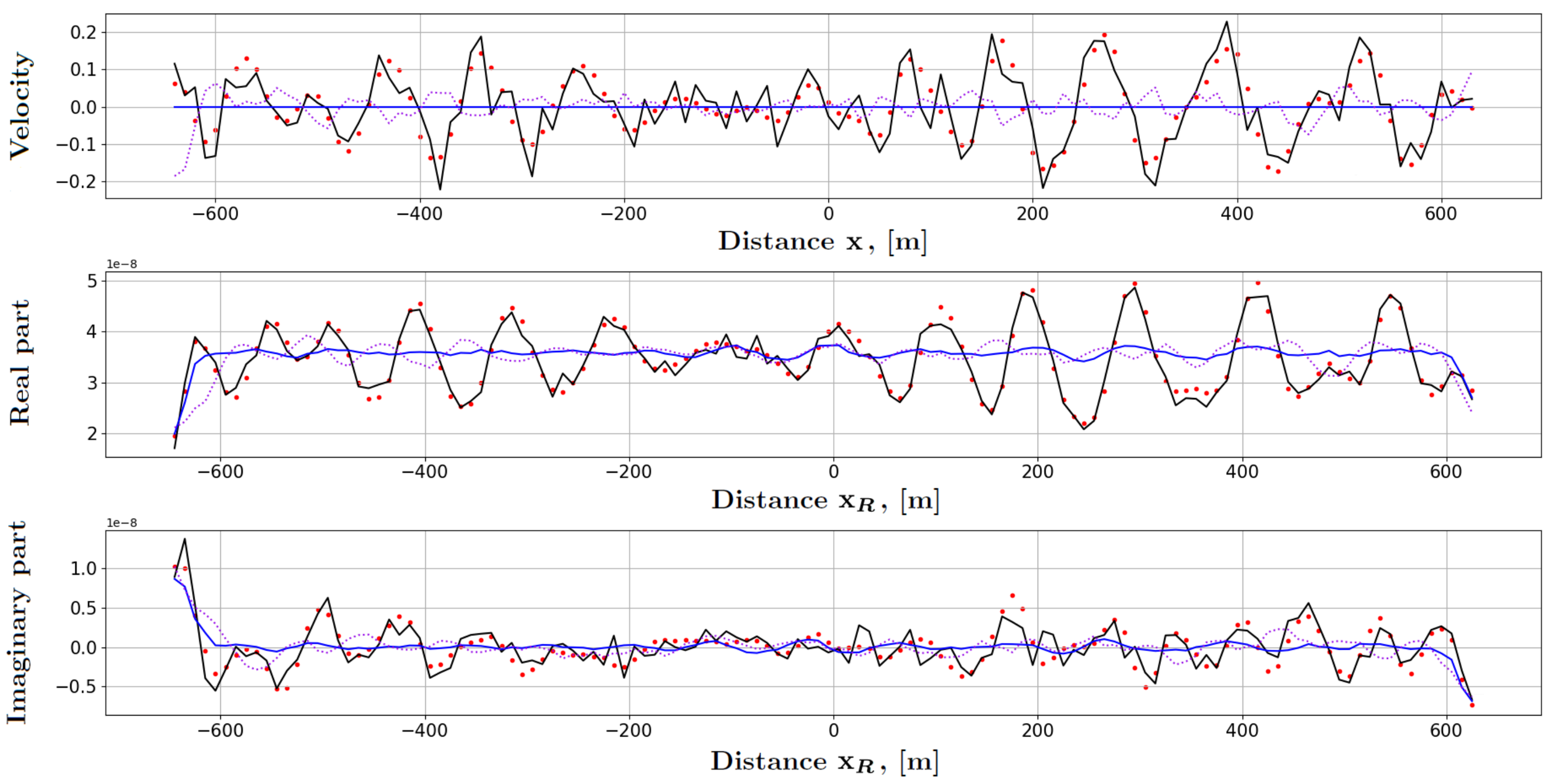
Velocity
0.2
0.1
0.0
−0.1
−0.2
−600
−400
−200
0
200
400
600
Distance x, [m]
Real part
1e−8
5
4
3
2
Distance x_R, [m]
Imaginary part
1e−8
1.0
0.5
0.0
−0.5
Distance x_R, [m]

Figure_22.

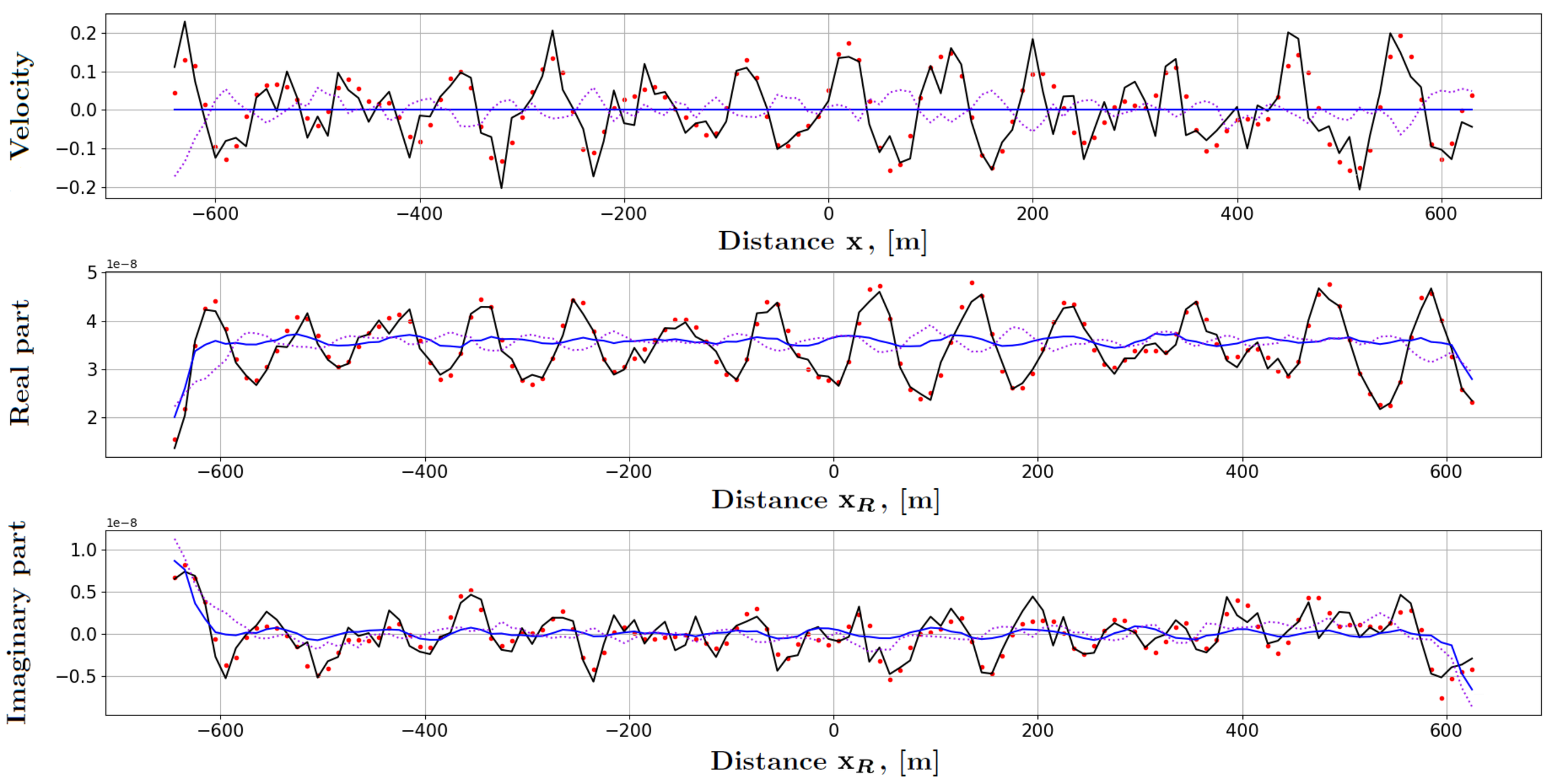
Velocity
0.2
0.1
0.0
−0.1
−0.2
−600
−400
−200
0
200
400
600
Distance x, [m]
Real part
1e−8
5
4
3
2
Distance x_R, [m]
Imaginary part
1e−8
1.0
0.5
0.0
−0.5
Distance x_R, [m]

Figure_23.

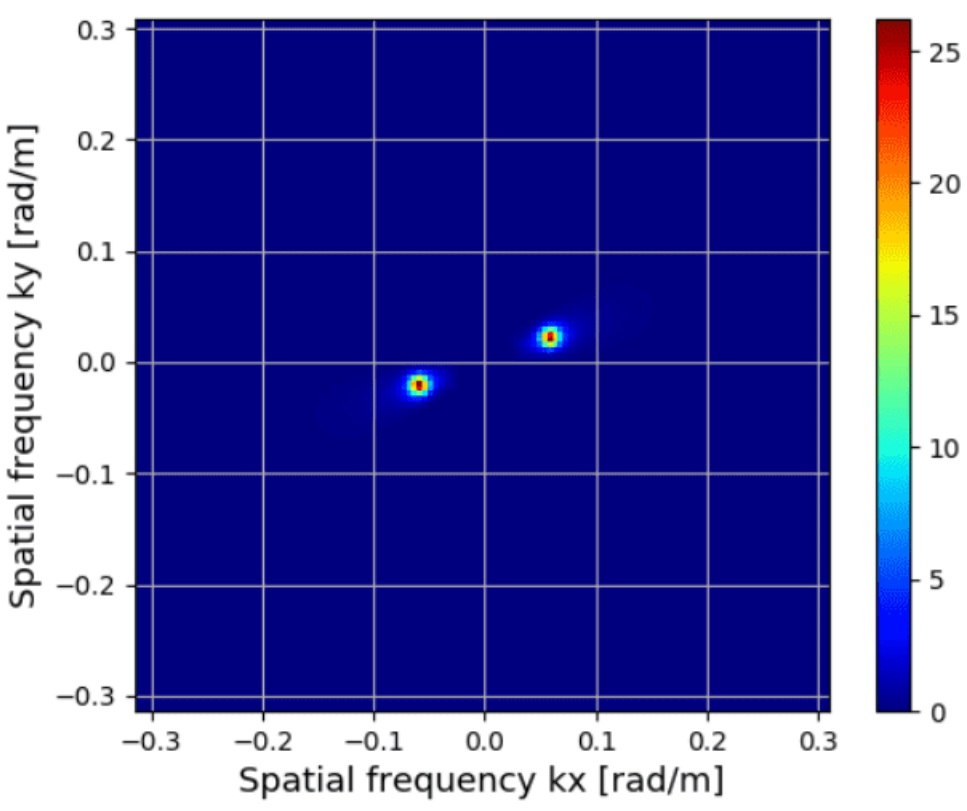

(a) Sampled directional spectrum $\hat{\mathscr{S}}_{2C}$.

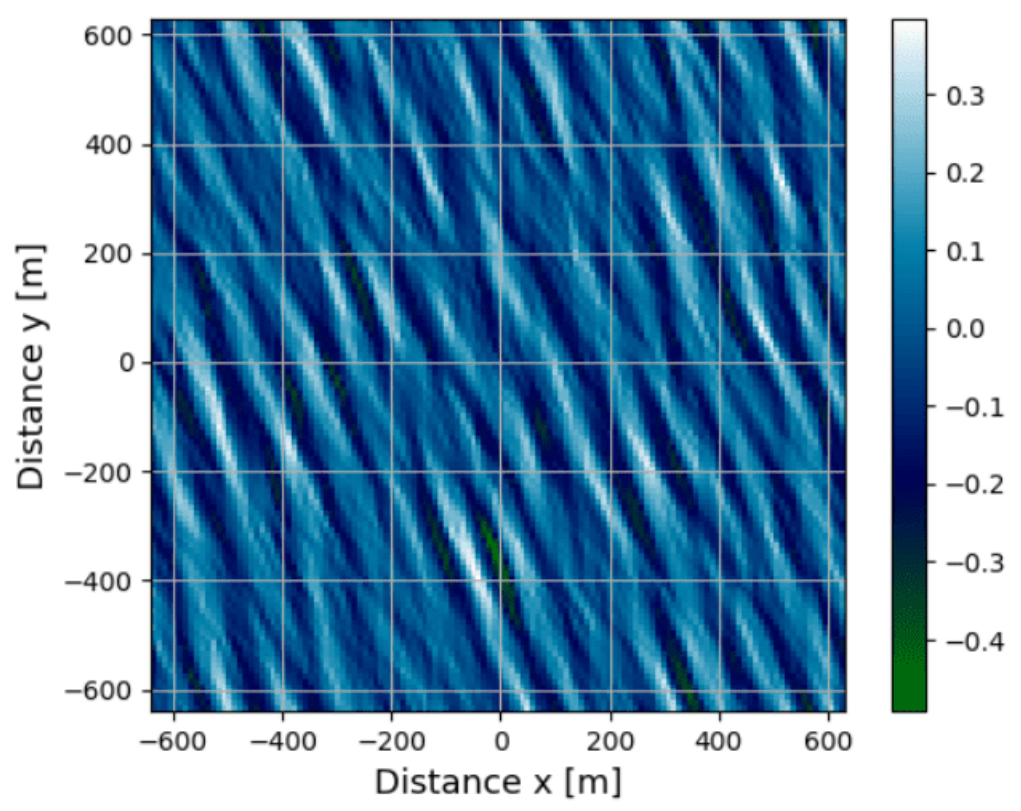

(b) The simulated ocean surface z.

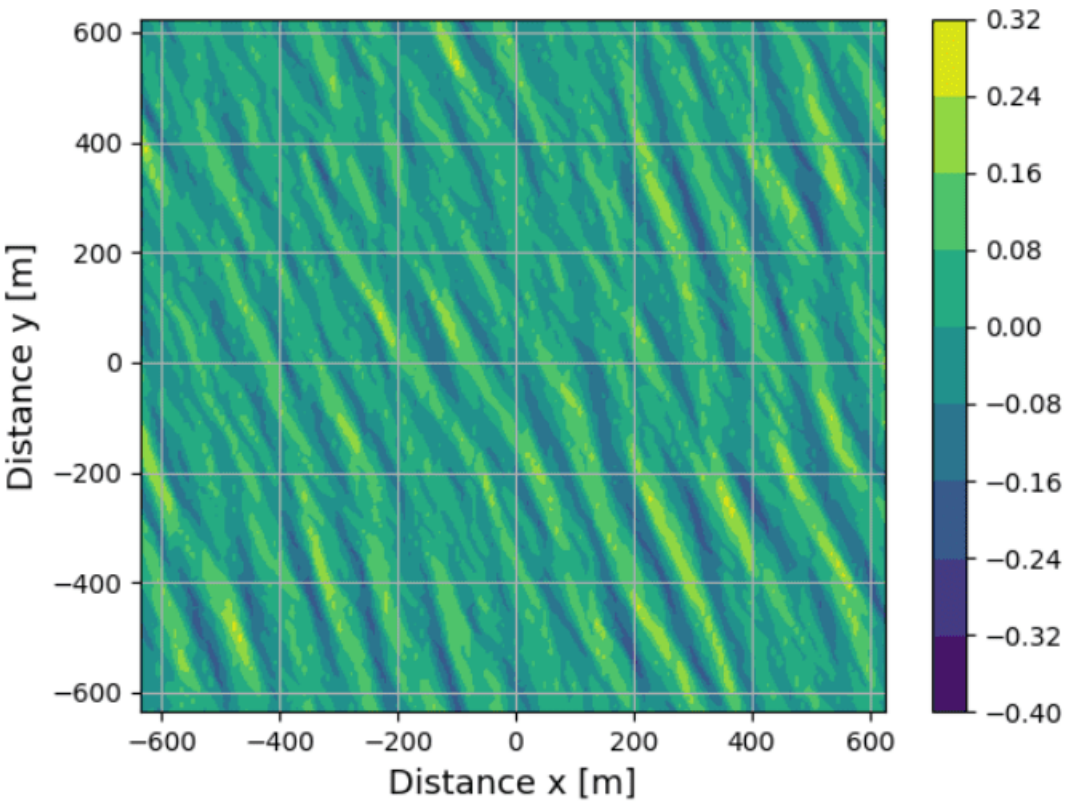

(c) Field of radial velocities u_r.

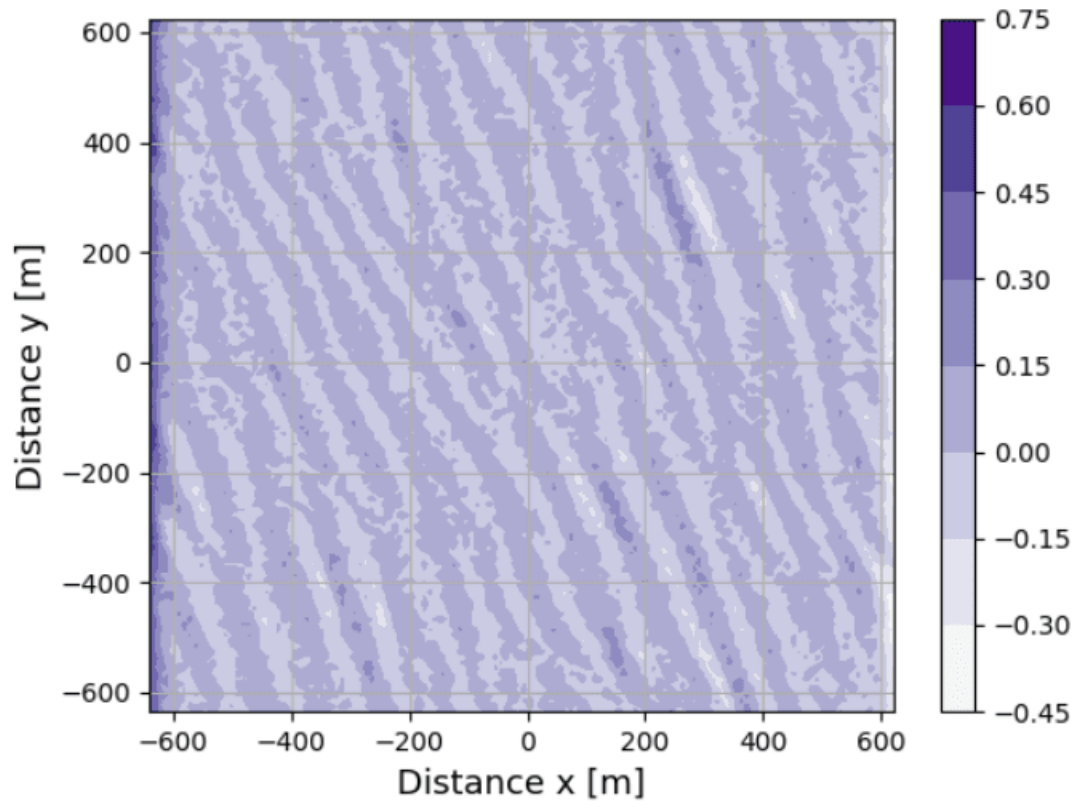

(d) The phase $\Phi_{ATI} = \angle D$.

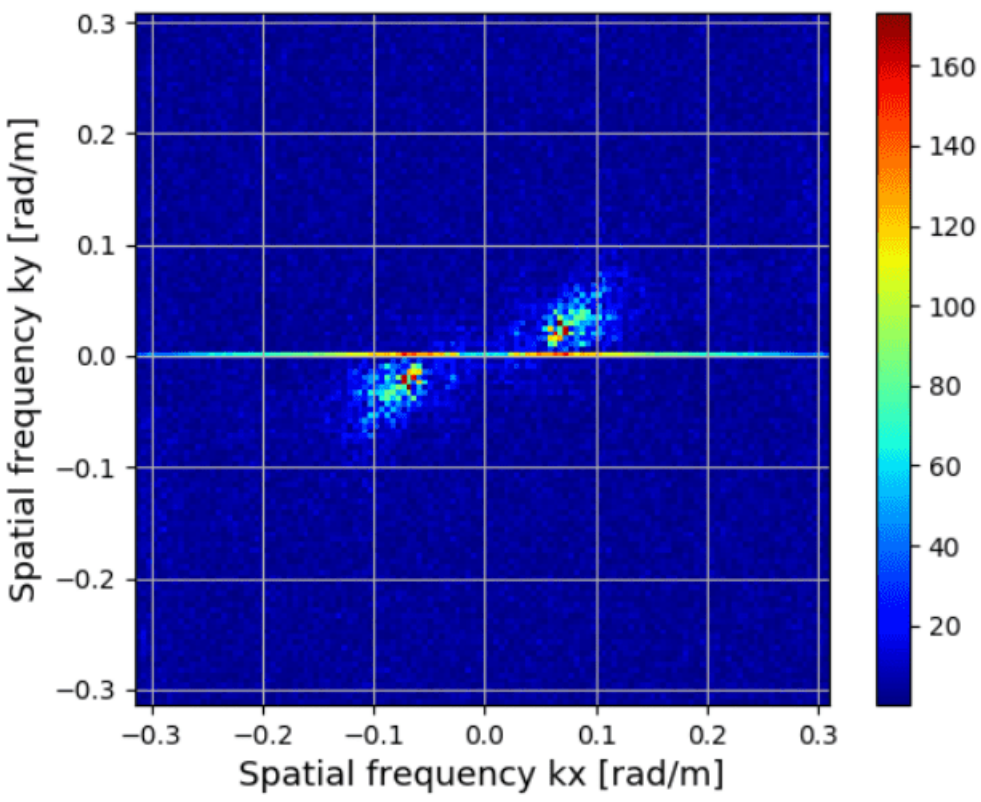

(e) The spectrum $\mathfrak{F}_D\{\Phi_{ATI}\}$.

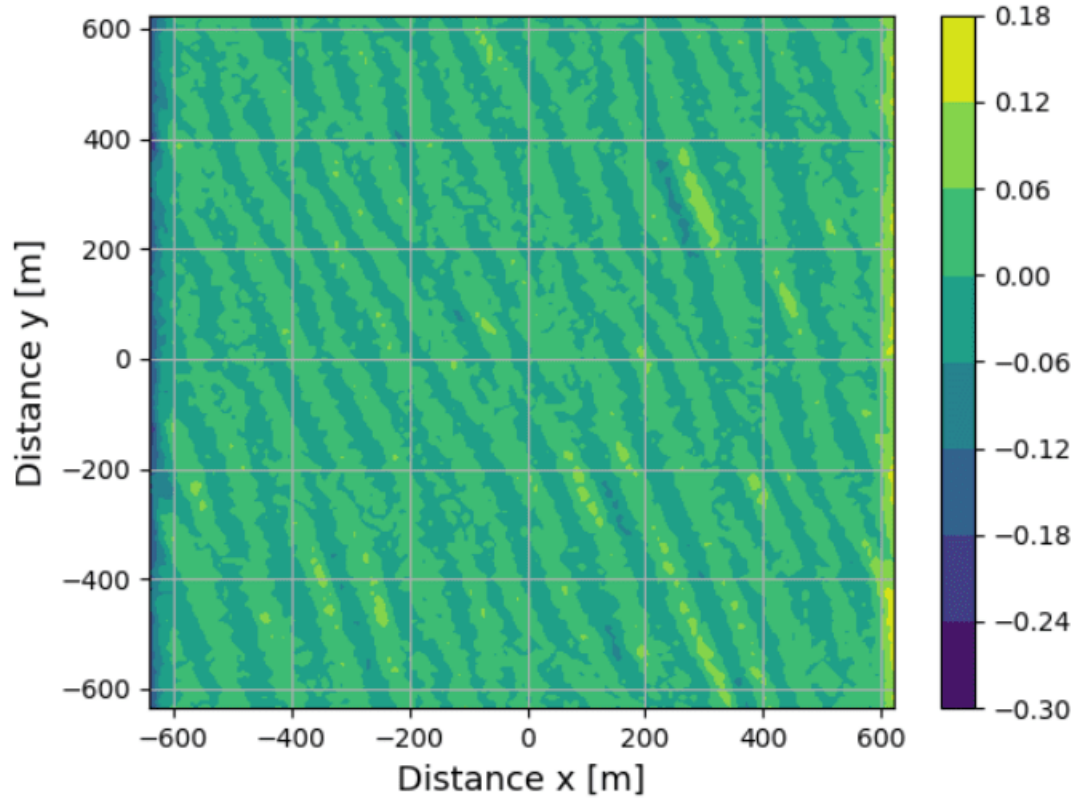

(f) The field u_{ATI}.

Figure_24.

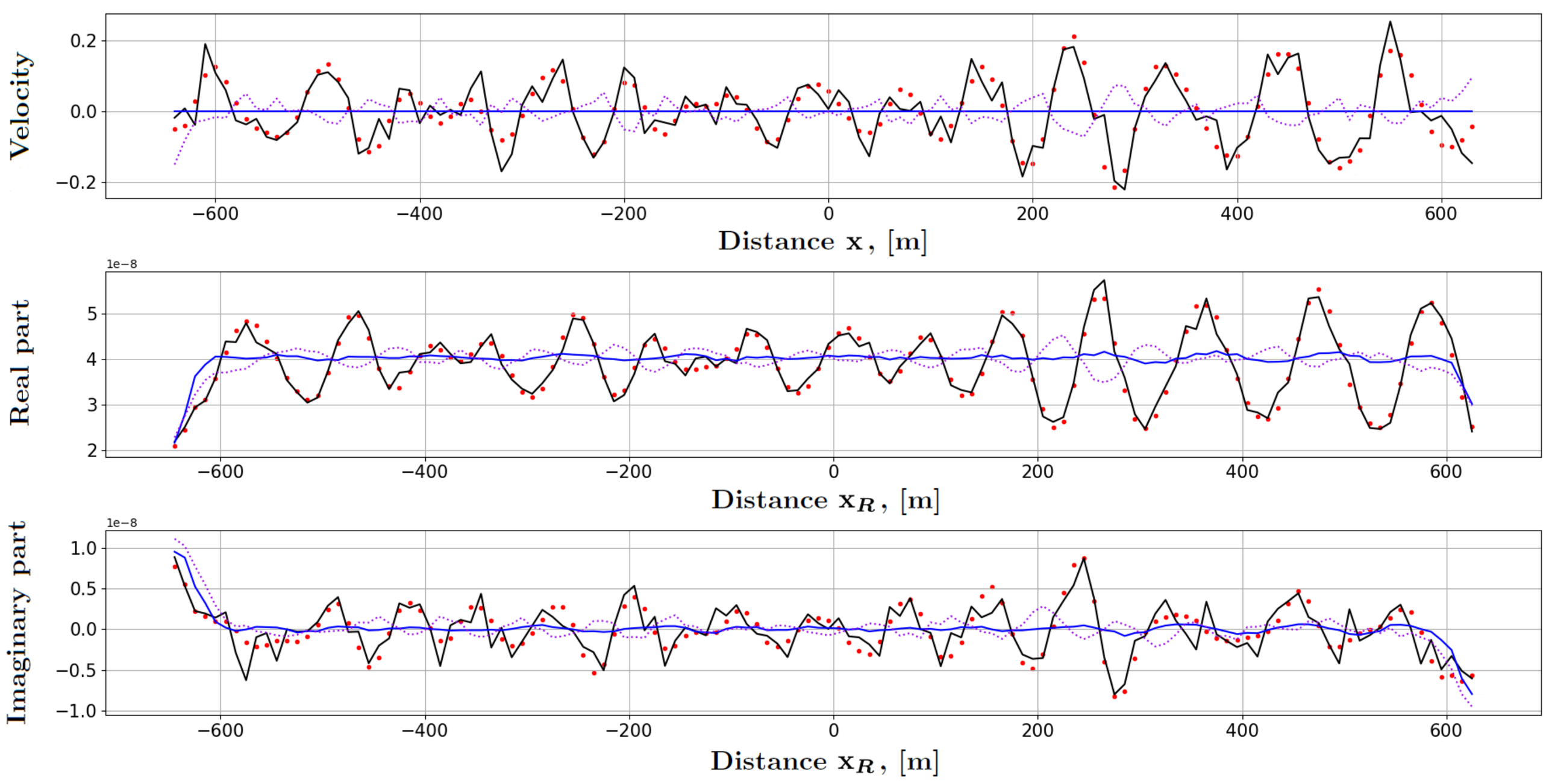
Velocity
0.2
0.0
−0.2
−600
−400
−200
0
200
400
600
Distance x, [m]
Real part
1e−8
5
4
3
2
Distance x_R, [m]
Imaginary part
1e−8
1.0
0.5
0.0
−0.5
−1.0
Distance x_R, [m]

Figure_25.

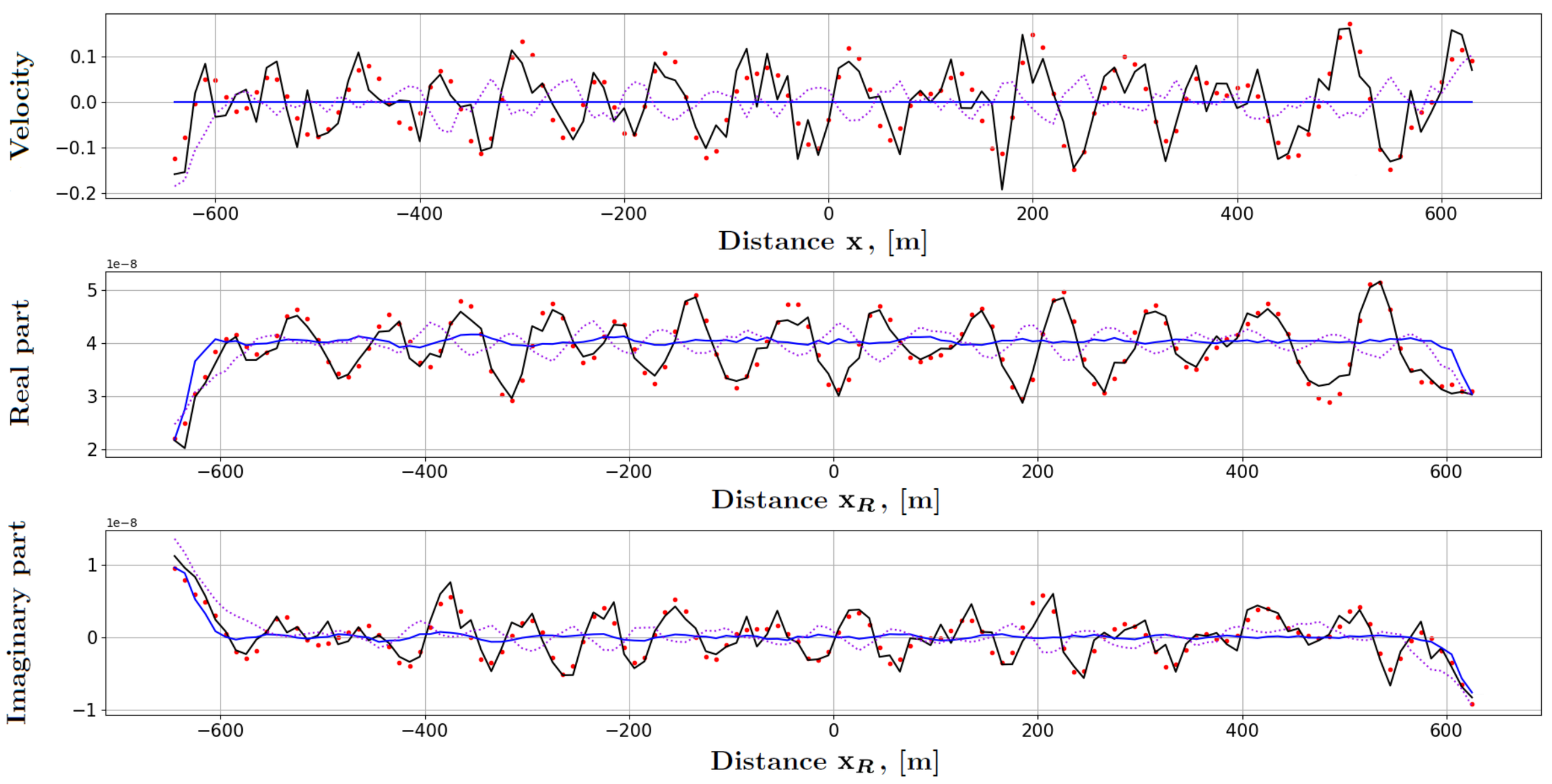
Velocity
0.1
0.0
−0.1
−0.2
−600
−400
−200
0
200
400
600
Distance x, [m]
Real part
1e−8
5
4
3
2
Distance x_R, [m]
Imaginary part
1e−8
1
0
−1
Distance x_R, [m]